ROLE OF INTRINSIC CARBON IN COPPER AND ITS HYDROGEN-ASSISTED DEPLETION DURING GROWTH OF GRAPHENE BY CHEMICAL VAPOR DEPOSITION

by

MOHAMMAD HADI KHAKSARAN

Submitted to the Graduate School of Engineering and Natural Sciences
in partial fulfillment of the requirements for the degree of
Doctor of Philosophy

Sabancı University

January 2019

ROLE OF İNTRİNSİC CARBON İN COPPER AND İTS HYDROGEN-ASSİSTED DEPLETİON DURİNG GROWTH OF GRAPHENE BY CHEMİCAL VAPOR DEPOSİTİON

APPROVED BY:

Assoc. Prof. Dr. İsmet İnönü Kaya (Thesis Supervisor) .....

Assoc. Prof. Dr. Burç Mısırlıoğlu .....

Prof. Dr. Selmiye Alkan Gürsel .....

Assoc. Prof. Dr. Cem Çelebi .....

Assoc. Prof. Dr. H. Özgür Özer .....

DATE OF APPROVAL: 07/01/2019

ABSTRACT

ROLE OF INTRINSIC CARBON IN COPPER AND ITS HYDROGEN-ASSISTED DEPLETION DURING GROWTH OF GRAPHENE BY CHEMICAL VAPOR DEPOSITION

MOHAMMAD HADI KHAKSARAN

Physics, Ph.D. Thesis, January 2019

Thesis Supervisor: Assoc. Prof. Dr. İsmet İnönü Kaya

Keywords: Graphene Nucleation, Graphene Growth, Intrinsic Carbon, Chemical Vapor Deposition (CVD), Copper Annealing

Growth of graphene on Cu by chemical vapor deposition (CVD) method is a multidimensional process. Therefore, a comprehensive understanding of the parameters involved in this process is essential to achieve a reproducible and optimized growth recipe. In this work, the role of intrinsic carbon in the bulk of Cu on nucleation of graphene is revealed and it is disclosed that CVD growth of graphene on Cu foil is not a pure surface process. We uncovered that hydrogen-assisted carbon depletion (HACD) effect causes carbon content within Cu bulk to diffuse out during annealing under hydrogen atmosphere and is a critical mechanism in the nucleation of graphene crystals. Additionally, we investigated the role of hydrogen on the diffusion of carbon toward the Cu surface during annealing. We showed that this interplay is not a linear mechanism, but depending on its concentration hydrogen either can boost or diminish the surface density of segregated carbon atoms from bulk. From that, we managed not only to grow a graphitic film on Cu foil but also and more importantly, illustrate spontaneous nucleation of graphene crystals during hydrogen annealing in the absence of external carbon precursor. To our knowledge, this is the first time such a growth has been realized. This finding can clarify the role of intrinsic carbon on the nucleation mechanism of graphene in the CVD process. We also showed that intrinsic carbon in Cu can effect the formation of ad-layers under as-grown graphene layer.

ÖZET

GRAFEN BÜYÜTMEDE BAKIRDAKİ İÇSEL KARBONUN VE HİDROJEN YARDIMIYLA TÜKETİLMESİNİN ROLÜ

MOHAMMAD HADI KHAKSARAN

Fizik, Doktora Tezi, Ocak 2019

Tez Danışmanı: Doç. Dr. İsmet İnönü Kaya

Anahtar kelimeler: Grafen Çekirdeklenmesi, Grafen Büyütme, İçsel Karbon, Kimyasal Buhar Biriktirme (KBB), Bakır Tavlama

Kimyasal buhar biriktirme (KBB) yöntemi ile grafen büyütülmesi çok boyutlu bir süreçtir. Bu nedenle tekrarlanabilir ve en uygun büyütme reçetesinin elde edilebilmesi için süreçte rol alan parametrelerin kapsamlı olarak anlaşılması önemlidir. Bu çalışmada, bakır bünyesinde bulunan içsel karbonun grafen çekirdeklenmesindeki rolü keşfedilmiş ve KBB ile Cu üzerinde grafen büyütmenin sadece yüzeyde gerçekleşen bir süreç olmadığı açıkça ortaya konulmuştur. Bakırın hidrojen atmosferi altında tavlanmasının, hidrojen destekli karbon tüketimi etkisiyle karbonun Cu içerisinden yüzeye difüzyonuna yol açtığını ve bunun grafen kristallerinin çekirdeklenmesi için kritik bir mekanizma olduğunu ortaya koymuş bulunuyoruz. Buna ek olarak, tavlama sırasında karbonun Cu yüzeyine difüzyonunda hidrojenin rolünü de araştırdık. Bu etkileşimin doğrusal bir bir mekanizma olmadığı, ama yoğunluğuna bağlı olarak hidrojenin, karbon atomlarının içeriden yüzeyde birikmesini arttırdığı ya da baskıladığını gösterdik. Bundan yola çıkarak hidrojen altında tavlama esnasında, karbon kaynağı olmaksızın Cu folyö üzerinde grafitsel film büyütmeyi gerçekleştirdik ve daha önemlisi grafen kristallerinin kendiliğinden çekirdeklenmesini gösterdik. Bilgimiz dahilinde, bu tür bir büyütme ilk kez bu çalışmada gösterilmiştir. Bu bulgu, içsel karbonun KBB süreci sırasında grafen çekirdeklenme mekanizmasındaki rolünün aydınlatılmasını sağlayabilir. Ayrıca, bakırdaki içsel karbonun, büyütülmüş grafen katmanlarının altındaki ek katmanların oluşumunu etkileyebileceğini de gösterdik.

to my family

ACKNOWLEDGEMENTS

First and foremost, I would like to express my sincere gratitude to my advisor, Assoc. Prof. Dr. İsmet İnönü Kaya for his continuous support and encouragement throughout my Ph.D. study. I would like to thank him for all of the opportunities that he has provided me for my research works.

I would like to thank Assoc. Prof. Dr. Burç Mısırlıoğlu, Assoc. Prof. Dr. Cem Çelebi, Prof. Dr. Selmiye Alkan Gürsel, and Assoc. Prof. Dr. H. Özgür Özer for devoting their valuable time and being on my thesis committee.

I would also like to thank the staff of SUNUM Nanotechnology Research Center, and the members of the Faculty of Engineering and Natural Sciences of Sabanci University who have kindly helped me with my research works.

I am deeply grateful to all of our laboratory members for their friendship and sharing their experience with me. Dr. Cenk Yanik, Dr. Sibel Kasap, Suleyman Çelik, Hasan Ozkaya, Abdulkadir Canatar, and Vahid Sazgari have supported me as true friends in my difficult times. I would like to thank them all for their constant support.

Finally and most importantly, I would like to express my deepest gratitude to my family for their endless loves and persistent supports over the years. Without their self-devotion, I would not be able to fulfill my academic goals.

Table of content

List of Figures

List of Tables

List of Abbreviations

GFs	: Graphene Flakes
CVD	: Chemical Vapor Deposition
ToF-SIMS	: Time of Flight Secondary Ion Mass Spectrometry
DGF	: Disordered Graphitic Film
SNGFs	: Spontaneous Nucleation of Graphene Flakes
Cu	: Copper
H	: Hydrogen
O	: Oxygen
SEM	: Scanning Electron Microscopy
PMMA	: Polymethyl Methacrylate
ACE	: Acetone
IPA	: Isopropyl Alcohol
DI	: Deionized
SiO_2	: Silicon Dioxide
EDS	: Energy Dispersive X-ray Spectroscopy
µm	: Micrometer
HOPG	: Highly Oriented Pyrolytic Graphite

1 Introduction

1.1 Context and Motivation

Since the first demonstration of the growth of graphene by chemical vapor deposition (CVD) on copper[1], a variety of improvements such as achieving centimeter size single crystals[2-5] and high carrier mobility comparable to mechanically exfoliated graphene have been realized.[6] These developments have made CVD growth on copper the most prominent method for graphene production for various suggested applications.[7-9] Therefore, the high demand for an economical and reproducible technique for the mass scale production of high quality graphene has led to many studies on CVD growth mechanisms [2, 10-23]. This elevated the motivation for research on growth mechanisms of graphene in CVD process.[2, 10-23] It has been discussed that the very low solubility of carbon in copper makes the graphene growth process to be governed by surface-adsorption and therefore leading to a self-limited course.[10] Weak surface diffusion barrier for carbon ad-atoms leading to the high mobility of carbon on copper at high temperatures is another reason for the growth of graphene to be considered as a pure surface-based process.[14, 24, 25] Overall, the CVD growth of graphene is described to be initiated with the adsorption of carbon precursor molecules on the copper surface, followed by their dissociation to form active carbon species which diffuse on the surface until trapped and accumulated at defect sites. Increase in the carbon concentration at defect sites leads to supersaturation of carbon and finally the nucleation of graphene flakes.[23, 26]

In the process where just a few atoms can have a substantial effect on the growth of one-atom-thick carbon crystal, delicate surface processes at high temperatures can easily lead to irreproducibility. This caused significant difficulties in uncovering the underlying

mechanisms behind the growth of graphene on copper. For example, initially, the passivation of nucleation sites due to reaction with oxygen had been suggested as the reason for the suppression of graphene nucleation in the presence of diluted oxygen. But later it has been agreed that the reduction in the nucleation is mainly due to the etching of carbon from the surface of Cu foil by oxygen. [2, 4, 19, 27-29] Likewise, while etching effect of hydrogen has initially been reported [30-34], later it has been argued that oxygen/water from hydrolyzers was the cause of etching of carbon on Cu ***surface*** and the inconsistency of nucleation process.[4, 35, 36] However, the effect of hydrogen on the carbon ***inside*** the bulk of Cu foil has not been fully described for the CVD process yet.

Moreover, because Cu foil had been widely considered to behave as pure copper with very low solubility for carbon, the intrinsic carbon incorporated in Cu foil during its production has been overlooked for many years. However, few recent reports imply that presence, dissolution, and diffusion of carbon inside copper foil makes the nucleation and growth of graphene to be more complex and multifunctional process than what was proposed earlier.[19, 21, 37, 38]

The underlying motivation of this thesis is to disclose the causes of inconsistency in the outcome of graphene growth by the CVD method and step toward final words on all growth-related issues. While almost all of the papers in this field have been focused on the effect of external carbon source on the graphene growth on copper, the first objective of this thesis is to report spontaneous nucleation of graphene on copper due to the presence of intrinsic carbon.

Accordingly, to achieve a comprehensive model for the nucleation of GFs on Cu foil, mapping the interplay between “presence, dissolution, and diffusion of carbon inside copper foil” and other parameters such as oxygen and hydrogen is essential. Therefore, the second intention of this thesis is to study the interplay between the flowing hydrogen in the CVD system and intrinsic carbon inside the copper.

The presented experimental results in this thesis about depletion and/or etching of intrinsic carbon in copper by hydrogen could explain critical open issues on the growth mechanism of graphene on copper foil and help us to draw a brighter picture about initial stage of graphene nucleation on the copper surface in the CVD process.

1.2 Structure of the Thesis

In chapter 2, the main aspects of the graphene growth on copper by chemical vapor deposition (CVD) are briefly reviewed, including the growth mechanism, the experimental setup for the CVD process, graphene transferring to the dielectric substrate. Besides in this chapter, we discuss the main characterization techniques that have been used in our studies on graphene nucleation and growth on copper.

In chapter 3, our experimental approach and our original results for *"Spontaneous nucleation of graphene flakes (SNGFs) on a copper foil in the absence of external carbon"* are presented. In this chapter, we demonstrate how the presence of intrinsic carbon copper foil results either in the growth of a graphitic film or nucleation of graphene on the surface of copper. Accordingly, we proposed a microscopic mechanism for hydrogen-assisted carbon depletion (HACD), that supplies nucleation and growth of graphene or graphitic film during the annealing process.

In chapter 4, the pressure dependence of hydrogen-assisted carbon depletion has been studied. This study reveals the opposite aspect of HACD which is etching of carbon from copper under high concentration of hydrogen. Therefore we successfully demonstrate this effect as an approach for suppression of graphene nucleation after an effective HACD.

In chapter 5, further technical details and experimental results are presented and discussed. We confirmed the white nano-particles which is very commonly observed in the SEM image of CVD graphene are SiO_2/SiO_x particles. Additionally, we present our experimental result for the effect of HACD on the nucleation of graphene ad-layers. Finally, we discussed the technical challenges toward a quantitative evaluation of HACD in copper.

In chapter 6, the primary outcomes of this thesis and the possible future works are proposed.

2 Growth of graphene on copper by chemical vapour deposition (CVD)

2.1 Introduction

Graphene is considered to have a great potential to be utilized in a range of electronic devices including solar cells, field effect transistors, super-capacitors, batteries, displays and sensors due to its unique electrical, optical and mechanical properties [39-49]. Hence, a significant amount of research has been devoted to the synthesis of graphene since its large scale production with controllable parameters will be a key factor towards commercialization. Exfoliating graphene from graphite either mechanically [50] or chemically [51] creates small flakes, that are not suitable for applications requiring uniformity. High quality graphene can be synthesized epitaxially on the surface of a SiC substrate by desorption of Si atoms. [52] However, SiC epitaxy has intrinsic limitations for large area applications. Another method to produce graphene is to synthesize it on a metal catalyst substrate by chemical vapor deposition (CVD) [1, 14, 53-59]. Currently, CVD appears to have the most significant potential for large area production of graphene with a sufficiently high crystalline quality for optoelectronic applications.

The potential of CVD graphene in optoelectronics lies in the fact that it can have both high transparency and high conductivity at the same time. With its enormous flexibility, graphene is one of the outstanding candidate materials as a transparent conductive electrode for flexible electronics. Nearly 98% transparency of monolayer graphene is far superior to those required by most of the optoelectronic applications. However, obtaining a highly conductive graphene film with high stability is proven to be a challenge. Although single crystal graphene can have very high mobility as demonstrated in small mechanically exfoliated samples, larger sheets synthesized by

scalable methods such as CVD show much lower mobility values in most of the results. The sheet resistance of monolayer CVD grown graphene typically ranges from several hundred to a thousand Ohms per square [60-62]. The reduced conductance in CVD graphene is due to electron scattering from crystal domains and the defects inherently formed during its growth.

Copper and nickel are the most widely used transition metals for the metal-assisted CVD synthesis of graphene [63-66]. Material parameters, such as carbon solubility, crystal structure and lattice constant as well as the thermodynamic parameters affect the deposition of graphene on the surface of a catalyst metal [1, 67, 68].

2.2 Growth of graphene on copper by CVD

After the first discovery of the growth of graphene by chemical vapor deposition (CVD) method on copper, [1] the variety of enhancements on the crystals size [2-5] and carrier mobility have been attained during last recent years [6]. This encouraged many studies on CVD growth mechanisms to find out a practical mass scale production technique for high quality graphene, fulfilling the economical and reproducibility concerns at the same time [2, 10-23]. Li et al. demonstrated that due to the very low solubility of carbon in copper, surface-adsorption governs graphene growth and makes it a self-limited process [10]. The growth terminates as soon as the copper surface is entirely covered with graphene since the active surface area on which to catalyze methane decomposition and supply the carbon source is lost. It has thus been suggested that besides the very low solubility of carbon in copper bulk, the high mobility of carbon ad-atoms on copper due to the weak surface diffusion barrier can boost the pure surface-based process mechanism [10, 14, 24, 25, 63].

CVD growth of graphene is generally explained, to begin with, the adsorption of a hydrocarbon molecule on a catalyst surface followed by its dissociation into active carbon radicals that diffuse on the surface until they agglomerate on defects. This local concentration continues to increase until the supersaturation level is reached and crystal nucleation has started on defect points (**Figure 2.1**) [23].

On the contrary, the average distance between nucleation sites defines the average size of crystal domains. Therefore, to reduce the total electron scattering from the crystal domains, suppression of the nucleation site for enlarging the average size of graphene crystals is essential.

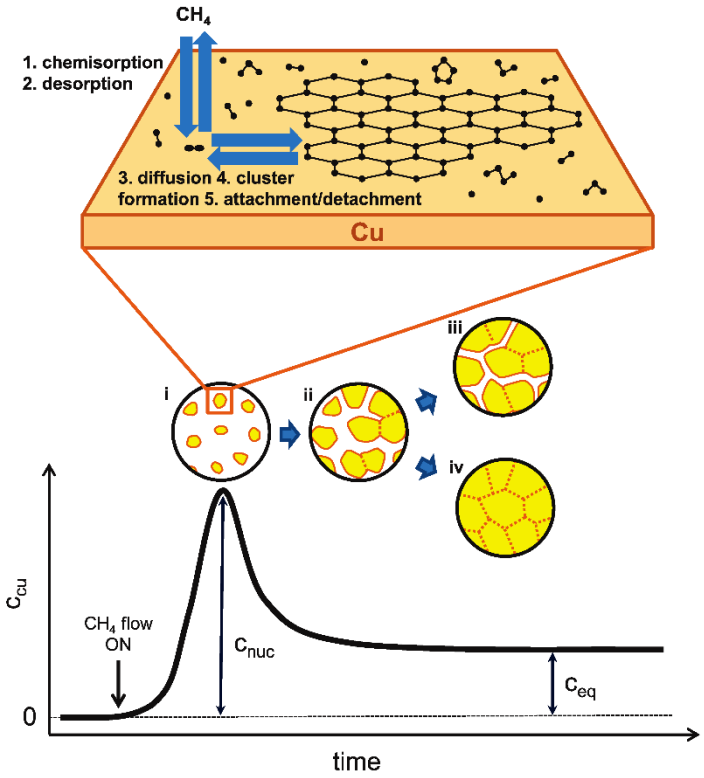

Figure 2.1: Schematic diagram for the nucleation and growth mechanism of graphene on a copper surface [23].

The adsorption and then dissociation of methane on the copper surface provides supersaturation of carbon adatoms on the surface. When the concentration of the active carbon species on copper (C_{Cu}) reaches a critical supersaturation point (C_{nuc}) nucleation, and growth of graphene domains are beginning (i). The growth rate is declining as graphene domains enlarging and covering more surface area of copper (ii). The growth process will be terminated either due to declining carbon radicals when the amount of below the supersaturated level (iii) or due to the merging graphene domains and losing all exposed surface area copper (iv).

The dramatic suppression of graphene nucleation attained by introducing oxygen to the CVD process has been a critical development towards the growth of high quality graphene. [2, 27] However, it has taken a while to understand the suppression of nucleation and its relation to the reduction of carbon content in copper foil. [19, 28, 29] It has been realized that, depending on the concentration, oxygen has contrary effects on carbon in the Cu foil which can be considered either as etchant or scavenger of carbon from the foil, [4, 19, 28] or as an impurity that raises solubility/diffusivity of carbon inside the Cu foil. [21, 27, 28]

Also, it has been noticed that the inconsistency of the nucleation density of graphene flakes on copper can originate from the presence of unintentional oxidative impurity gases in the CVD system. [4]

So far, a variety of studies have been focused on the role of *external* carbon sources, either in the form of precursor or contamination, on the nucleation and growth mechanism of graphene flakes (GFs). [10, 11, 14, 23, 60, 69-71] But still, they did not entirely clarify the subject. However, recently the critical role of carbon *inside* the copper foil on the nucleation of GFs is revealed in a few studies, [19, 28, 37] and implies that more studies are required in this area.

2.2.1 Growth of ad-layer graphene on copper

Despite the fact that the graphene growth on copper is predominantly monolayer, the formation of ad-layer graphene under certain conditions has also been demonstrated and discussed in various literature. [11, 17, 21, 72, 73] This ad-layer formation is attributed to high level precursor saturation, [72] the diffusion of active species into the interface between the as-grown graphene layer and copper or over the as-grown graphene layer through the boundary layer, [17, 73] and the diffusion of a very small amount of dissolved carbon into the copper, induced by oxygen impurities. [21]

Aside from the CVD conditions, qualities of the copper foil such as surface roughness, crystal domain size, and orientation, the density of defects and impurities are claimed to play an individual role in the formation of multilayer graphene. [60, 61, 74, 75] Previous studies argued that the presence of impurities increases the activity of a catalyst at its surface by enhancing the surface reaction rate. Therefore, the graphene thickness was locally increased in the vicinity of the impurities or surface defects due to the increased amount of dissociated carbon atoms. [17, 60, 76, 77]

Additionally, since for the monolayer graphene film grown by CVD on copper, the reported sheet resistance typically ranges from several hundred to a thousand Ohms per square [60-62], it seems to be a more viable approach to use multilayer graphene to achieve a better conductivity with a slightly reduced transparency within the acceptable limits. In that sense, multilayer graphene appears to be closer to meet the current 10-500 Ω/□ and 80-90% transparency requirements for a variety of electro-optical applications such as displays or touch screens. [17, 78-85]

However, growing the multilayer graphene on copper with a predetermined thickness and coverage still stands as an open problem as the number of layers of graphene and their coverage was not changing much after initial few minutes of growth time. [77, 86, 87] In this regard, a more in-depth understanding about the diffusion of carbon inside the

copper bulk can lead us to achieve a better controlled-conditions either for suppression or enhancing the growth of ad-layer/ multilayer graphene on Cu foil.

2.2.2 Experimental setup for chemical vapour deposition

For our experiments, we used a CVD system with a tubular furnace included an 11 cm inner diameter quartz tube (**Figure 2.2**). For each test, we used a 2×3 cm^2 sized Cu foil that was placed at the center inside the tube. The ambient gas is removed from the CVD system by three times pumping down to 10^{-1} mbar followed by flushing with argon to 300 mbar. Therefore, during the annealing process basically, the level of purity of the Ar and H_2 sources were the sole parameters determining the purity of the gases in the chamber. After this, when the system reached to a base pressure of 5×10^{-2} mbar the process was initiated by heating the system from room temperature to 1000 °C in 40 min, followed by an annealing phase at 1000 °C. Only hydrogen (99.999% pure) and argon (99.999% pure) were injected into the system during the heating up and annealing phases to treat the copper surface. The pressure of the chamber was tuned by a needle valve located between the tube exhaust and the pump.

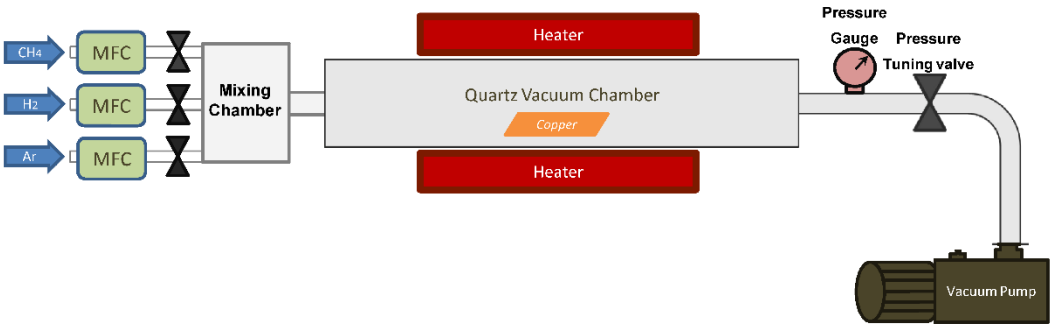

Figure 2.2: Schematic drawing of CVD setup for growing graphene on the copper foil

The chamber is pumped by an *Agilent TriScroll 300* dry pump (never been connected to any other pumps) to exclude external carbon contamination due to pump oil. [69] The CVD system was cooled to room temperature while maintaining the gas flow rates. The cooling of the chamber from 1000 to 200 °C took 10 min. In this work, we used a fresh quartz tube (99.998% pure, Yukang Quartz Ltd) for the annealing test experiments to exclude cross-contamination. Moreover, the tube was baked at 1000 °C for 2 hours under a 500 sccm flow of argon before the experiments. In that regard, to avoid any possible

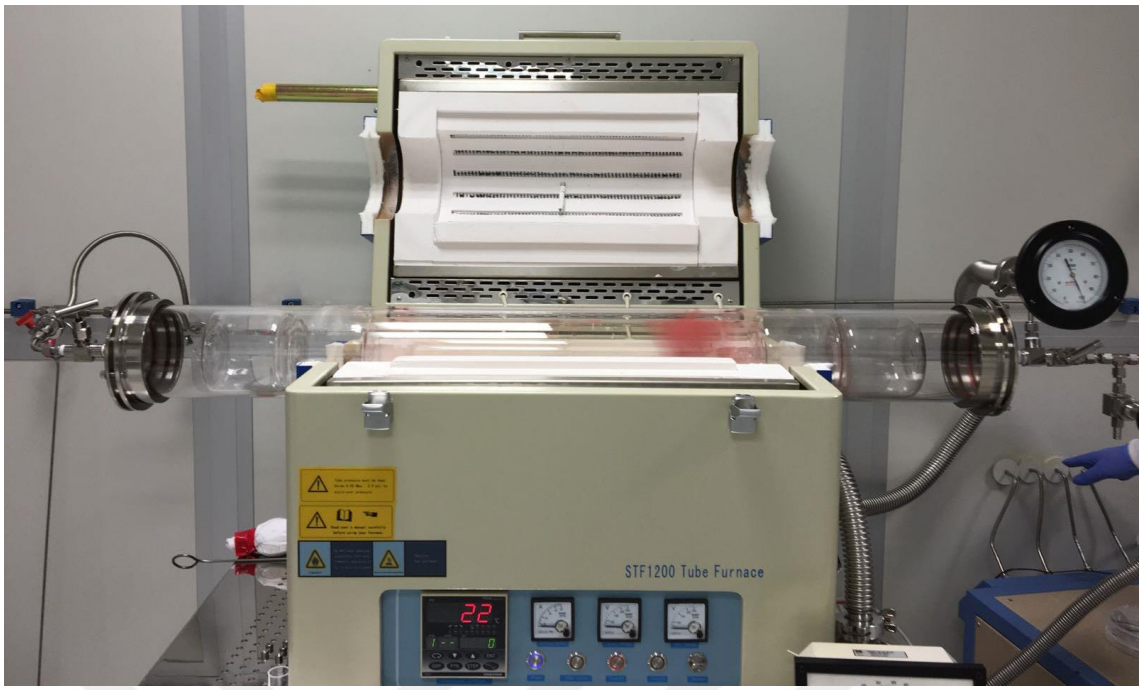

Figure 2.3: Experimental CVD setup for growing graphene on the copper foil.

effect of a pre-used external precursor, we used methane (CH_4) gas after finishing the whole annealing under test, in the final round of our experiments.

2.2.3 Graphene transferring

In order to inspect grown graphene in CVD process under an optical microscope or Raman spectroscopy system, it is very common to transfer graphene to on to SiO_2/Si substrates (see sections **2.3.1** and **2.3.3**). We choose the wet transfer technique which is the most widely used transferring technique for CVD graphene from the copper on to the SiO_2/Si substrates. [1, 88] First, a thin layer of poly (methyl methacrylate) (PMMA) (MicroChem 950 PMMA 2% in chlorobenzene) was spin-coated on the samples (**Figure 2.4(a-c)**) and baked at 180 °C for 5 min (**Figure 2.4(d)**). Then, the unintentionally grown graphene at the back-side of the foil was removed by oxygen plasma (**Figure 2.4(e,f)**). Next, the samples were placed in 0.1 M aqueous $(NH_4)_2S_2O_8$, overnight (**Figure 2.4(g-i)**). After the copper foil was etched away, the graphene film with PMMA support was transferred from the solution into deionized (DI) water. Three cycles of 10-min DI water rinsing were applied to wash away the remaining etchant. Then the film was picked up from water on a SiO_2/Si substrate (**Figure 2.4(j)**). Finally, the PMMA was dissolved using a hot acetone bath at 70 °C, rinsed with 2-propanol and dried with blowing compressed nitrogen (**Figure 2.4(k-l)**).

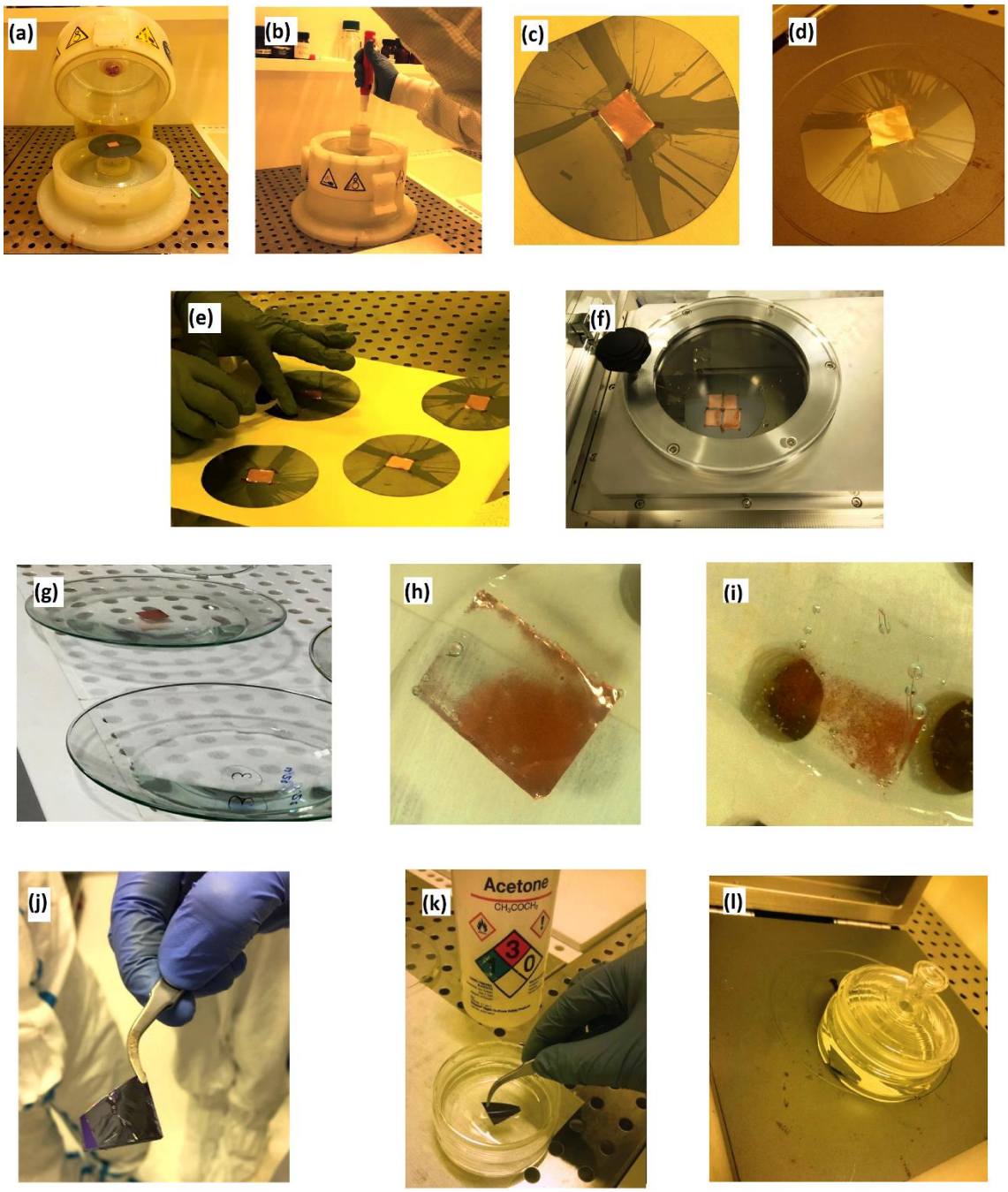

Figure 2.4: Experimental work flow of the wet transferring graphene film to SiO_2/Si substrate.

2.3 Characterization of graphene and growth procedure

2.3.1 Optical Microscopy

The simplicity of optical microscopy made it as the most common technique for inspection large area graphene samples. Practically, optical microscopy provides us a quick thickness examining before applying the accurate methods such as scanning and transmission electron microscopy (SEM), atomic force microscopy (AFM) or Raman

spectroscopy. [89, 90] Under optical microscopy a transferred graphene film on Si/SiO_2 substrate become visible since the interference color of reflected light is changing by graphene compared to the empty substrate **Figure 2.5**. A typical optical microscope in the visible light range can provide the magnification up to ×1500 that is theoretically limited by nature of light diffraction and therefore resolution limit of around 0.2 µm. How illuminating, positioning and the characteristics the specimen, all are effecting on the observed image with an optical microscope. Silicon wafer with a silicon dioxide layer (usually 300-nm thick) is the most widely used substrate that mono-layer graphene turns into a visible feature on its surface. This visibility is due to an interference of light between the graphene and the thin layer of SiO_2 and therefore enhanced absorption of light by graphene. [89-93]

Figure 2.5: Optical microscope images of transferred graphene on Si/SiO_2 substrate.

The different thicknesses in multilayer graphene sheet on Si/SiO_2 illustrate distinct optical contrast (left) [90]. Transferred graphene crystals on Si/SiO_2, produced by CVD method, with a uniform monolayer thickness (right).

Moreover, not only the changing in surface morphology and microstructure of copper foil, after treating under CVD process, can be traced with the aid of the optical microscope, but also the morphology of the grown graphene flakes on the copper surface and be inspected very quickly.

This can be down directly on growth copper foil by a simple thermal annealing treatment. Jia et al. have shown that due to heat treatment in ambient air the uncovered copper transforms to copper oxides while the covered part of copper by graphene remains intact. [70] This effect makes an interference color contrast between oxidized part of copper and the area covered by graphene; hence graphene easily turns to visible features in optical microscope images (**Figure 2.6**). This simple technique facilitated various

studies to find how involving parameters in CVD process affect graphene nucleation and growth. [70, 94-97]

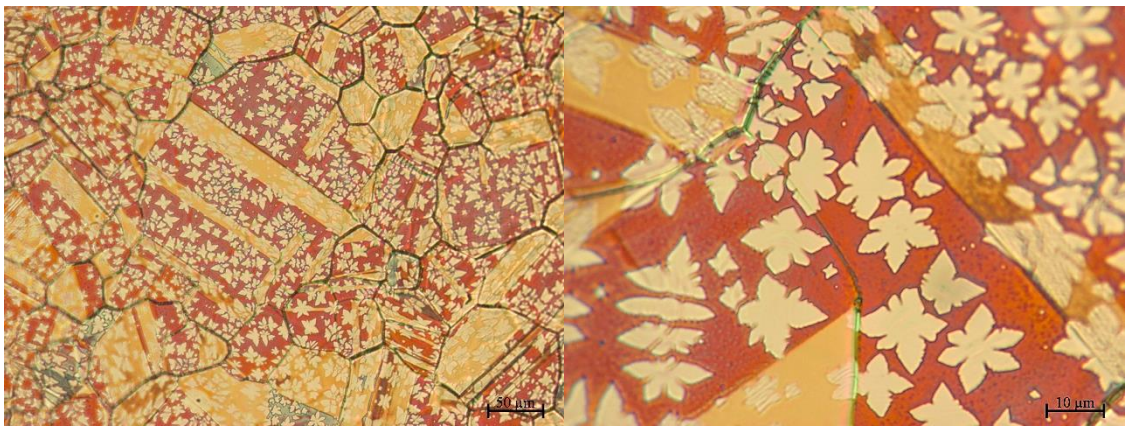

Figure 2.6: Optical microscope image of the surface of a copper foil after CVD process which is partially covered by graphene snowflakes

After 2 minutes of heating copper in ambient air at 180° C, the naked part of copper surface get oxidized and can be distinguished from the covered area by graphene flakes.

2.3.2 Scanning Electron microscopy

The wide range of magnification, large depth of field (focus), and relatively high resolution together with the convenient of usage are made scanning electron microscopy (SEM) as one of the most common tools for characterization of materials. In SEM interaction of incoming electrons with the matter near its surface generates secondary electrons (SE2) with an intensity that depends on the local properties of the surface. The signal from the SE2 detector and lateral coordinates of the primary beam is presented as a gray scale image that mimics the topography of the inspected surface. SEM's resolution is limited by the interaction volume of the electron beam within the sample as well as the diameter of the incoming electron on the probing surface.

In the area of graphene research, SEM turns to a predominant tool for the studies on CVD graphene grown on the transient metallic substrate. [17, 22, 37, 98-104] Compared to SEM imaging requirement, transferring the graphene to a dielectric substrate is essential for some of the characterization methods such as Raman spectroscopy. However, transferring of graphene will cost extra time and painful work and could introduce contamination, tears or cracks to the graphene which can interfere with characterization results and mislead us about the growth process. On the contrary, a variety of valuable information such as graphene domain (crystal) size, domain morphology, and surface coverage, the density of nucleation and growth rates can be achieved directly from SEM

without any need for transferring the grown graphene to another substrate. For example, using SEM, it has been realized that the shape of graphene domain depends on several parameters such as process temperature, the growth atmosphere, the partial pressures of involving gases, the catalyst substrate and the crystallographic orientation of the catalytic grains. [18, 22, 32, 71, 72, 104-108]

Although the determination of the exact number of graphene layers with SEM may not be an easy approach all the time; however, valuable information about thickness graphene is grown on copper can be attained from SEM in most of the cases. As can be seen in **Figure 2.7**, the color contrast changes explicitly when numbers of graphene layers change on the copper surface. This contrast is due to attenuation of secondary electrons by graphene layers and the different work functions of the surface covered by a different number of graphene layers. [99, 100, 109] Therefore from the area that is covered with less number of graphene more secondary electrons can be released and therefore appears with brighter color in the SEM images. On the contrary, the area that is covered with more layers of graphene is darker since the less secondary electron can survive from thicker graphene film. In general, graphene wrinkles, copper surface morphology and overall uniformity that can be traced in SEM image are the main simple features that give qualitative information about the graphene films on copper by CVD.

In **Figure 2.7** SEM images of some samples of CVD graphene film grown on copper are illustrated. As can be seen in **Figure 2.7 a and b**, growth is terminated before a full surface coverage. Therefore, we can obtain valuable information about the density of nucleation, the growth condition that provided six-lobed shape graphene domain, the average size of graphene flakes, and the emergence of ad-layers at the center of graphene flakes. Besides, in **Figure 2.7 c, d and e,** we see that after a full coverage of graphene wrinkles appears as a dark line on the surface, span over the copper surface and even pass the copper grain boundaries also twisted in some locations. These wrinkles, which are formed on the copper surface due to the negative expansion coefficient of graphene, facilitate tracing presence of monolayer graphene since it is pretty difficult to distinguish monolayer graphene from the substrate due to its uniform color. Moreover, in **Figure 2.7 c, d and e**, we can see some dark patches of multi-layer graphene with distinguishable grey shades that give us some insight about their thickness. Finally, we can observe graphene cracks that appear as bright stripe lines in **Figure 2.7 e**. The benefit of detecting cracks in

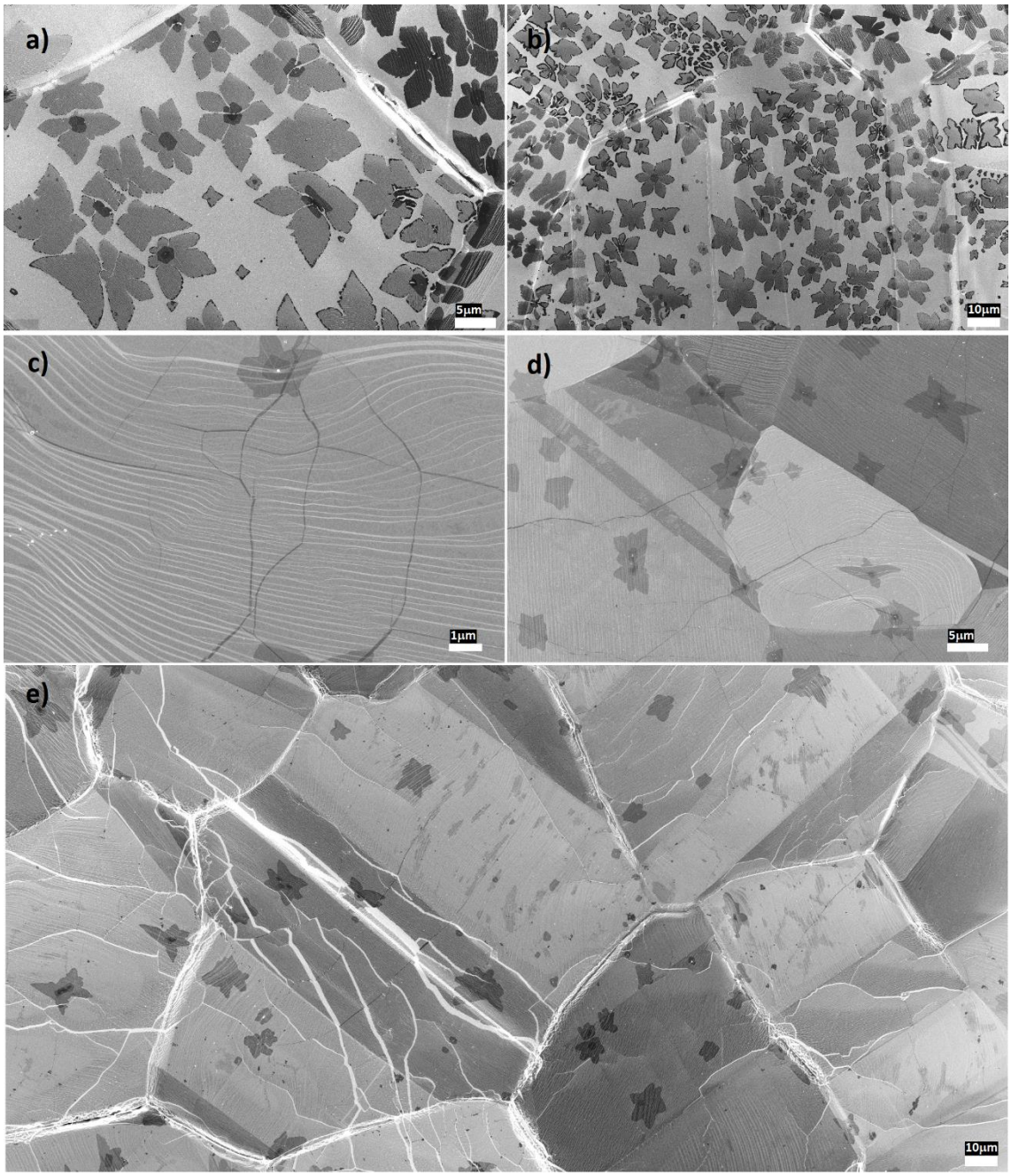

Figure 2.7: SEM images of graphene film grown on copper by CVD.

From the SEM image of a graphene film on copper we can inspect various parameters and characteristics of the film such as: density of nucleation (a and b), graphene domain shape (a and b), graphene wrinkles and therefore overall surface coverage (c-e), thickness uniformity and presence of multilayer patches (a-e) and cracks in the graphene film (e).

graphene film on copper by SEM is that we can distinguish it from the crack that can be produced on the graphene film after a failed transfer process on SiO_2/Si substrate.

Usually, the SEM systems are equipped with additional detectors such as energy dispersive X-ray spectroscopy (EDS), allowing for chemical analysis of the sample.

Therefore, the presence of some impurity features on the surface of copper after the CVD process can be inspected by EDS in the SEM system. In this thesis work, we used a *Zeiss Gemini 1530* SEM accompanied by an energy dispersive spectroscopy detector (EDS, OXFORD INSTRUMENTS X-Max^N) to structurally characterize the copper samples and graphene.

2.3.3 Raman spectroscopy

Raman spectroscopy is a nonlinear laser spectroscopy technique where the inelastic scattering of laser beam interacted with a sample, provides characteristic data about vibrational modes in the sample. This technique can be used to characterize verity materials either in solid, liquid or gaseous phase. In the Raman Effect, the frequency of the laser photons is changing when interacting with matter. Practically during this process, the incoming laser's photons first being absorbed by sample's atoms and exited its electrons to a higher energy level and then re-emits those photons with the same or different frequencies after relaxation of their electron to its ground energy level. In practice, most of the laser light scatters with the same frequency of incident beam and is considered as elastic scattering. However, a few portions of the scattered laser beam will be a frequency shifted or inelastic scattering and is called Raman scattering.

There are two types of Raman scattering, so-called Stokes scattering where increases the energy of scattered light (reduces the frequency) and anti-Stokes scattering that decreases the energy of scattered light (increases the frequency). From these frequency shifts, we can extract valuable information about vibrational or rotational energy states in the samples. [110]

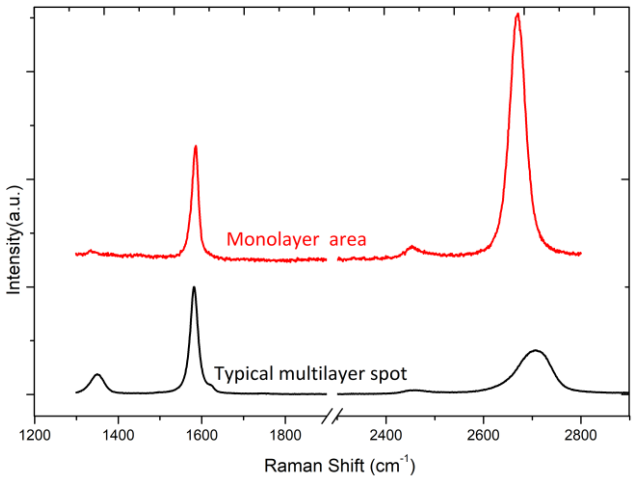

Figure 2.8: Raman spectrum of a typical monolayer and multilayer graphene

Over the years, Raman spectroscopy has always been one of the main tools for characterization of graphitic materials, [111-115] and therefore it turns to an important technique to investigate the electrons-phonons interaction in graphene film as well. [116-121]

In general, the Raman spectra of all of the carbon-based materials, such as fullerenes, graphite or conjugated polymers, contains a few important modes in the 1000–2000 cm^{-1} spectral range. [122] Specifically for the graphene, the variations in Raman spectrum versus the changing in the numbers of layers implies the changes in the electron bands and therefore provide a non-destructive way to distinguish single, bi-layer and few-layer Bernal stacked (AB) graphene. [118, 123] G mode and 2D mode are the main noticeable features in the Raman spectrum of graphene as are demonstrated in **Figure 2.8**, for a typical monolayer and multilayer graphene, obtained using a 532 nm laser beam. The G peak locates around 1580 cm^{-1}, and the 2D peak locates about 2680 cm^{-1}. Also, there is another peak that can be found around 1350 cm^{-1}, so-called D peak. Each of these peaks corresponds to a vibrational mode as follow: G peak represents the vibrational mode due to stretching of whole sp^2 atoms pairs, in both rings and chains, while the D peak represents the vibrational breathing modes of sp^2 atoms in rings. Due to symmetry, D mode is not an allowed transition in a perfect graphene crystal; however, this transition is allowed in the presence of a defect since it breaks the symmetry in graphene. The 2D mode is the second harmonic of the D mode, and since it corresponds a two-phonon transition process, it is not a forbidden by fundamental selection rules even in a perfect graphene crystal. [114, 124]

Since, position, shape and relative intensity of the G and 2D Raman modes change as the number of graphene layers changes; it can be used as a method to obtain the thickness of inspecting graphene sample. In **Figure 2.9** G and 2D modes of graphene samples up to four layers are demonstrated and compared to of graphite. [125] We can see the change in the shape of the 2D band as the number layers increases in which around four layers thickness, the profile of 2D become very similar to 2D of graphite. When the number of graphene layers increases, a combination of sub-components will involve in the profile of 2D mode and therefore changes the 2D mode's profile. Also, the more increase in the number of layers will cause a larger reduction of the relative intensity of 2D peak to the G peak. Therefore, for the samples with five layers or more, it would be difficult to distinguish it from graphite using Raman spectra. [114, 118, 123, 126]

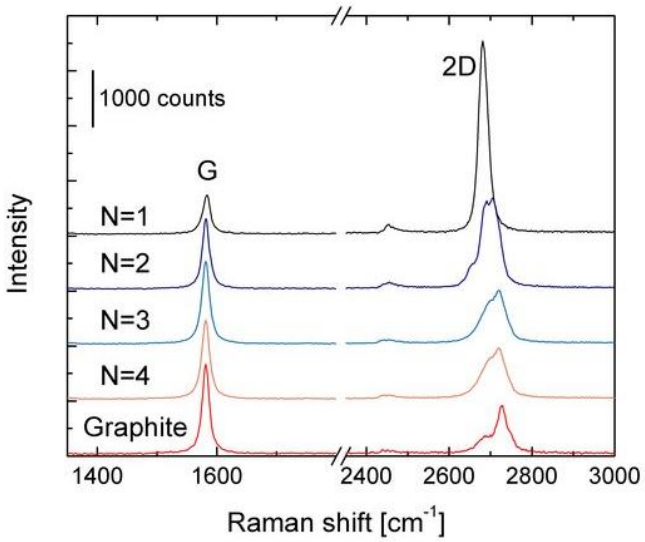

Figure 2.9: Thickness dependence of graphene Raman spectrum

2D peak in the Raman spectra of graphene become more similar to 2D of graphite as the number of layers increases. [125]

Here, we need to note that measuring the number of graphene layers from Raman spectra is a well-established technique just for the graphene samples with AB Bernal stacking. [118, 123] Usually, this kind of sample can be achieved from the mechanical exfoliation of highly oriented pyrolytic graphite (HOPG); however, we cannot always consider the AB stacking for the multilayer graphene produced by CVD technique. Therefore, further concerns in the width of the 2D peak, as well as intensity ration of 2D and G peaks, are required to adequately address the characteristics of CVD graphene based on its Raman spectra. [123, 127, 128]

In practice, to enhance the Raman signal and exclude the back reflection of the laser beam from copper, usually, we transfer graphene samples on a silicon wafer coated with 300 nm thick silicon dioxide layer. This provides us with a cleaner spectrum which can be easier to analyze. In this research, we used Raman spectroscopy (Renishaw inVia Reflex) to confirm the presence of carbon-based layers on the copper samples or after transfer.

2.3.4 Time of flight secondary ion mass spectrometry

Over the years, the ability to detect all elements of the periodic table by secondary ion mass spectrometry (SIMS) and its high sensitivity down to ppm level are made it as a unique technique for the materials analysis and characterization. Combining this technique with time-of-flight (ToF) measurement that can provide the mass spectra of the

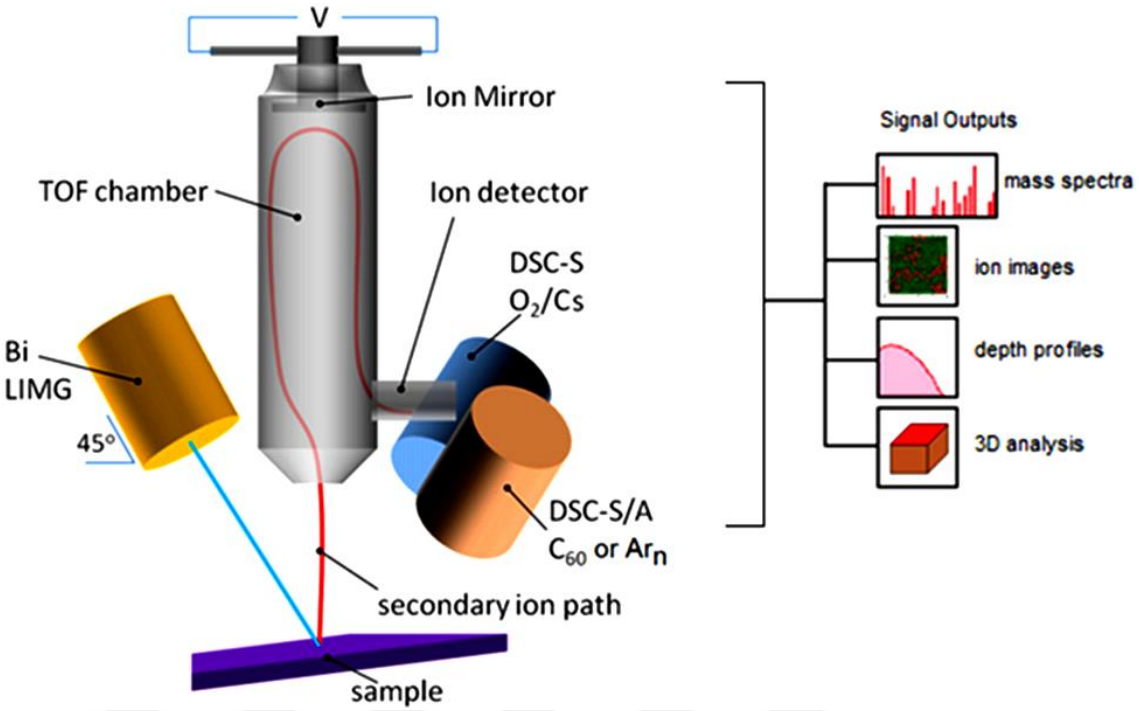

Figure 2.10: Schematic illustration of a dual-beam time-of-flight secondary ion mass spectrometer

Primary ion gun releases secondary ions from the sample. Then the secondary ions are extracted and detected in the flight tube. The outputs result can be in the form of mass spectra, 2D ion map, depth profiles or 3D ion analyses, depending on the operational mode of the system [129].

out-most part of the inspecting surfaces, applying low current ion beam (static SIMS), ends up with time-of-flight secondary ion mass spectrometry (ToF-SIMS) systems that can analyze and characterize the surface of materials in a high geometrical resolution [129, 130]. Since the tracing of carbon in the copper with a ppm resolution is one of the main focus in this thesis work, we used this technique to characterize the depth profile of carbon in the bulk of our copper foil samples, using a similar approach as a few other recent literature works [19, 38].

In ToF-SIMS first surface of the sample is bombarded with a beam of primary ions (with 0.1–20 keV energy). The ion bombardment of the surface produces the secondary ions that can have positive or negative charges that can be extracted from the surface by a bias voltage and directed to the detector of the mass spectrometry system. A schematic illustration of a dual-beam ToF-SIMS system is demonstrated in **Figure 2.10**. In a dual-beam system first secondary ions are generated by primary ion and then analyzed by ToF detector; then the second ion beam will sputter the surface for controlled etching of the sample. This controlled etching process enables the system to characterize the composition of the sample from the surface to its bulk.

For generating the secondary ion, the emitted ions from the primary ion gun are collimated and accelerated to the desired energy. Then it will be focused, and raster over the surface of the sample and therefore some part of primary ion's momentum will be transferred to the particles on and close to the surface (**Figure 2.11**). During this process an atom or an atoms cluster that earn required energy with a proper momentum direction, can to overcome the binding energy and leave the surface and are called secondary ions.

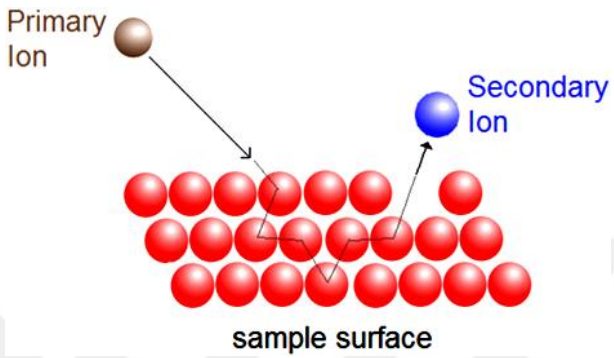

Figure 2.11: Schematic drawing for generation of secondary ion due to the impact of the primary ion to surface atoms

After the collision, the momentum of the primary ion is transferring to the sample surface and then distributed between different atoms. As a result of this process, the surface atom can be ejected as a secondary ion. [130]

In the dual-beam ToF-SIMS systems, a liquid metal ion gun/source (LMIG/S) is the most common source of the primary ion beam. These type of ion sources provides a well-focused ion beam and therefore high lateral resolutions in the case of secondary ion mapping. The initial LMIGs were gallium or gold based LMIG but then the bismuth-based ion sources become dominated primary ion source since the yield of secondary ion is enchased using this source. [131-133]

As soon as generating the secondary ions they should be separated in terms of their mass to charge ratio ($^{m}/_{z}$) to obtain the mass spectrum. The most commonly used mass analyzer is the ToF system, where the secondary ions are distinguished from their flight time in a flight tube. Practically, as the extremely short pulses of the primary ion beam raster the surface of the sample, the secondary ions pulses from the sample surface are created. The secondary ions pulses are accelerated via an electrostatic extraction plate with a constant potential, V, usually around 2 and 8 KeV heading to the ToF measuring section. Therefore, the kinetic energy of the secondary ions can be formulated with the value of $KE = (\frac{1}{2})mv^2$; then accelerated ions lead to a field free tube (the flight tube),

with the length of L, therefore the mass separation (m/z) can be obtained according to the following equation.

$$\frac{m}{z} = \frac{2Vt^2}{L^2} \quad (2.1)$$

That V is the accelerating potential, L is the length of the flight tube, and t is the time that takes the ions to fly in the flight tube and hit the detector (considering $= \frac{L}{t}$, and $KE = Vz$). Thus, time-of-flight of the secondary ions is proportional to square root of (m/z), which means lightest ions will arrive first to the detector and heavier ions move slower and riches to detector later time sequence.

As a result, the mass spectrum from each pulse of the secondary ion beam can be calculated from equation (2.1) in terms of flight time. The time-of-flight mass analyzer can easily be self-calibrated according to the light mass ions since they always exist in the in the system and the spectra.

In many cases, it is essential to study composition variation through the depth of the specimen. The main steps of depth profiling for a dual-beam ToF-SIMS system are illustrated in **Figure 2.12**. In the first step, (**Figure 2.12** (a)) sputter beam rasters the predefined sputter area. Usually, the sputter ion beam is delivering much higher current than of primary ion beam; therefore it removes material from the surface in a controlled regime. Then analytical (primary) ion beam bombarding a smaller area (sub-crater) within the sputter crater (**Figure 2.12** (b)) and producing the aforementioned secondary ions. Analyzing the smaller area (sub-crater) is to avoid 'edge effect' which can be caused by the interference of material from the edge of the sputtering region. When the secondary ions are collected into the ToF analyzer (**Figure 2.12**(c)), the sputtering and primary ion beam analysis will be repeated sequentially until reaching the desired depth.

Each of secondary ion pluses produces a mass spectrum (**Figure 2.12**(d)) therefore the peak values of desired atomic or molecular ions can be plotted versus depth of sample (**Figure 2.12**(e)).

For the depth profiling of the carbon content in our copper samples, we used TOF SIMS 5 (ION-TOF GmbH). To avoid edge effects on the generated spectra, SIMS measurement is performed by analyzing a 150 × 150 μm^2 area at the center of a 400 × 400 μm^2 sputtered region. 2 keV Cs^+ ions with 70 nA current is used during the sputtering cycle and spectra

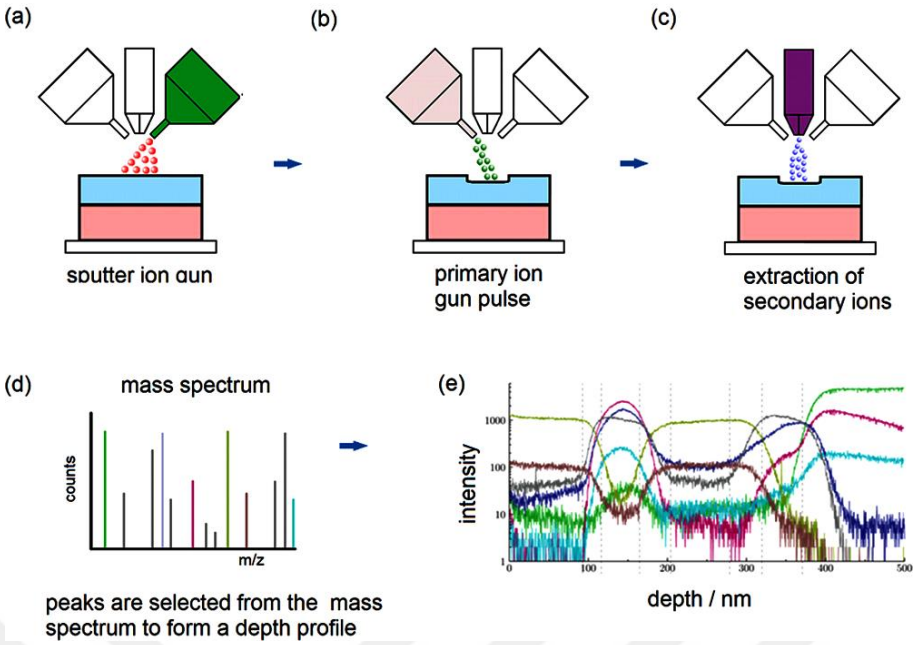

Figure 2.12: Main steps of depth profiling in a dual-beam ToF-SIMS

First A high energy sputter beam rasters the predefined sputter area (a). The primary ion beam is bombarding a smaller area (sub-crater) within the sputter crater and producing secondary ions (b). The generated secondary ions are extracted into the ToF analyzer (c) and produce mass spectrums (d). From the peak values of each species, its depth profile can be traced (e). [129]

are obtained by using a 25 keV Bi^+ ion beam after each sputtering cycle. The ion current of Bi^+ was 1.5 pA in the interlaced mode with a cycle time of 100 µs. We omitted the detected ions from the top 1.9 nm of the samples to exclude the contribution of adsorbed carbon from ambient air. This depth was determined from the local minimum of the CH^- ions signal during depth profiling. [19]

2.3.5 Other characterization techniques

In addition of the characterization techniques implemented in this research work and described in this chapter, there are many other techniques such as: Transmission Electron Microscopy (TEM), Scanning Tunneling Microscopy (STM), Atomic force microscopy (AFM), [98] X-ray photoelectron spectroscopy (XPS), [134] and Optical Transition Spectroscopy, [17] that can be used to characterize the different aspects of CVD graphene, and its growth process depends on the focused area of the research.

3 Spontaneous nucleation of graphene flakes (SNGFs) on copper foil in absence of external carbon

3.1 Introduction

In this chapter, we reveal the role of intrinsic carbon diffusing out from the copper foil upon nucleation and growth of graphene crystals when other sources of carbon contamination were meticulously avoided. As a result, for the first time, to our knowledge, we demonstrate the growth of micron-sized graphene flakes (GFs) on copper foil up to the near full surface coverage in the absence of any external carbon source. To measure the carbon content in the Cu foils, we used time-of-flight secondary ion mass spectrometry (ToF-SIMS) technique, which has a high mass resolution power ($\approx 10^5$) at a ppm level of elemental detection. We show that before the beginning of the graphene growth phase, hydrogen induces migration of carbon atoms from inside copper foil towards its surface (H-assisted C depletion). [37]

The intensity profile of the carbon content versus depth in Cu foils measured with ToF-SIMS provided not only direct evidence for the presence of intrinsic carbon within the bulk of copper foil, but also confirms the depletion of carbon from the bulk towards the surface of Cu foil assisted by H during annealing.

As it will be discussed in detail in sections **3.3, 3.5**, and **4.2**, we observed three possible consequences of hydrogen-induced carbon depletion depending on the hydrogen partial pressure: (i) growth of a disordered graphitic layer on copper; (ii) nucleation and growth of graphene flakes from carbon impurity trapped in the copper bulk. (iii) etching/reducing carbon from copper surface/bulk. Our experiments indicate that the use of low hydrogen concentration in a CVD process makes the second consequence to be the most likely outcome. This leads to an uncontrolled spontaneous nucleation of graphene flakes

(SNGFs) during the annealing phase, before any carbon precursor is fed into the system. This premature growth leads to an increased density of nucleation sites and, hence, reduces the average crystal size and quality of graphene films.

The systematic work presented in this paper on the H-assisted C depletion mechanism unveils an important detail about the origin of the nucleation of graphene crystals and elucidates the relationship between the nucleation density and process parameters.

3.2 Experimental approach

25 μm-thick ultra smooth Cu foils (<0.2 μm roughness, 99.8% metallic pure LiB grade, P.N. B1-SBS) purchased from Taiwan copper Foil Co. LTD. were used for main experiments. In addition, 99.999% metallic pure copper foil (25 μm thick purchased form Alfa Aesar, P.N. 10950) representing different levels of purity was used for comparison. Both types of Cu foils are not oxygen free. For each test, the 2×3 cm^2 sized Cu foil was placed on a 10 cm diameter quartz tube centered inside the main tube (to provide a uniform gas flow over the foil). After removing ambient gas is from the CVD system, when the base pressure reached to a of 5×10^{-2} mbar the process was initiated by heating the system to 1000 °C in 40 min, followed by an annealing phase at 1000 °C. To treat the Cu foil, simply hydrogen and argon were used during the heating up and annealing phases.

Although we meticulously avoided any carbon contamination in our CVD setup (as described in **section 2.2.2**), annealing of copper foil under relatively high concentrations of hydrogen ambient led to the formation of *graphitic films* on its surface. A series of annealing tests and ToF-SIMS depth-profile measurement of carbon in the Cu foils confirmed the presence of intrinsic carbon and its depletion to the surface during hydrogen annealing (H-assisted C depletion). However, under lower hydrogen pressure, graphene flakes were nucleated and grown without any external carbon precursor. In fact, we realized that due to the depletion of carbon from the bulk to the surface of the copper foil, the formation of nucleation sites on the surface is initiated during the annealing phase before any external carbon precursor is introduced. The details of our results are described in the following subsections.

3.3 Presence of intrinsic carbon and its depletion from copper foil

In the first set of experiments, three samples of copper foil were used to investigate the effect of hydrogen partial pressure on the depletion of intrinsic carbon during annealing.

The first two samples were annealed for 20 min under the hydrogen partial pressure values of 0 and 6 mbar and labeled accordingly as P-0 and P-6, respectively. To avoid restructuring the surface of P-0 and forming cuprous oxide (Cu_2O) due to oxygen impurities as the temperature descends, P-0 was cooled down under 6 mbar hydrogen.

The details of the annealing conditions are given in **Table** 1 and **Figure 3.1** display the SEM images of the corresponding samples after annealing. The annealing of P-0 caused some changes in the morphology of the copper surface such as the enlargement of the copper grains and reduction of the native oxide layer (**Figure 3.2)**, as expected.[135] However, there is another noticeable change in P-6 which is annealed under a hydrogen atmosphere; the emergence of a dark thin film fully covering the surface of P-6 as well as black spots scattered over it as seen in **Figure 3.1 b.**

To further verify the assessments from the SEM results about the thin film coverage on the surface of P-0 and P-6, they were also tested by ambient oxidation by heat treating at 180 °C in air for two minutes.[70] As their optical images are given in **Figure** 3.3, the surface of P-6 is protected, while the surface of P-0 is oxidized in the air. This hinted at a carbon-based layer on the P-6 sample, similar to the graphene film grown on a Cu foil.

Table 1: Annealing Parameters for Samples P-0, P-6, and P-0-6

Without using any external carbon precursor, a disordered graphitic (DG) film is formed on the surface of P-6 due to diminishing oxygen scavenging mechanism using H_2 flow from the beginning of annealing.

sample	annealing time (min)	H_2:Ar flow rate (sccm)	process pressure (mbar)	H_2 pressure (mbar)	figure	surface
P-0	20	000:500	15	0	Figure 3.1a	bare
P-6	20	200:500	21	6	Figure 3.1b	DG film
P-0-6	0-20 min	000:500	15	0	Figure 3.1c	bare
	20-40 min	200:500	21	6		

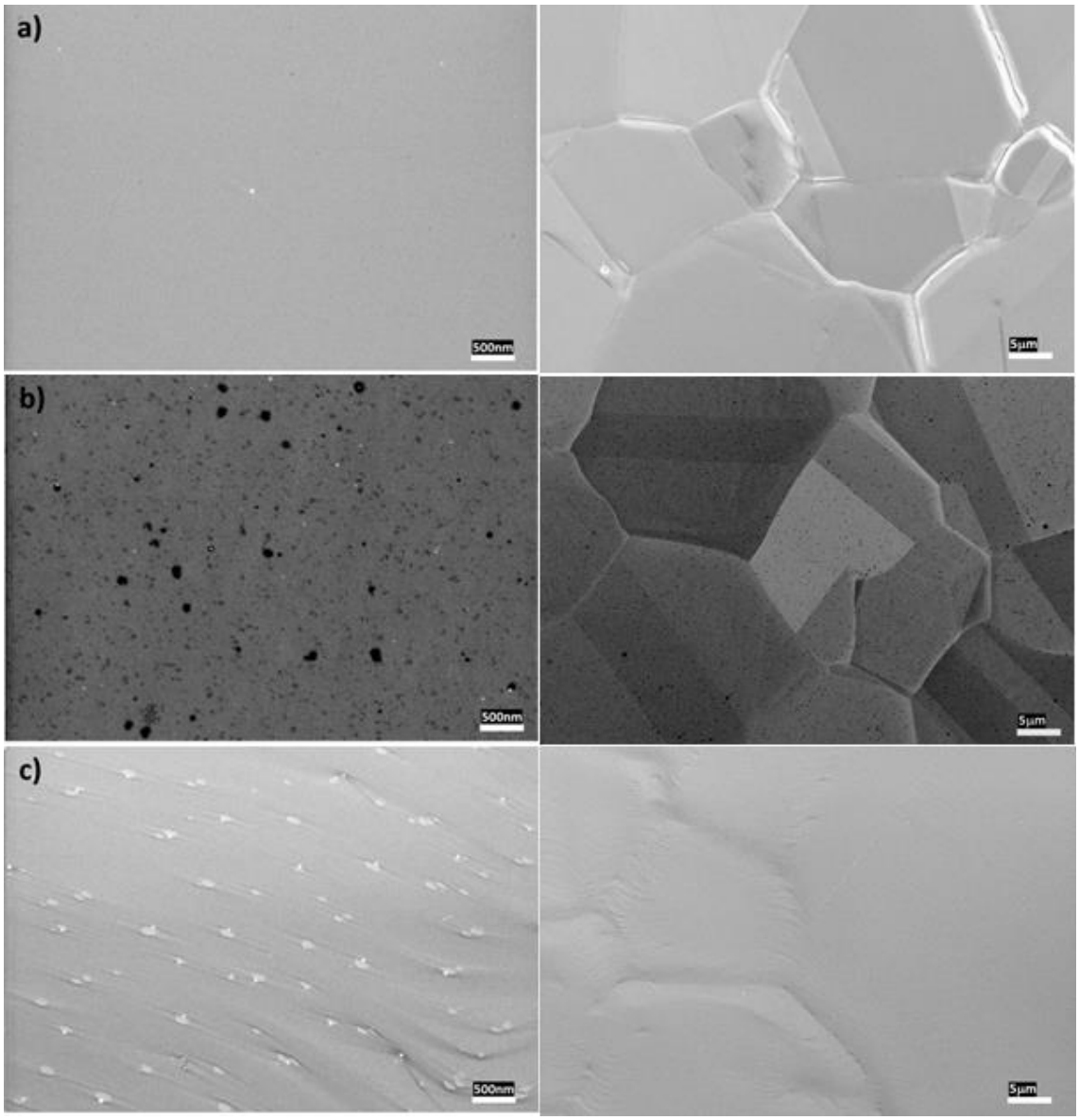

Figure 3.1: SEM image of the sample P-0, P-6 and P-0-6 in different magnifications

(a) SEM image of the sample P-0 surface after 20 min annealing under argon flow with no hydrogen. No specific feature can be seen on P-0 surface except for a few white spots identified as silicon oxide particles. (b) The SEM image of the sample P-6 surface after 20 min annealing under 6 mbar hydrogen pressure. The copper surface is fully covered by a graphitic thin film and darker spots signify denser graphitic features. c) The SEM image of the sample P-0-6 surface which was first annealed just as P-0 and then as P-6 in the same cycle; its surface shows no carbon features on it. During the first 20 min of annealing without hydrogen, carbon impurities were scavenged by oxidative impurities, thus, during the second 20 min annealing phase under hydrogen no graphitic thin film could be grown due to absence of carbon supply.

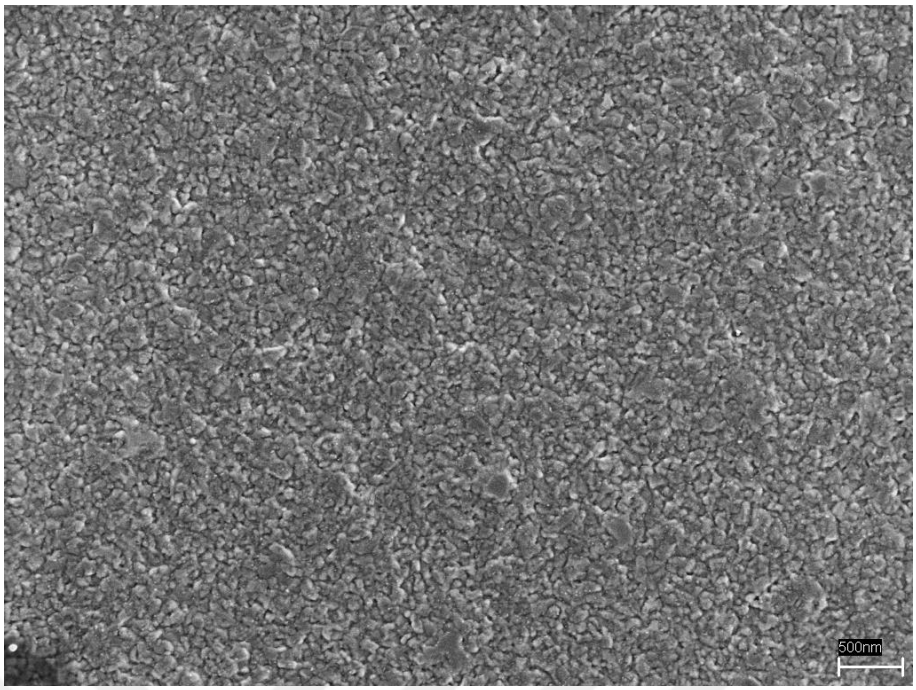

Figure 3.2: SEM image of untreated as received copper foil with its native oxide layer.

These results hinted at a carbon-based film formation on P-6 similar to a graphene film grown on Cu foil, but no film on the P-0 surface. Raman spectra of P-0 and P-6 samples before and after transfer confirmed these observations; D and G peaks of the Raman spectra of P-6 illustrated in **Figure 3.4** manifest a disordered graphitic structure [114]. On the contrary, Raman spectra of P-0 has no feature. No carbon precursor was used during the annealing and any external carbon contamination was rigorously prevented. To exclude any possibility of carbon deposition originating from the impurities in hydrogen gas, we performed a control experiment on a third sample (P-0-6), comprising a two-step annealing process as follows: during the first 20 min of annealing, no hydrogen was used as in the case of P-0, then the annealing was continued for another 20 min under 6 mbar hydrogen partial pressure as P-6. The bare surface of P-0-6 at the end of the process as can be seen in **Figure 3.1c** and **Figure 3.3f** verifies that the growth is not from carbon contamination, neither in hydrogen gas nor from other external sources. We conclude that the carbon atoms emerged on the P-6 surface originated from the copper foil itself. In **section 3.4** we propose a microscopic mechanism leading to the depletion of carbon in P-0 and P-0-6 and carbon film formation on the P-6 surface.

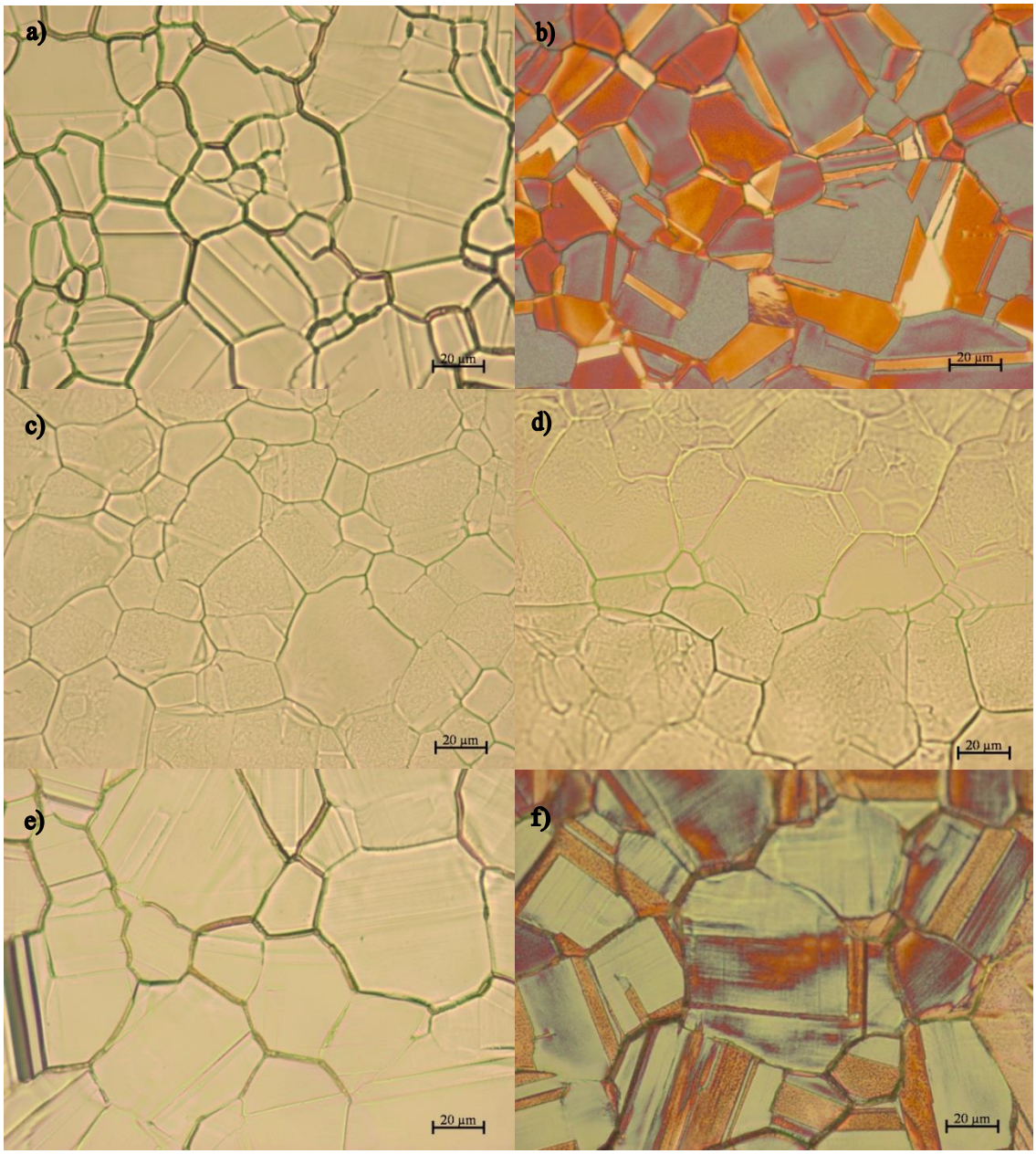

Figure 3.3: The optical image of P-0, P-6 and P-0-6 surface before (left) and after (right) heating at 180 °C.

The optical image of P-0 surface before (a) and after two minutes heating at 180 °C in the air (b). The oxidization of P-0 surface implies its bare and unprotected surface. The optical image of the annealed sample P-6 before (c) and after two minutes heat treatment at 180 °C in air (d). The copper surface was not oxidized since it is fully covered by a thin graphitic layer. The optical image of the annealed sample P-0-6 surface before (e) and after two minutes heat treatment at 180 °C in air (f). Similar to P-0, the bare surface of P-0-6 cannot be protected from oxidization.

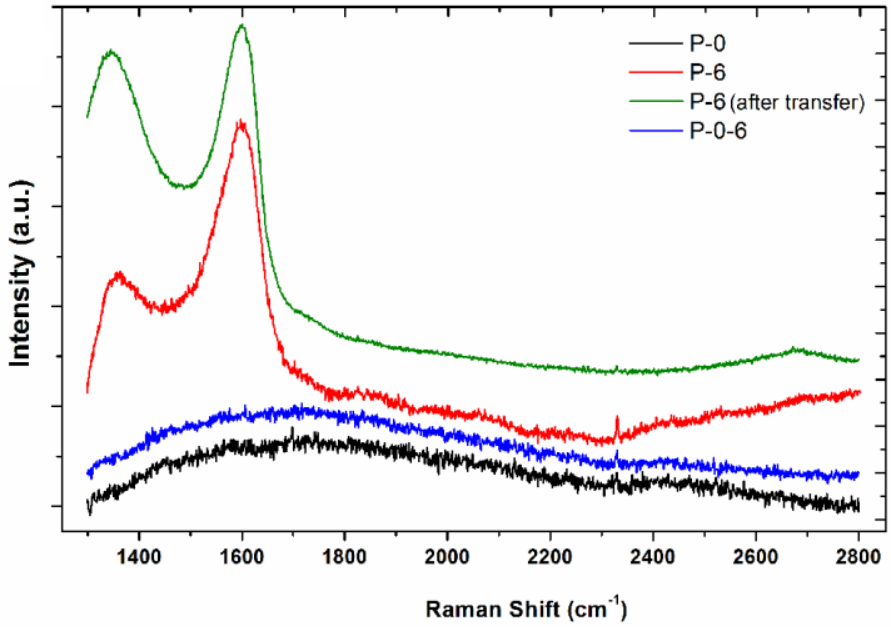

Figure 3.4: Raman spectra of P-0, P-6 before and after its transfer on a SiO_2/Si substrate, and P-0-6

D and G peaks, around 1350 cm^{-1} and 1600 cm^{-1} verify the presence of the disordered graphitic structure on P-6, however, no graphitic peak can be seen in the Raman spectra of P-0 and P-0-6.

Here, we also need to note that the bare surface of P-0-6 compared to P-6 confirmed the absence of carbon outgassing from the quartz tube, as the same quartz tube has been used for both experiments.

We performed ToF-SIMS experiments to directly verify the existence of intrinsic carbon inside the copper foil and its depletion to the surface during annealing under a hydrogen atmosphere. We determined the carbon concentration profile with respect to the depth from the surface on P-0, P-6, P-0-6 as well as the untreated copper foil (T-0). As it can be seen in the intensity profile of the C_2 ion in **Figure 3.5**, the carbon concentration in untreated sample T-0 rapidly declines as a function of distance from the surface within a few tens of nm depth. This data verifies the carbon content in copper and the profile with increasing concentration towards the surface supports the proposal that carbon is embedded in the Cu foil during the rolling and foil production process. This is somewhat similar to the process of mechanical alloying of carbon and copper.[136] Additionally, ToF-SIMS measured more than one order of magnitude above the background level carbon concentration well below the surface in T-0. The existence of carbon deeper in the foil may be connected with impurities initially existed in the copper material before the foil production process. In the P-0 sample, which was annealed for 20 min

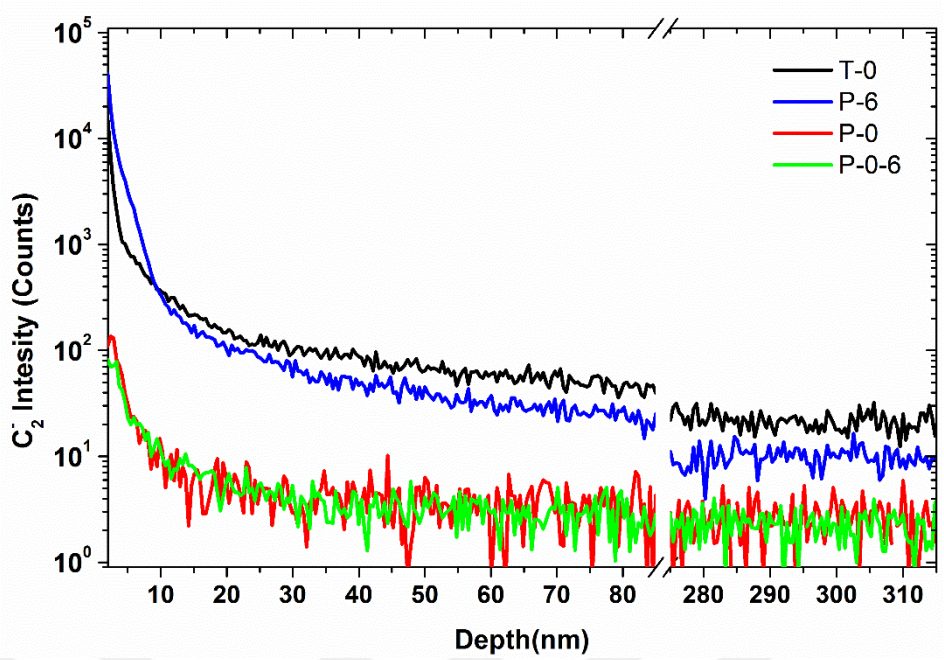

Figure 3.5 : Depth profile of C_2 intensity in T-0, P-6, P-0-6 measure by ToF-SIMS

Depth profile of C_2 intensity from ToF-SIMS in untreated copper foil (T-0) reveals a high concentration of embedded carbon near the surface. Reduction of C_2 intensity in depth profile of copper foils after annealing confirms out-diffusion of embedded carbon atoms during annealing. Annealing of copper foil in the absence of hydrogen releases carbon atoms from P-0 and P-0-6. However, annealing P-6 in the presence of hydrogen makes the out-diffusing carbon atoms to be accumulated near the copper surface raising carbon concentration in the region near the surface (0-10nm). The similarity of C_2 depth profile in P-0-6 to the depth profile of P-0, verifies the absence of the carbon content in hydrogen.

without hydrogen, we observe that the carbon profile has undergone a significant change. The carbon level is reduced throughout the measured depth and, in particular, there is two orders of magnitude reduction in the carbon level near the surface of P-0 compared to the untreated foil, T-0. In contrast, 20 min annealing of P-6 under 6 mbar hydrogen increased its carbon concentration near the surface. Also, compared to P-0, there is less drop in the carbon level of P-6 below 10 nm. The very similar depth profile of P-0-6 to P-0 implies a similar mechanism for the reduction of its carbon content during its first 20 min annealing step and no effect of hydrogen during its second step of annealing. Such a transformation in the carbon profile demonstrates a total depletion of carbon from copper foil in the absence of hydrogen during annealing but the migration of carbon from the bulk of copper foil towards its surface during annealing in the presence of hydrogen.

3.4 Proposed microscopic mechanism for hydrogen-assisted carbon depletion (HACD)

Here, we propose a microscopic mechanism that causes the intrinsic carbon to migrate and accumulate on the surface of copper foil in the presence of hydrogen as in the case of sample P-6. At elevated temperatures on the surface of Cu, H_2 dissociate to its atoms and dissolve in the copper bulk and releases carbon from C–O–Cu bonds and depletes oxygen in the form of H_2O vapor [137]. This process reduces the chance of intrinsic oxygen to scavenge the carbon. Reducing oxygen from the C–O–Cu bonds in the copper bulk with hydrogen leads to the formation of C–C molecules, C_xH_y clusters or individual C atoms. Carbon clusters cannot be accommodated in the copper lattice. Also, in the absence of oxygen C atoms cannot easily dissolve in copper [21, 138]. Therefore, they have to leave the copper matrix and are expelled to the surface or to the grain boundaries. As a result, the carbonic compounds segregate to the surface and agglomerate during annealing under hydrogen. This proposed mechanism also can explain the earlier observation of the hydrogen dependency of carbon dissolution and out-diffusion in the copper film, during the growth of graphene but from the external carbon precursor [139]. When the local concentration of carbon atoms on the copper surface reaches the supersaturation level, nucleation of a graphitic film will start [23, 26].

In the of case annealing in the absence of hydrogen, intrinsic oxygen impurities bond with carbon atoms in the bulk and form volatile CO or CO_2 gas to leave the bulk [19]. This process efficiently depletes carbon and no carbon film formation occurs on the P-0 surface.

We tried to reach both copper foil suppliers to learn further details about production method and the pre/post-processing of the foils, however, none of our suppliers provided us any details.

In general, we believe the intrinsic carbon embedded inside the copper foil may be originated from the following sources:

a) Carbon in the initial copper block before it was rolled into foil. Although the solubility of carbon in pure copper is very low, the presence of oxygen impurity elevates the dissolution of carbon in copper [21]. Therefore, in case of oxygen rich copper, presence of carbon in the final foil products seems to be feasible. However, the copper foil producers are mostly concerned about the metallic impurities rather than carbon.

b) Carbon may embedded inside the copper foil due to mechanical alloying of carbon and copper during rolling process [136].

c) The diffusion and adsorption of organic gases from ambient into copper gain boundaries during shelf life can be another source of carbon inside the copper bulk. The foil production process may lead to trapping of this carbon in between Cu grain boundaries due to mechanical changes in the grain geometry or aforementioned mechanical alloying mechanism.

All in all, the carbon and oxygen trapped inside Cu grain boundaries, voids, or any imperfection sites of Cu during the foil production or shelf life, that may not be even chemically bonded to the Cu. Oxygen can also scavenge the carbon inside the Cu foil in the absence of hydrogen during annealing. However, introducing hydrogen into the CVD system with high enough concentration can diminish that process and keep carbon in the bulk. Regarding the declining profile of carbon in untreated copper foil, T-40, we believe items (b) and (c) are the dominant causes for presence of carbon inside the copper foil. However, proposing a detailed discussion about origin of carbon inside the copper foils, requires a systematic study in collaboration with cooper foil suppliers and inspecting each step of their production presses.

The results of SEM and ToF-SIMS analyses obtained from the sample P-0-6 are also entirely consistent with the above microscopic mechanism we proposed. During the initial phase of annealing under the same conditions as sample P-0 oxygen scavenging releases the carbon off the sample. Therefore, in the second phase of annealing done under the same conditions as sample P-6, the H-assisted C depletion mechanism becomes no more relevant simply due to the absence of carbon. Therefore, ToF-SIMS results perfectly match for P-6 and P-0-6 samples as can be seen in **Figure 3.5**. Consistent with this mechanism and ToF-SIMS results, we observe no carbon film formation detected on the P-0-6 surface in the SEM images. This test also proves that there is no role of any external carbon in the process. **Figure 3.6** displays a schematic diagram that summarizes the effect of the H-assisted C depletion mechanism on copper foil under various H_2 concentrations.

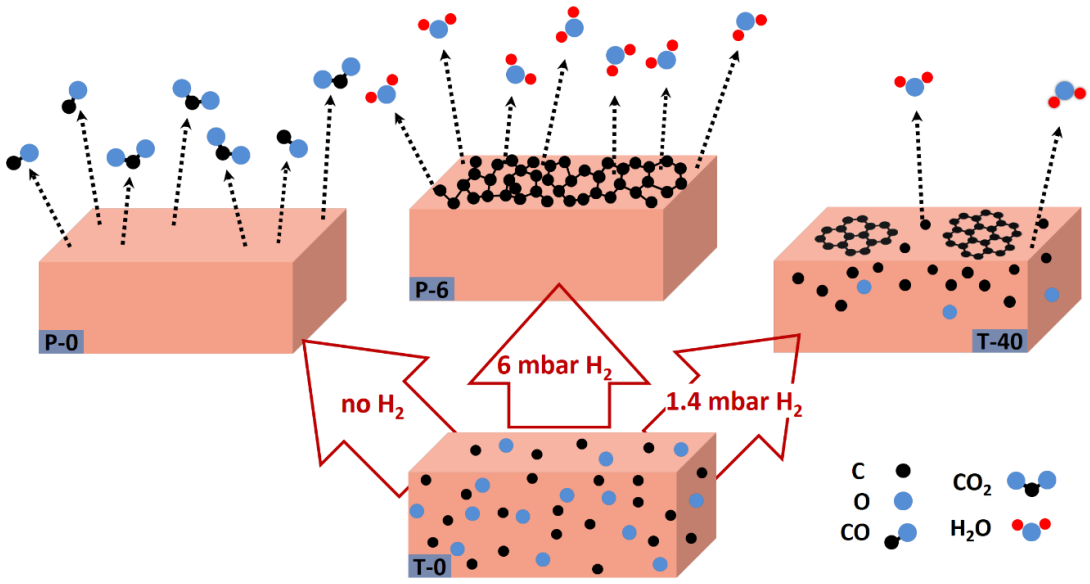

Figure 3.6: schematic diagram that summarizes the effect of the H-assisted C depletion mechanism on copper foil under various H_2 concentrations

Effect of H-assisted C depletion mechanism on copper foil under various H_2 concentrations. Annealing in the absence of hydrogen leads to bonding of intrinsic carbon atoms with oxygen impurities, form volatile CO or CO_2 gas and leave the bulk (P-0). This process efficiently depletes carbon and no carbon film forms on the surface. Annealing under low H_2 pressure (1.4 mbar) slowly depletes the C atoms from the bulk, hence few locations on the surface could reach supersaturation and nucleation threshold leading to the formation of GFs (T-40). Annealing under higher H_2 pressure (6 mbar), the rate of C depletion is increased such that the whole surface is supersaturated simultaneously, and a disordered graphitic structure is formed without a long-range atomic order (P-6)

3.5 Nucleation and growth of graphene from intrinsic carbon

The quality of the graphene film grown by CVD is directly connected with the density of nucleation sites; denser nucleation leads to smaller crystals and lower quality graphene films. Therefore, preventing uncontrolled generation of nucleation sites is essential to improve the CVD process. In this section, we explain our investigation on whether the segregation of intrinsic carbon on the copper surface may generate nucleation and growth of graphene. On the basis of on our proposed mechanism, it is expected that the H-assisted C depletion during the annealing process runs at a faster rate under a higher hydrogen concentration. Therefore, the formation of the disordered graphitic film on sample P-6 should be due to the rapid depletion of carbon species under relatively high hydrogen partial pressure.

Under lower H_2 partial pressure, the out-diffusion rate of C is reduced and its sudden supersaturation is inhibited. Instead, the nucleation and growth of graphene flakes (GFs)

is initiated at sparsely distributed supersaturation points. In other words, this provides the growth of a graphitic layer with a longer-range atomic order (as schematically demonstrated in **Figure 3.6**). Sample T-40 was annealed under reduced hydrogen partial pressure of 1.4 mbar and for an extended annealing time of 40 min (**Table** 2), to attain a growth condition for GFs with a large enough size to be observed. **Figure 3.7a** display the SEM images of the surface of the sample T-40 after annealing. Rather than the disordered graphitic layer seen in sample P-6, micron-sized GFs are formed on the surface of T-40 due to the reduced carbon supply rate from the copper bulk. The rate of graphene

Table 2: Annealing parameters and the calculated graphene surface coverage and nucleation density for the samples T-40, T-80, T-100, T-40E, and HP_T-40E.

Samples annealed under low hydrogen pressure exhibited nucleation and growth of graphene flakes instead of graphitic film formation. Sample T-40E was initially subjected to a chemical etching process to remove any surface carbon and then was undergone the same annealing process as T-40. Nucleation and growth of graphene flakes on T-40E just as in the case of the unetched sample T-40 excludes the effect of surface carbon.

sample	annealing time (min)	H_2:Ar flow rate (sccm)	process pressure (mbar)	H_2 pressure (mbar)	figure	graphene surface coverage (%)	graphene nucleation density (10^5 mm^{-2})
T-40	40	50:500	16	1.4	Figure 3.7a	33	6
T-80	80				Figure 3.7b	63	6
T-100	100				Figure 3.7c and Figure 3.8	85	6
T-40E	40				Figure 3.12	22	2
HP_T-40E	40				Figure 3.13	20	0.2

growth is rather low, that is, after 40 min of annealing only 33% of the surface of T-40 is covered by GFs. To determine if full graphene coverage can be achieved, samples T-80 and T-100 were annealed under the same conditions as T-40 but with extended durations of 80 and 100 min, respectively. As the annealing time is increased, the GFs grew larger and surface coverages of 63 and 85% were obtained in the samples T-80 (**Figure 3.7b**) and T-100 (**Figure 3.7c**), respectively.

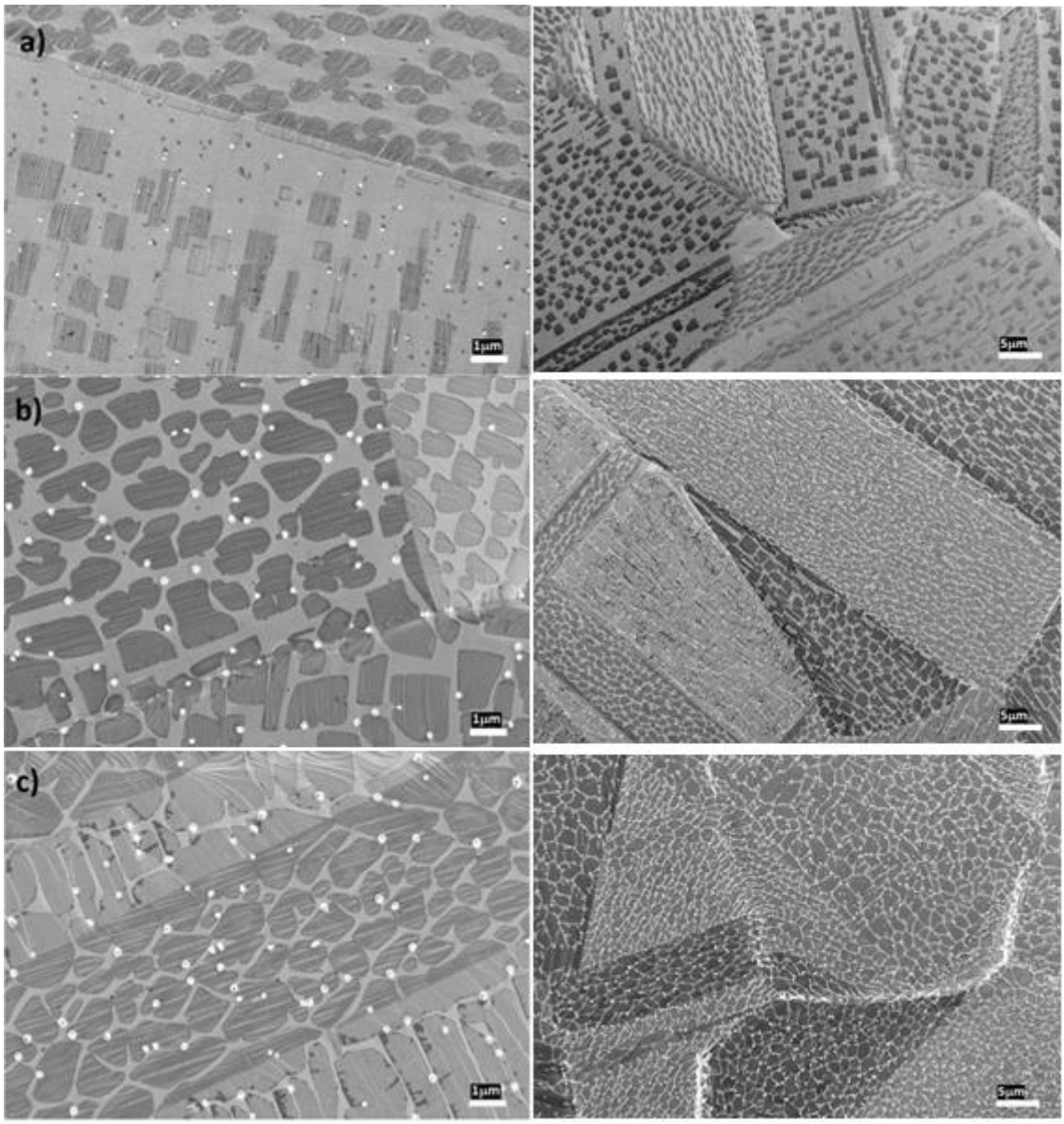

Figure 3.7: SEM images of copper foil annealed under 1.4 mbar hydrogen partial pressure for prolonged annealing duration 40 (T-40), 80 (T-80) and 100 min (T-100)

Reduced hydrogen concentration leads to the formation of GFs. (a) T-40, 40 min annealing time. Relatively small GFs; silicon oxide particles are mostly located outside or at the edge of the GFs. (b) T-80, 80 min and (c) T-100, 100 min annealing time. The size of GFs slightly increases with the annealing time but the surface is not fully covered. Even extending the annealing time beyond 100 min leads to no significant increase.

The Raman spectra taken from six randomly picked GFs on sample T-100 after they were transferred on to the SiO_2/Si substrate confirm the monolayer graphene structure in all flakes with slight variation in their quality (**Figure 3.8**) [62]. To our knowledge, the formation of neither a disordered graphitic film nor graphene flakes on copper during the annealing stage in the CVD system has been reported so far.

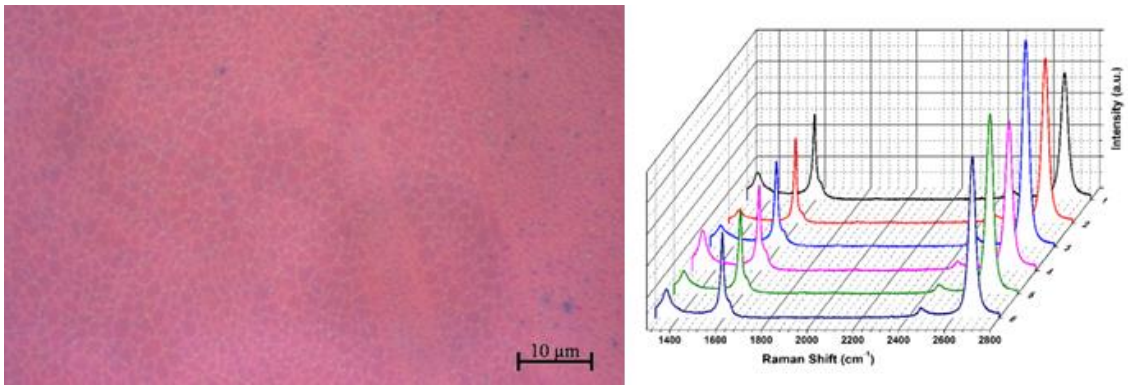

Figure 3.8: The optical image (left) and Raman spectrum of six random flakes of T-100 after transferring to SiO_2/Si substrate.

The ratio of 2D/G peaks, around 2700 and 1600 cm^{-1}, confirm they are monolayer graphene with slight variation in their quality (all normalized to the G peak).

No significant change in the surface coverage of GFs is observed when the annealing time was extended beyond 100 min. This can be explained as follows within the scope of the microscopic mechanism we proposed in **section 3.4**: our results verify that carbon originating from the copper foil facilitates graphene growth, but the growth is limited by the ability of the carbon in copper to reach the surface at the annealing temperature. The diffusion rate of carbon to the surface is expected to follow a continuously declining profile as the graphene flakes grow and block the access of hydrogen to the copper bulk, suppressing the release of carbon from C–O–Cu bonds. Therefore, as the annealing time is extended, the growth rate declines and coverage tends to saturate.

Depth profiles of carbon concentration in samples T-0, T-40, T-80, and T-100, measured with ToF-SIMS, are compared in **Figure 3.9** and its inset. As the annealing time is increased, the carbon content near the copper surface is increased while the carbon content in deeper parts is decreased. ToF-SIMS data directly and independently verifies the migration of carbon towards the surface. The inset figure shows the variation of carbon concentration versus annealing time for both near the surface (1.9-110 nm) and deeper in the bulk (110-300 nm). We observe a saturated behavior in carbon migration with respect to the annealing time, which is consistent with the saturation of graphene growth with the annealing time as explained in the previous paragraph.

In the SEM images shown in **Figure 3.7**, we can see some white particles scattered on the surface of Cu samples, and their size increases with longer annealing time. These particles are a compound of silicon and oxygen, originated from the quartz tube of the

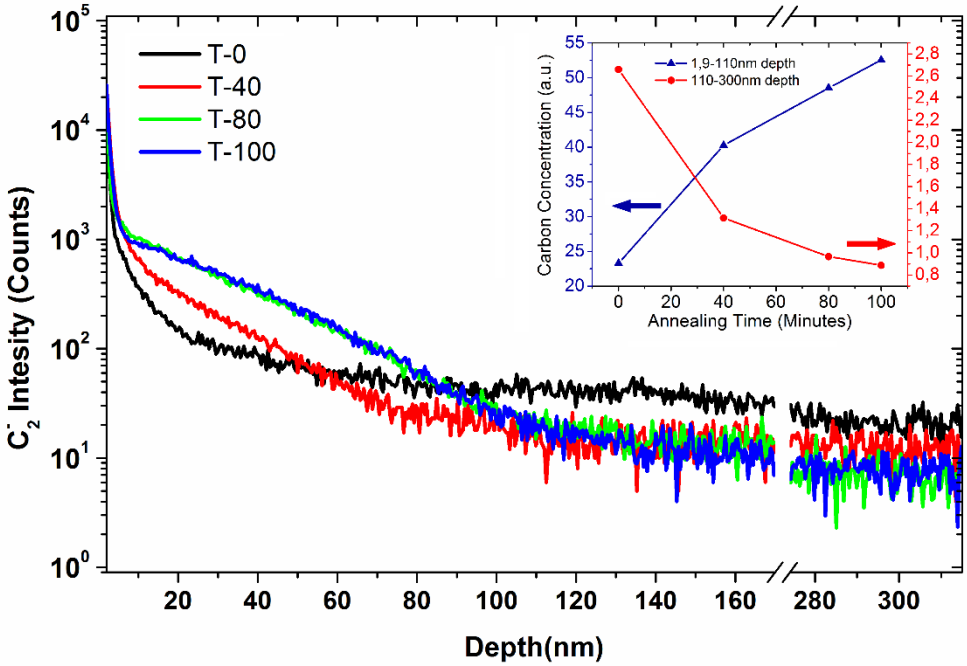

Figure 3.9: Depth profiles of carbon concentration in samples T-0, T-40, T-80, and T-100, measured with ToF-SIMS

Depth profile of C_2 intensity for untreated and 40, 80, 100 min treated copper foils (T-0, T-40, T-80, and T-100) under H_2. Comparing C_2 profiles in T-40 and T-80 with respect to T-0, we observe that carbon atoms deep in samples were depleted but the concentration in the region near the surface (0-55 nm for T-40 and 0-90nm for T-80) is increased. A similar C_2 profile of T-100 to T-80 indicates the slowing down of the H-assisted C depletion mechanism as graphene flakes grow and block the access of hydrogen to the copper bulk. Inset shows the variation of carbon concentration versus annealing time for both near the surface (1.9-110 nm) and deeper in the bulk (110-300 nm).

furnace (**section 5.1**) [17, 140-142]. It can be clearly seen that SiO_x particles are never sited at the center of GFs at the earlier stages of graphene growth. Therefore, we infer that silicon oxide particles are not the initial cause of graphene nucleation. But the accumulation and segregation of carbon atoms originating from the bulk of copper facilitate the nucleation.

The model we propose in this work based on our experimental results, provides a better understanding of why it is difficult to effectively suppress graphene nucleation without using a tuned oxygen flow or pocket geometry in the CVD process. A diluted oxygen flow before or during the growth phase suppresses nucleation by etching the “preformed” GFs, or carbon atoms on supersaturated spots. Hence, the number of spots which have enough agglomerated carbon for supersaturation to act as nucleation sites is reduced.

When a pocket geometry is used with the copper foil [143-145], diffusion rate of hydrogen into the pocket is reduced and the extraction rate of carbon from the bulk of the

copper foil to its internal surface is suppressed. This again effectively diminishes number of spots which can reach the supersaturation threshold.

3.5.1 SNGFs after chemically etching the surface of a copper foil

To confirm whether the origin of the observed GFs on T-40 is the carbon atoms distributed inside the bulk and not the surface contamination, we performed an experiment with a chemically cleaned Cu foils. We etched the surface of a copper foil with acetic acid/hydrogen peroxide solution to fully remove its outermost layer and the native oxide.[21, 60, 70]

In the first trial, we immersed the Untreated Cu foil inside the acetic acid for 10 minutes. However, we did not observe a significant change in the size and distribution of GFs after annealing them with the identical parameter of T-40. Accordingly, we checked the 10 min etched Cu foil under SEM, and we found that the Cu foil surfaces did not change much compared to Unetched Cu sample (comparing **Figure 3.10** to **Figure 3.2**).

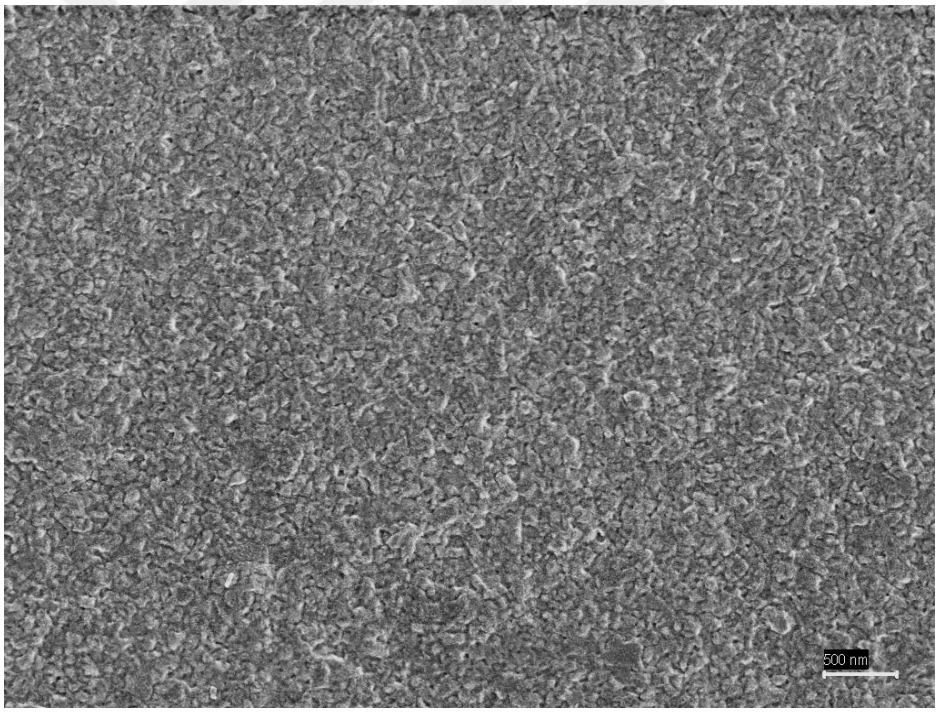

Figure 3.10: The SEM image of copper foil, which 10 min etched in acetic acid.

As it can be seen, exposing the copper surface to only acetic acid does not much affect the copper surface.

To intensify the surface etching, we added a few drops of hydrogen peroxide to the acid (1:30 ratio) and extended the etching time to 20 minutes. As it is demonstrated in **Figure 3.11**, the initial native oxide layer on the Cu foil were fully removed and their grains appeared. Accordingly, we used this recipe (20 minutes in 30:1 acetic acid and

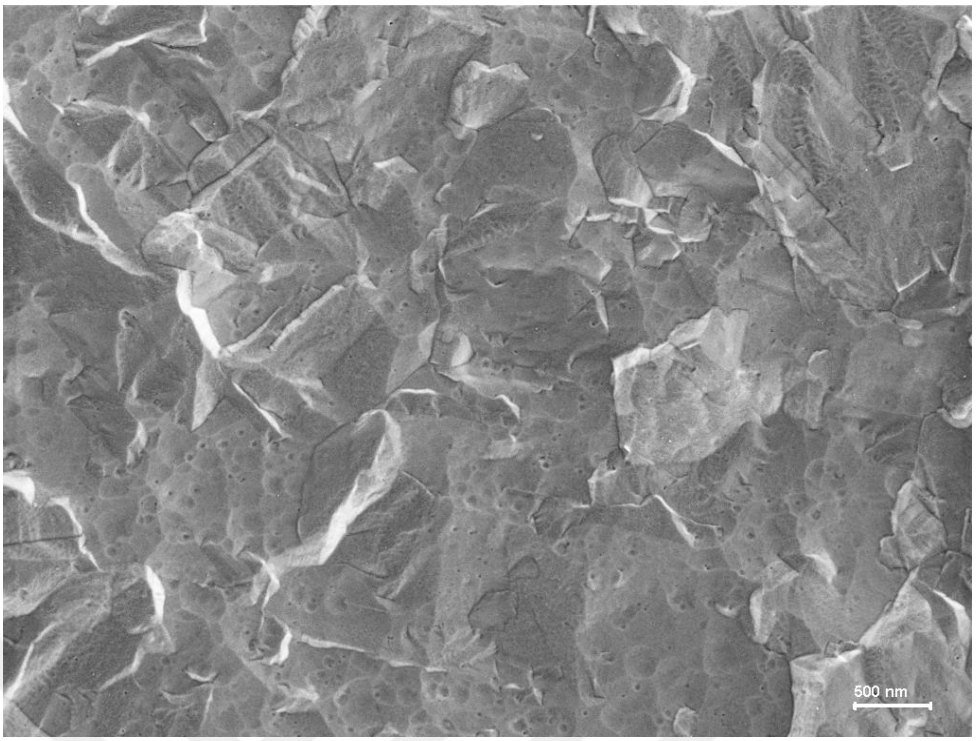

Figure 3.11: SEM image of copper foil, which 20 min etched in acetic acid and hydrogen peroxide mixture.

After 20 min the oxide layer on copper surface is etched and irregular grains of as-cast copper will appear.

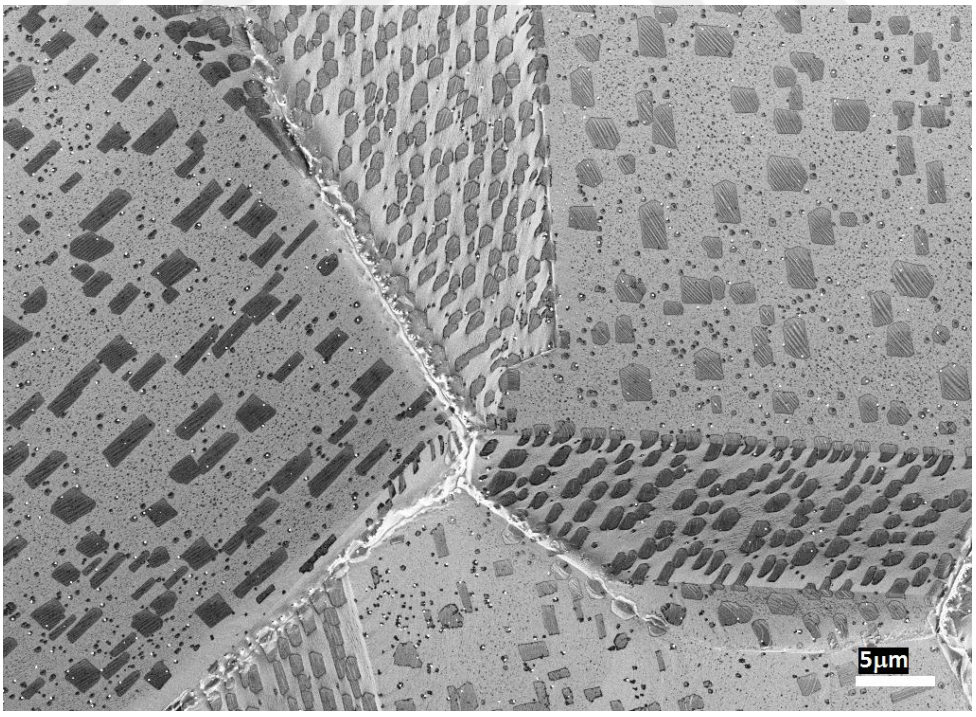

Figure 3.12: SEM image of T-40E

T-40E is 20 min etched Cu foil in acetic acid/hydrogen peroxide solution which is then annealed under 500 sccm argon and 50 sccm hydrogen for 40 min as sample T-40. Even after fully removing the outermost layer and any possible carbon contamination, we observe spontaneous growth of graphene on the surface.

hydrogen peroxide mixture) to prepare the etched sample for annealing test (T-40E). As it can be seen in **Figure 3.11** after 20 min the oxide layer on copper surface is etched and irregular grains of as-cast copper will appear.

Immediately after etching, the sample (T-40E) was annealed for 40 min in the furnace under 1.4 mbar hydrogen, similar to the process used for T-40 (Table 2). As demonstrated in the SEM image in **Figure 3.12**, GFs still appeared on T-40E after annealing. This provides additional evidence that carbon in the bulk of Cu foil contributes to the GF formation on the surface due to H-assisted depletion. We observed that the nucleation density of GFs was slightly reduced in the chemically etched sample as it can be seen by comparing **Figure 3.7a** and **Figure 3.12**. We attribute this reduction to the removal of high carbon concentration in copper layers just beneath the surface by chemical etching.

3.5.2 Experiments with high purity copper foil

Also, we used a different type of copper foil (99.999% purity) to investigate the variation of graphene nucleation with the level of purity. We repeated annealing and chemical cleaning conditions of T-40E on a sample labeled HP_T-40E taken from the high purity copper. Even though it had two orders of magnitude higher purity level,

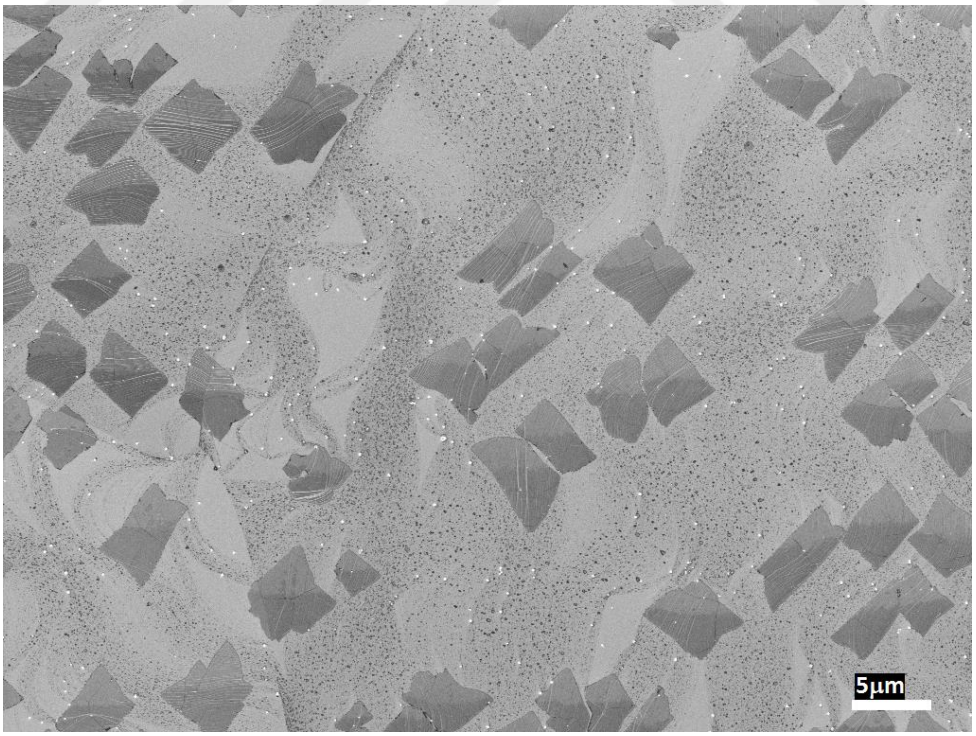

Figure 3.13: SEM image of HP_T-40E

HP_T-40E, the 99.999% pure copper 20 min etched in acetic acid/hydrogen peroxide and 40 min annealed under 500 sccm argon and 50 sccm hydrogen similar to T-40E. Compared to T-40E, the higher purity of HP_T-40E results in lower nucleation density and the coverage of GFs.

nucleation and growth of GFs are also observed in this sample confirming the presence of carbon in it (**Figure 3.13**). We believe that the rolling technique should again be the cause of the carbon content. We should note that the purity level reported by the supplier refers to metallic elements. Thus, to achieve a reproducible nucleation and growth conditions, the distribution profile of carbon inside copper foil needs to be considered.

From the distribution of GFs in **Figure 3.7**, **Figure 3.12** and **Figure 3.13** we can conclude that carbon does not seem to be preferentially segregated along the copper grain boundarie*s*. However, we avoid making a definite conclusion because the boundaries move during the annealing (e.g. Ref [22]). Thus, even when carbon preferentially segregated along the copper grain boundaries, after it reaches to the surface it may not move and follow the direction of boundary movement during annealing. Therefore, we may not observe a correlation between grain boundaries and segregated carbon.

Also, in **Figure 3.7a**, **Figure 3.12** and **Figure 3.13** there are some nm size dark spots visible beside micron size GFs. We believe that these features are graphitic or amorphous carbon clusters that emerged on the surface during the cooling phase as the solubility of carbon in copper drops with decreasing temperature.[138] On the contrary, this kind of dark spots do not appear in the SEM images of **Figure 3.7b, c**. This is due to extended exposure to hydrogen annealing, after which there was not enough carbon to emerge to the surface and form such carbon clusters during the cooling phase.

3.6 Conclusions

In this chapter, we have demonstrated the aggregation of carbon atoms on the surface of copper foil after annealing under hydrogen in the absence of external carbon sources. Depending on hydrogen partial pressure, carbon atoms may form either a disordered graphitic film or graphene on the surface. Despite the fact that the solubility of carbon atoms inside pure copper is very low, our experimental results verify that the growth of these carbon-based structures is due to the presence of intrinsic carbon in the copper bulk. We proposed that the migration of carbon atoms from inside the copper towards its surface is induced by hydrogen. This depletion mechanism is independently verified by measuring C2 intensity versus depth by ToF-SIMS. The depth profiles of processed and untreated samples demonstrated the migration of carbon during the annealing process under hydrogen. We conclude that the nucleation and growth of graphene on copper foil in CVD cannot be considered as a pure “surface process”, due to the presence of carbon

embedded below the surface during the foil production process. Therefore, the "competition between the surface mobility of carbon ad-atoms versus desorption" of an external precursor does not define the full characteristics of the nucleation regime of graphene crystals on copper in the CVD process. One needs to include the out-diffusion of carbon atoms originated from the inside of copper bulk as well.

The carbon atoms migrating from the copper bulk to the surface can be the main cause for the nucleation of graphene crystals rather than the surface imperfections and impurities such as SiO_x particles. We believe that the prematurely nucleated and grown GFs during the annealing phase under hydrogen become a determinant factor for the density of growing GFs during the growth phase. Thus, to achieve a reproducible growth condition, the distribution profile of carbon inside the copper foil needs to be considered. Accordingly, the approach for annealing copper foil presented in this paper can be considered as a method for an initial evaluation of embedded carbon inside a copper foil and its effect for reproducing a growth recipe.

4 Pressure dependence of hydrogen-assisted carbon depletion

4.1 Introduction

In this chapter, we verified the hydrogen assisted depletion of carbon in Cu foil under a wide pressure range of H_2. Supported by ToF-SIMS depth-profile measurements of carbon in Cu foil together with optical microscopy and SEM characterizations of the annealed surfaces, we revealed simultaneous accumulation and etching of a carbon film on the Cu surface. We show that depending on the H_2 concentration, annealing process can result either formation of DG or graphene at varying qualities, or a completely carbon free surface, although for all cases the migration of carbon to the surface is evident. Finally, we practiced annealing of copper under maximized hydrogen pressure for the purpose of reducing the carbon content in its bulk and consequently achieved a reduction in the density of SNGFs. To obtain compatible data with chapter 3, we used the same setup and materials in the experiments presented here.

The experimental result presented in this chapter on the HACD mechanism elucidates further details about the role of hydrogen in the CVD process for growth of graphene on Cu foil and can explain part of the inconsistencies among some the earlier reports [4, 30-33, 35, 36].

4.2 Etching of carbon under high concentration of hydrogen

To investigate the effect of H_2 partial pressure on depletion of intrinsic carbon during the annealing, Cu foil samples (99.8% metallic pure) were annealed under the H_2:Ar atmosphere with varying pressures and concentrations of H_2. The details of the annealing parameters are given in **Table 3**. In **Figure 4.1**, the SEM images of these samples after

annealing are demonstrated for comparison. Due to boosting of HACD at high H_2 pressure, compared to P-6, a thicker DG film was expected for P-17 and P-60. However, in the SEM images we can see that when the concentration of H_2 was increased in the case of sample P-17, the DG film to got partially etched (**Figure 4.1b**), and with maximum hydrogen partial pressure for P-60 the DG film was completely vanished and a clean surface was obtained (Figure 4.1**Figure 4.1c**). Surface coverage on P-17 and P-60 were also tested by ambient oxidation (two minutes heated at 180°C) and confirmed the etching of the DG after rising hydrogen pressure (**Figure 4.2**).

Table 3: Annealing process parameters for samples P-6, P-17, and P-60.

After annealing without using any external carbon precursor, a disordered graphitic (DG) film is formed on the surface of Cu foils. The DG film coverage is determined by scanning electron microscopy and also verified by ambient oxidation. Under 6 mbar H_2 partial pressure. However, increasing the H_2 pressure resulted in an etched graphitic layer on copper surface.

Sample	Annealing time (minutes)	H_2:Ar flow rate (sccm)	Process pressure (mbar)	H_2 pressure (mbar)	Figure	DG film coverage
P-6	20	200:500	20	6	Figure 4.1, Figure 4.2	Full coverage
P-17	20	200:500	60	17	Figure 4.1, Figure 4.2	Partially etched
P-60	20	200:0	60	60	Figure 4.1, Figure 4.2	Fully etched

To get a better insight about this paradoxical effect of HACD, the depth profile of carbon in samples treated for the same duration under varying H_2 pressures P-17 and P-60 or left untreated were measured by ToF-SIMS technique. ToF-SIMS results presented in **Figure** 4.3**4.3** establish that rising of the hydrogen pressure enhances the depletion of the carbon content from bulk of Cu foil as expected in HACD mechanism. However, in contrary to the results of annealing at 6 mbar H_2, or below [37], the surface concentration of carbon is decreased after annealing at 17 mbar or above H_2 pressure. As can be seen in **Figure 4.3** the crbon intesity profile of P-6 crossing the profile of untreted sample (T-0) around 10 nm depth. This is becaused the depleted carbon from down below 10 nm depth of P-6 acumulated close to its surfce (above 10 nm). This crossing of the depth profile dose not happenng nither for P-17 nor for P-60, but the overall down-shifting of their profiles indicates enhanced HACD vrsus the H_2 pressure. As further details are discussed in the following paragraphs, we argue that increasing the H_2 pressure and therefore boosting HACD, induces more defects and deteriorates the atomic bonds of grown

graphitic film on copper from the depleted carbon atoms. Accordingly, the carbon-based structure cannot withstand on the surface at the elevated annealing temperature. This is effect explain the deference between the surfaces of P-6, P-17 and P-60 that we observe in **Figure 4.1** and **Figure 4.2**.

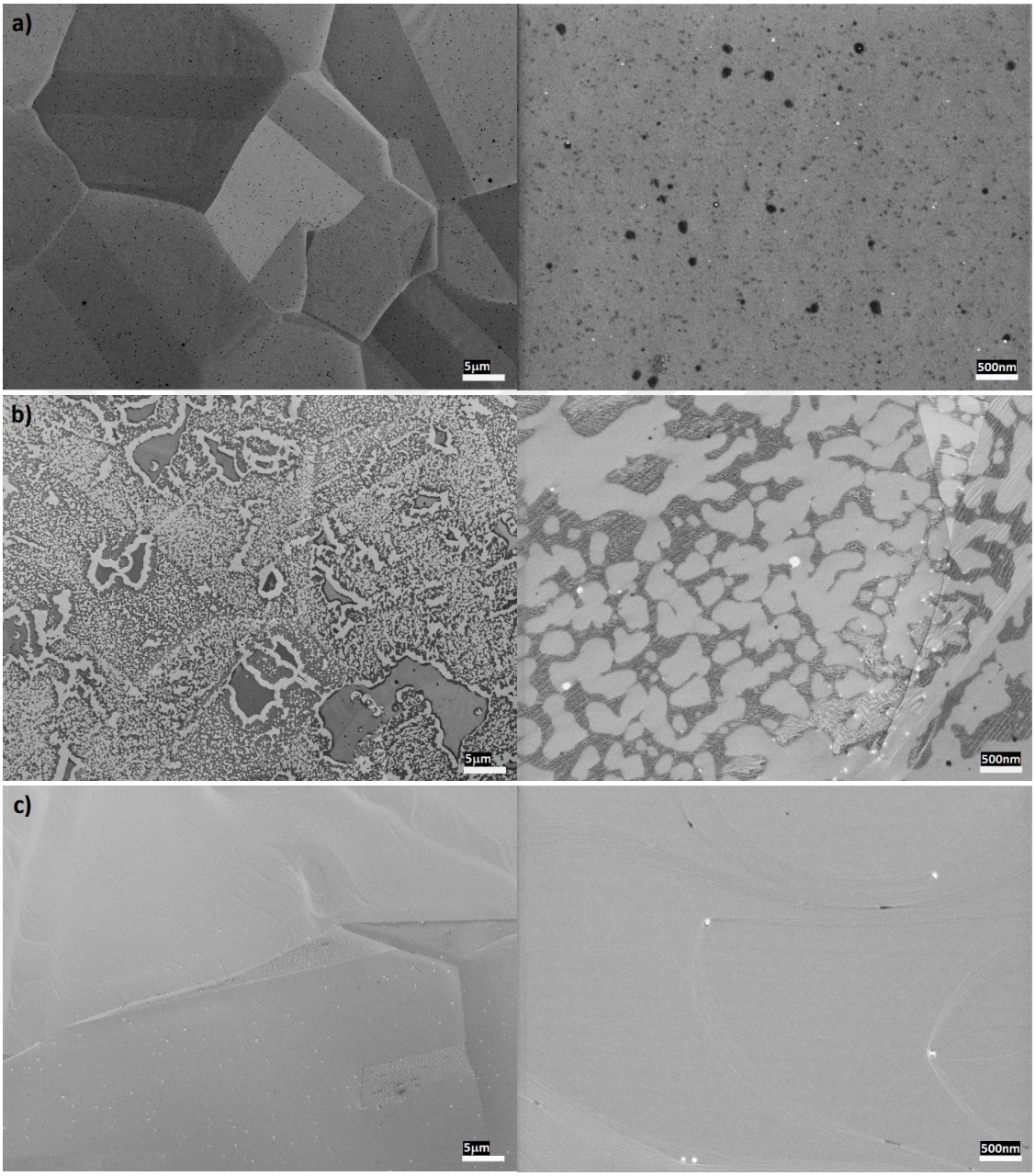

Figure 4.1: SEM image of P-6, P-17 and P-60 in different magnification

Refer to Table 1 for process parameters for each sample. a) P-6, a graphitic layer covered the whole Cu surface.b) P-17, DG partially covering the Cu surface since it got etched at high hydrogen concentration. The darker regions are the unetched parts of the graphitic layer. c) P-60, no graphitic layer is present since it was completely etched away during the annealing.

In general, etch and growth rates depend on several parameters including the purity of feeding gases [4, 33, 35, 36, 137, 140]. Depending on the relative rate of these

counteracting mechanisms, either the growth or the etching of graphitic film on the copper surface dominate at different stages of the thermal treatment [146].

Here we offer and discuss three possible mechanisms that can cause the etching of the graphitic layer when hydrogen is introduced during annealing:

i) Etching by the oxidative impurities in the hydrogen gas: Role of oxygen and/or oxidative impurities in H_2 gas on etching of graphene, even at ppm level concentrations, were demonstrated in the literature. [4, 35, 36] Since the pressure of H_2 also determines the partial pressures of its oxidative impurities a etch rate should depend on it. We used 99.999% pure gases with constant flow rate in each of our experiments. Besides, since the carbon content in copper foil is finite, the rate of out-diffusion of carbon declines in time during the annealing and at a certain point the etch rate exceeds the growth rate.

ii) Enhanced etch rate of DG films due to inherent defects: Here we can consider two extreme conditions. On one side, applying very low hydrogen pressure reduces SNGFs due to reduction of HACD mechanism and hence the reduced number of supersaturated spots on the surface. In this scenario, due to the minimized SNGFs, larger size graphene flakes with less edge atoms and less defects per area will grow on the surface. On the other side, applying high hydrogen pressure, causes a very fast carbon depletion and generates supersaturation at numerous points on the surface of copper foil. However, the high density of supersaturated sites on the surface will result in a DG film with very small size graphitic domains and more defects and edges.[114] The more defected graphitic film is more prone to chemical etching. Therefore, while the rate of out-diffusing carbon declines during annealing, the etch rate exceeds the growth rate and dominate during early the stages. As a result, the more defected DG film is etched faster; this is consistent with the observations of partially etched P-17 and fully etched P-60.

iii) Etching assisted-/cause by hydrogen; Although, it has been discussed that unintentional oxidative impurities causes the etching effect on graphene in hydrogen atmosphere [4, 35, 36], however, science in HACD effect we are dealing with different mechanism for SNGFs or growing DG film, the possibility of etching by hydrogen may is needed to be taking into account. The

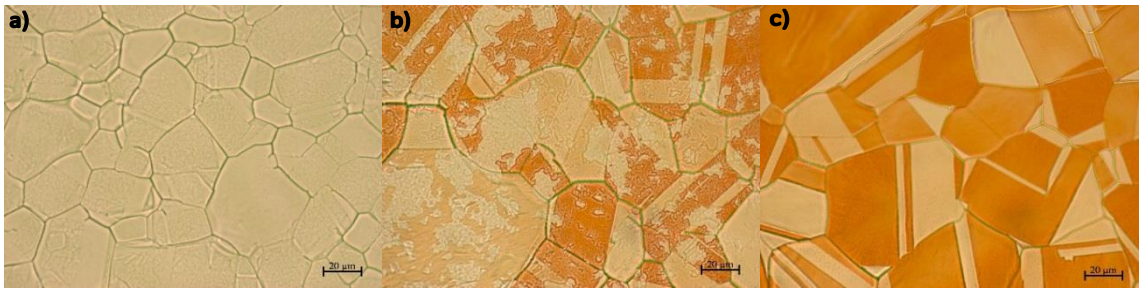

Figure 4.2: The optical image of P-6, P-17, and P-60 after 2 minute heat treatment at 180 °C in air

a) The surface of P-6 was not oxidized at all after 2-minute heat treatment at 180 °C in air since it is fully covered by a thin layer of a graphitic film. b) The partially etched graphitic layer on the surface of P-17 protects the copper surface from oxidization on coated regions. c) The whole of P-60 surface is oxidized since there was not any graphitic film on its surface as a barrier against ambient air during heating at 180 °C. The variation of the oxide color is due to different oxidation rates of copper grains with varying crystal orientations.

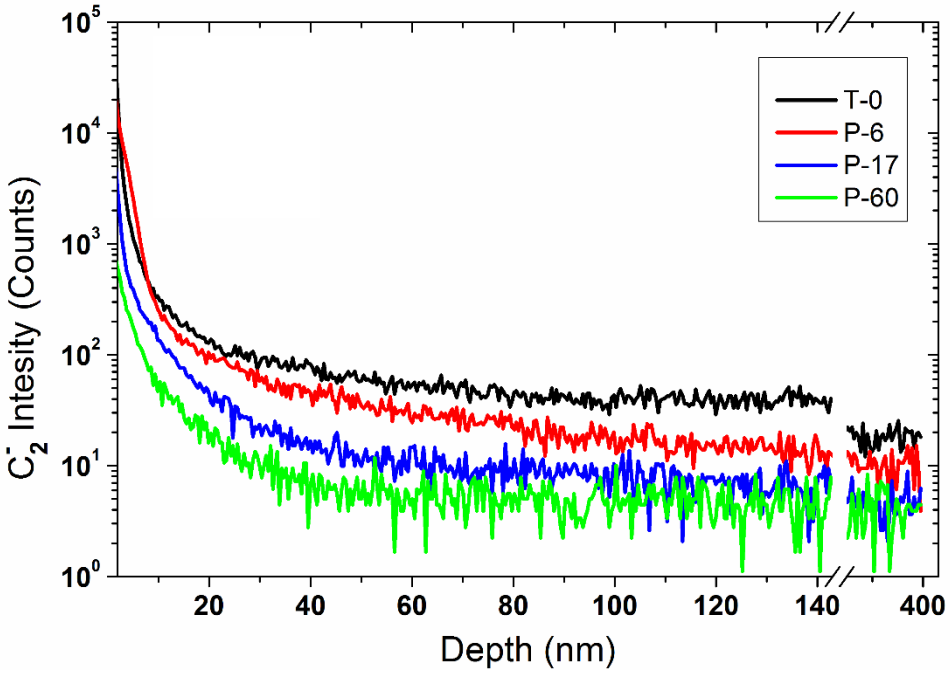

Figure 4.3: Depth profile of C_2 intensity measured by ToF-SIMS in copper foils treated in different level of hydrogen pressure (T-0, P-6, P-17 and P-60)

The comparison of untreated sample (T-0) and the samples treated in 6 mbar (P-6), 17 mbar (P-17) and 60 mbar (P-60) clearly demonstrates enhancement of carbon depletion below the surface of Cu foil with increase of the hydrogen pressure.

higher level of H_2 concentration provides the higher chance for reaction of C radicals with H^+ ions over the surface of copper and formation of C-H bonds instead of the C-C bonds. Therefore, the more implement H-C defect bond in the C-C network of graphitic film, means more fragile sites against etching by oxidative gas impurities. Accordingly, high concentration H_2 and thus H^+ can

induces more defected sites in graphitic atomic chain grown on P-17 and speeds of etching mechanism described in (i) and (ii).

In an extreme level of hydrogen concentration, the H^+ ions may totally passivating the out-diffusing carbon radicals, right after reaching to the surface. This may ends up with formation volatile C_xH_y molecules that evaporate and leave the surface at 1000 °C. Accordingly, during annealing of P-60, the depleted carbon may even did not form any graphitic film and simply get etched as soon as reaching to copper surface.

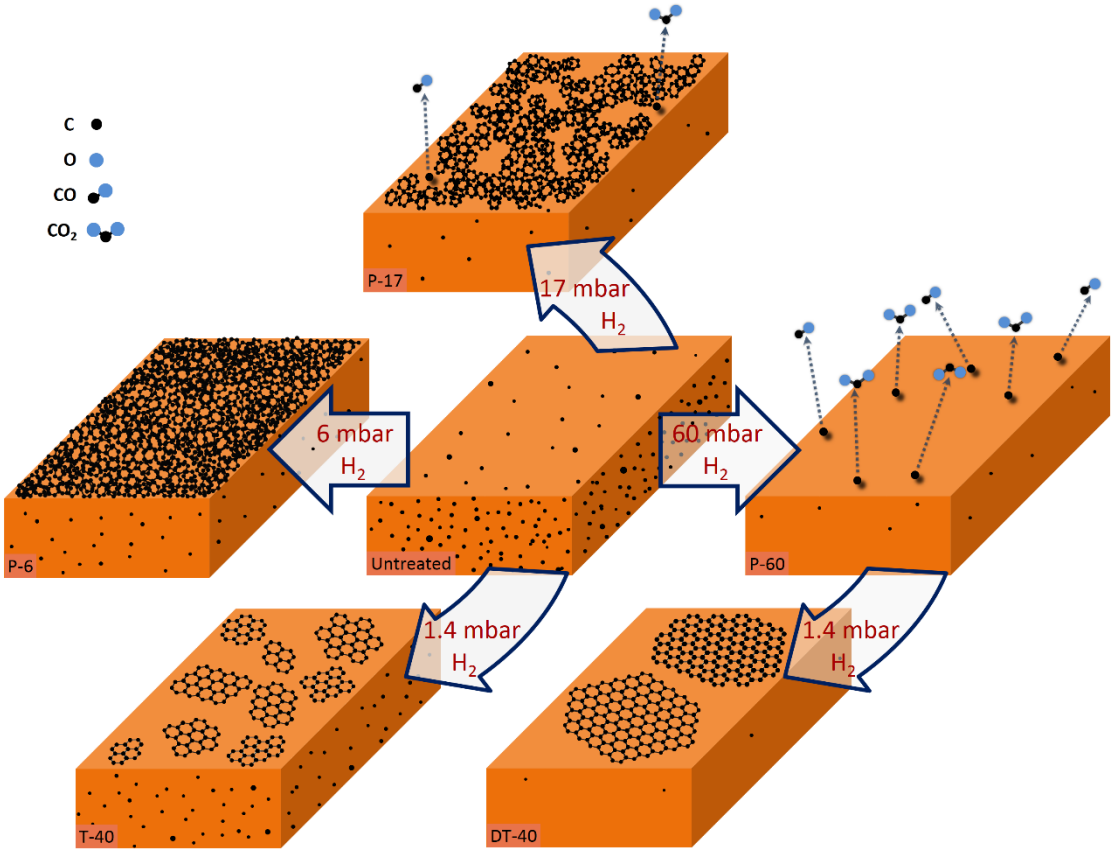

Figure 4.4: Schematic illustration of effect of HACD in different conditions.

The annealing of copper in 1.4 mbar H_2, slowly depletes the carbon atoms from its bulk, therefore some spot on the copper surface could pass supersaturation threshold that leads to nucleation and growth of GFs (T-40). Raising H_2 pressure to 6 mbar during annealing increases the rate of C depletion and supersaturates the whole surface immediately. As a result, a graphitic film without a long-range atomic order (DG film) grows on P-6. [37] Further increase of H_2 pressure causes futher disorder on the graphitic structure of grown film from depletes carbon due to faster HACD mechanism at higher H_2 pressure. This results in such a weak graphitic film that can not survive to the end of annealing proccess and gets partially (P-17) or fully (P-60) etched depending the H_2 pressure. Since SNGF is attributed to the carbon content inside the copper, SNGF is expected diminish on a Cu foil which has less carbon in its bulk than the untreated Cu foil. Therefore when P-60 is treated again at 1.4 mbar of H_2, SNGF is observed but at a reduced density.

To identify the weight of each of these three possible effects on the removing carbon based features from the copper surface, we believe more experiments are needed. For e.g. by replicating the P-60 and DT-40 test with ultra-pure hydrogen (grade of 6 or 7 for purity) we may be able to conclude on the role of hydrogen for etching/cleaning on Cu foil in the CVD process.

A schematic diagram illustrated in **Figure 4.4**, describes the overall effect of H-assisted C depletion mechanism from bulk the surface of copper foil under various hydrogen concentrations.

4.3 Suppression of graphene nucleation after an effective HACD

In the next part of our experiment, as illustrated in **Figure 4.4**, we used highest hydrogen pressure (60 mbar) to utilize HACD mechanism to effectively deplete the carbon inside the bulk of Cu foil. Since SNGF is attributed to the carbon content of Cu foil, a diminished version of this effect during another round of annealing under low pressure of H_2 (1.4 mbar) was expected. To do so and as described in **Table 4**, sample labelled DT-40 first was applied 200 sccm hydrogen at 60 mbar for 40 minutes to deplete its carbon at an excessive rate, then was continued to be annealed for another 40 minutes at a reduced hydrogen concentration (1.4 mbar) in favor of SNGF from the remaining carbon in the Cu foil. Basically, the same recipe as T-40 is applied on a sample which was pre-processed to deplete its carbon content.

Table 4: Annealing parameters and the calculated density for the samples T-40 and T-40D.

Sample DT-40 was initially treated before they were applied the same annealing process as T-40. The initial treatment for DT-40 was the depletion of the carbon in the bulk by the application of the same procedure as P-60. Nucleation density is dramatically reduced in this sample.

Sample	Initial annealing (40 minutes)			Second annealing (40 minutes)			Graphene nucleation density (mm^{-2})
	H2:Ar flow rate (sccm)	Process pressure (mbar)	H2 pressure (mbar)	H2:Ar flow rate (sccm)	Process pressure (mbar)	H2 pressure (mbar)	
T-40	-	-	-	50:500	16	1.4	$6x10^5$
DT_40	200: 0	60	60	50:500	16	1.4	$3.3x10^4$

SEM images of sample DT-40 is illustrated and compared to SEM images of T-40 in **Figure** 4.5 **4.5**. From this image we can conclude that the carbon depletion in the first phase of annealing of DT-40 resulted in more than one order of magnitude reduction in

the density of SNGFs compared to T-40. This result is consistent with earlier reports. However, in those reports hydrogen 'surface' cleaning was proposed as the mechanism for the observed reduction in the nucleation density.[147, 148]

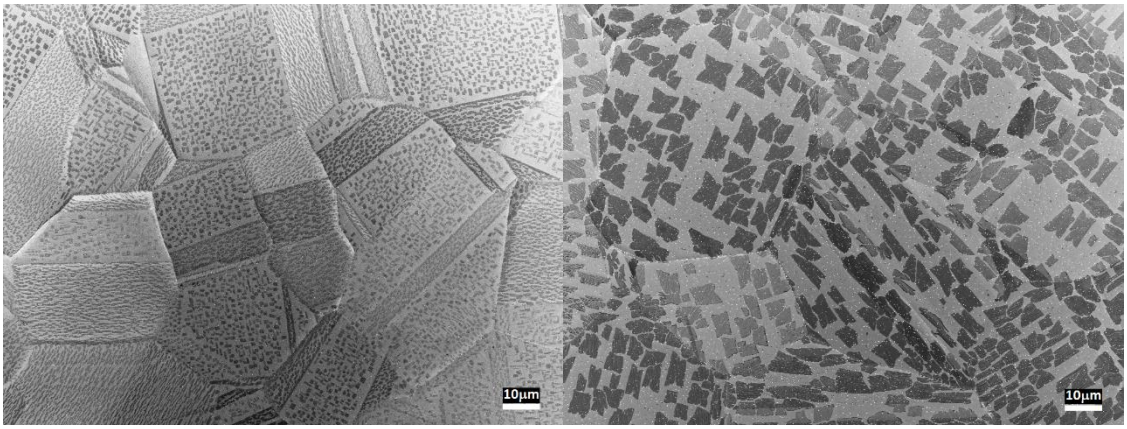

Figure 4.5: SEM image of T-40 (left) and DT-40 (right)

In DT-40 which was treated in two annealing steps, the effective carbon depletion due to the high concentration of hydrogen during the first step of annealing decreases the density SPNGFs in the second step of annealing.

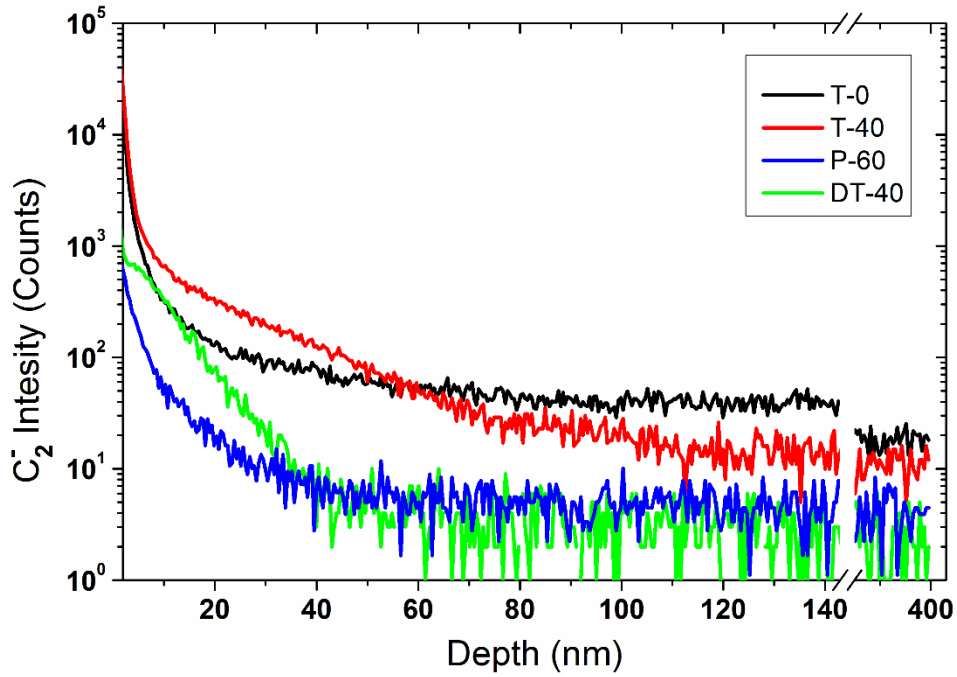

Figure 4.6: Depth profile of C_2 intensity for untreated (T-0), medium treated (T-40) and maximum treated of (P-60 and DT-40) copper foils under H_2

Similar change from T-0 to T-40 can be observed for changing in profile of P-60 to DT-40. That is crossing carbon profile of P-60 and DT-40 (at 40 nm), implying the migration and accumulation of carbon towards the copper surface in the second annealing step at 1.4 mbar H_2 pressure for DT-40. The one order of magnitude less carbon at the surface of DT-40 than of T-40 explains the one order of magnitude less in the nucleation density of DT-40 in comparison with nucleation density in T-40.

Again, we used ToF-SIMS to measure carbon depth profile in DT-40 and to explain the reduction in the density of SNGFs in of DT-40. The carbon depth profile in P-60 and DT-40 can be compare with of T-0 and T-40 as given in Figure 4.6. As can be seen in **Figure 4.6**, a similar trend in changing of carbon profile from T-0 to T-40 also is visible for changing from P-60 to DT-40. That is crossing carbon profile of P-60 and DT-40 (at 40 nm) similar to crossing of T-0 and T-40 profile (at 50 nm). This, implies the migration and accumulation of carbon toward the copper surface in second annealing step at 1.4 mbar H_2 pressure for DT-40. However, as the overall carbon densities in P-60 and DT-40 are declined, there is one order of magnitude less carbon at the surface of DT-40 than of T-40 surface. This explains the why the nucleation density of GFs in DT-40 is one order of magnitude lass than of T-40, as given in **Table 4** and displayed **Figure 4.6**.

4.4 Conclusions

In the experimental result of this chapter, we illustrate an opposite aspect of HACD on Cu foil that appears during the annealing Cu foil under increased concentration of hydrogen (compared to SNGFs described in **chapter 3**), which can reduces the surface density of carbon on Cu foil.

We demonstrated that increasing hydrogen pressure is boosting HACD mechanism. The boosted HACD provide a faster supersaturation of whole copper surface which results in a defected disordered graphitic film on the surface.

Our experimental results verify that, at elevated H_2 pressure, DG film become such fragile that get etched before ending the annealing phase. We discussed that the higher H_2 pressure causes the more defect in the grown graphitic structure on the Cu foil. As a result, presence of oxidative impurities in the flowing gas can be more effective on etching of the more defected DG film.

Furthermore, we used the boosted HACD at maximized H_2 pressure of the system as a pre-treatment approach to effectively reduce total carbon content of Cu foil and minimize SNGFs effect in another step of annealing at 1.4 mbar H_2. The observed one order of magnitude decrease in density of SNGFs of such a pre-treated sample, elucidate hydrogen surface cleaning.

5 Further discussion and technical details

In this chapter, further valuable experimental results that have been achieved along the main scope of this thesis are presented. Also at the last part of the thesis, the practical challenges against quantitative evaluation of HACD process are discussed.

5.1 SiO_2/SiO_x contamination

From EDS analysis, that is given in **Figure 5.1** in different scales; we found that these white nanoparticles that appeared at the surface of the Cu foil are silicon oxide (**Figure 5.1**)[17]. Later Lisi et al. reported that the SiO_x particles originating from quartz tube as a result of aging, and claimed that such contamination could not be found on graphene when installing a new tube [142]. Although our experimental result also confirms the connection between quartz tube age and level of SiO_x contamination, we noticed that the aging of the tube is not the single main parameter that involves the SiO_x particles contamination.

In our experiments, we found that the annealing duration is also a very effective parameter for the size of SiO_x particle on the Cu surface. In experiments with our growth setup, we observe less SiO_x particle contamination using an aged tube after a short time-high temperature treatment and more SiO_x particles using a new quartz tube after a more extended thermal treatment. For example, as it can be seen in **Figure 3.7** larger size particles appeared in T-100 compared to T-40. We repeated each experiment more than once in varying orders in time but did not observe any difference in terms of the size and density of the SiO_x particles or GFs. To be more specific, the reported result for T-40E and HP_T-40E given in **Figure 3.12** and **Figure 3.13** belong to the experiment that has

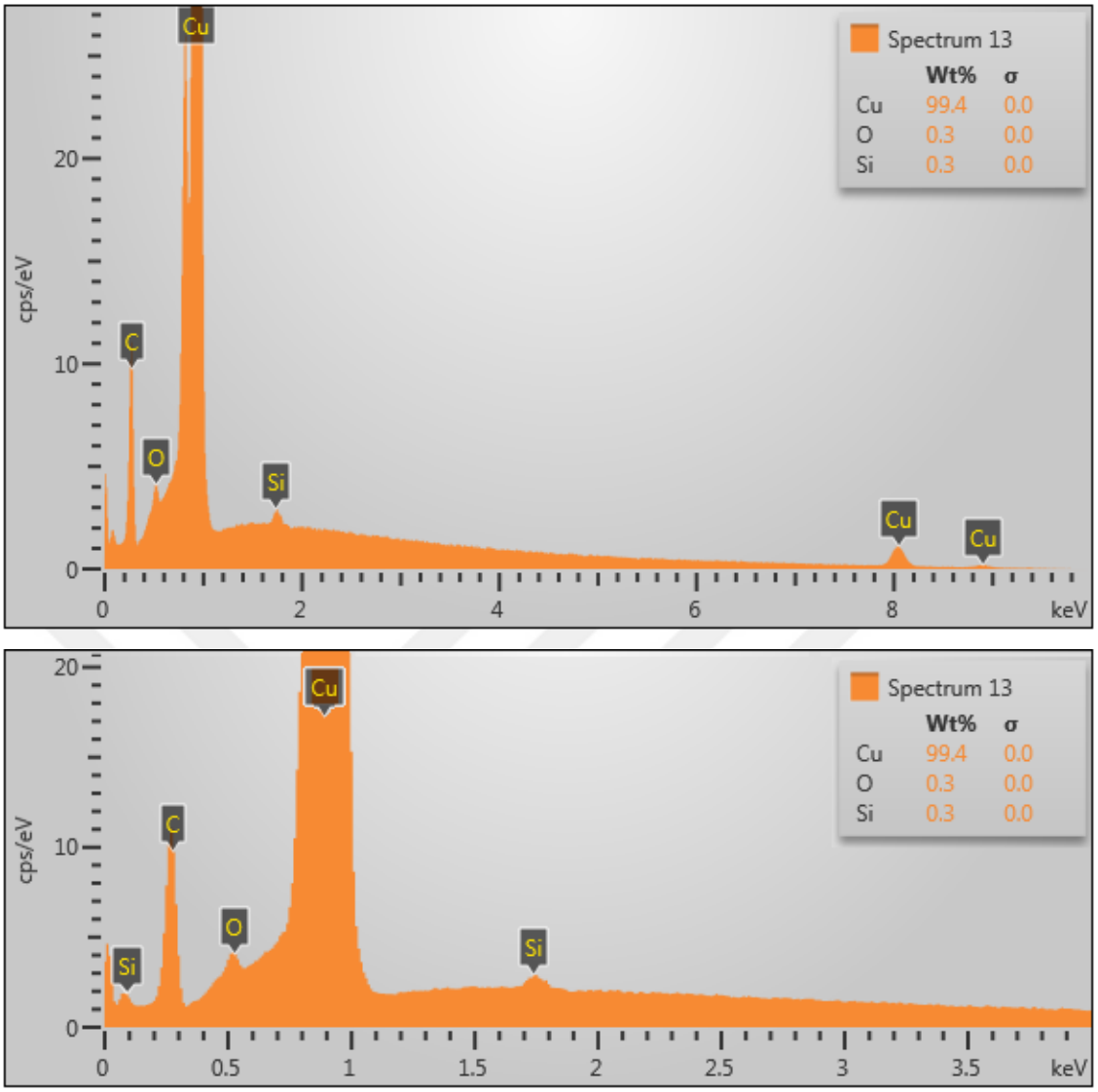

Figure 5.1: Typical EDS analysis of white particle in the SEM images reveals they are SiO_x

The EDS analysis in different energy and count scale confirms silicon and oxygen are the only origins of the white particle contaminations.

been done after T-100. But the size of SiO_x particle on T-40E and HP_T-40E are as small as on T-40.

Furthermore and more importantly, we found in our experiments that the affinity between SiO_x and copper surface differs depending on conditions which seem being missed in *Lisi et al.* report. For example, the SiO_x particles prefer to be deposited at the edge of GFs or stay on the uncovered part of Cu foil rather than the surface area which is covered by graphene or graphitic film. This effect, which clearly can be seen in **Figure 3.7**, is due to the different surface energy of Cu foil in case of being covered with graphene. Additionally, in section **5.2** we extend our experimental tests by using methane

as the external precursor for growth of graphene which provides fast and continues graphene growth on the copper surface. As the SEM images of T-40_G1.4 is given in **Figure 5.3**, we observed negligible SiO_x. This is because in case of a short annealing duration and implementing external carbon precursor the fast growth and full coverage graphene diminish desorption of SiO_x vapor on the copper surface.

5.2 The effect of HACD on nucleation of graphene ad-layers

Although the core of our research in this thesis was not about the growth of multilayer graphene on Cu foil, we observed interesting results as briefly investigated the effect intrinsic carbon and HACD in formation ad-layer graphene on the surface of a Cu foil. As we demonstrated and discussed our experimental results in the following lines, the density of ad-layer can be effectively modified by changing intrinsic carbon in the copper, using HACD.

As the last part of our experimental study, we extended our experiment to the CVD growth of graphene on copper, investigating the effect of the intrinsic carbon in the copper bulk on graphene thickness nonuniformity and the formation of graphene ad-layers. As given in **Table** 5 and with a similar approach to subsection 4.3, we used two Cu foil samples (99.8% metallic pure) that were treated under different annealing parameters but the same growth parameters as described in **Table** 5. The first sample is labeled as T-40_G1.4, and it was annealed (as same as sample T-40) under 1.4 mbar hydrogen for 40 minutes followed by 20 minutes growth by adding 18 sccm methane to the flowing gases. The second sample is labeled as P-60_G1.4, and it was annealed (as same as sample P-60) under 60 mbar hydrogen for 40 minutes and followed with the same growth parameters of T-40_G1.4. As can be seen in SEM images of both T-40_G1.4 and P-60_G1.4 in **Figure** 5.2, they were fully covered with a single layer of graphene. However, more effective depletion and decreased carbon in P-60_G1.4, during annealing at the higher concentration of hydrogen provides three times reduction in density of graphene ad-layers compared to that of T-40_G1.4. We should note that we observe this reduction in density of graphene ad-layers in the P-60_G1.4 while the density and size of SiO_x particles on P-60_G1.4 are more than of T-40_G1.4. Accordingly, despite the earlier thought, [17, 60, 62] that the surface impurities and roughness to be the primary cause of graphene ad-layer formation, the result of this section refers to the intrinsic carbon inside the copper as the primary source of growing ad-layer graphene on the copper.

Table 5: Annealing and growth parameters for samples T-40_G1.4 and A60_G1.4.

Different hydrogen pressure was used for annealing of T-10_G1.4, T-40_G1.4 and P-60_G1.4 to study the effect of H-assisted C depletion on the density of graphene ad-layer.

sample	annealing (10 minutes)			growth (30 minutes)			figure	graphene ad-layer density (mm^{-2})
	H_2:Ar flow rate (sccm)	Process pressure (mbar)	H_2 pressure (mbar)	H_2:Ar:CH_4 flow rate (sccm)	Process pressure (mbar)	H_2 pressure (mbar)		
T-10_G1.4	50:500	16	1.4	50:500:18	16	1.4	Figure 5.3	$\approx 2x10^6$
	annealing (40 minutes)							
T-40_G1.4	50:500	16	1.4				Figure 5.2	$\approx 7x10^5$
P-60_G1.4	50: 0	60	60					$\approx 2x10^5$

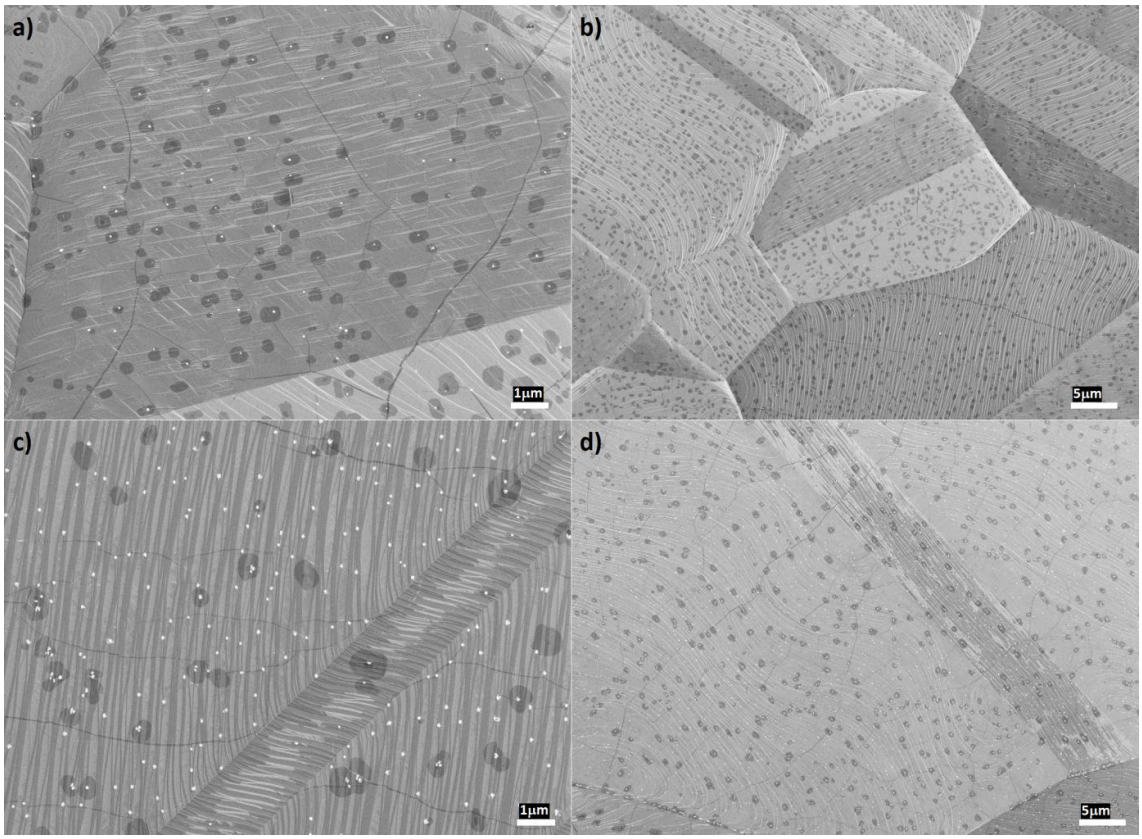

Figure 5.2: SEM images of graphene grown on T-40_G1.4 and P-60_G1.4which have been treated under different H_2 pressure during annealing stage but same H_2 pressure during the growth stage.

T-40_G1.4 (a and b) annealed under 1.4 mbar hydrogen for 40 minutes followed by growth for 20 minutes by adding 18 sccm methane to the flowing gases without changing the argon and hydrogen flow rate. P-60_G1.4 (c and d) annealed under 60 mbar hydrogen for 40 minutes and then followed by growth with the same parameter of T-40_G1.4. Both T-40_G1.4 and P-60_G1.4 are fully covered with the single layer of graphene, but due to the higher concentration of carbon in T-40_G1.4 the density of graphene ad-layers in T-40_G1.4 are higher than P-60_G1.4.

Finally, we tested the effect of annealing duration on the formation of graphene ad-layers regarding our expectation from the time-dependency of HACD. We repeated the

same parameter of T-40_G1.4 recipe, except for annealing duration that has been shortened to 10 minutes, and therefore we labeled it as T-10_G1.4 in **Table 5**. Hence, in T-10_G1.4 more intrinsic carbon survived from HACD and remained in its bulk compared to

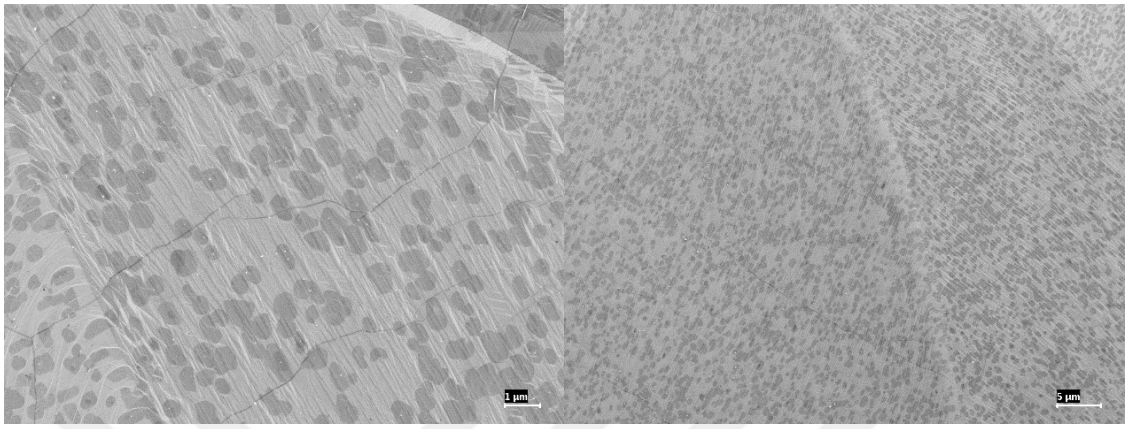

Figure 5.3: SEM images of graphene grown on T-10_G1.4 which has been treated under the same H_2 pressure during the annealing and the growth to of T-40_G1.4 but with a shorter annealing duration.

T-10_G1.4 annealed under 1.4 mbar hydrogen for 40 minutes followed by growth for 20 minutes by adding 18 sccm methane to the flowing gases without changing the argon and hydrogen flow rate. Similar to T-40_G1.4, T-10_G1.4 is entirely covered with the single layer of graphene, but the more surviving intrinsic carbon from HACD due to the reduced annealed duration a higher density of graphene ad-layers can be observed on its surface.

T-40_G1.4. As a result, as can be seen in **Figure 5.3** the more remaining carbon inside the T-10_G1.4 produced a higher density of graphene ad-layers patches on it than of T-40_G1.4.

5.3 Challenges for quantitative evaluation of HACD

A quantitative evaluation of the proposed mechanism for HACD based on reliable diffusion coefficient for carbon, hydrogen and other compounds in copper, can lead us to a universal model for nucleation of GFs on copper during the CVD process. Such an evaluation requires accurate values for diffusion coefficients and solubility of carbon in the Cu foil. One, may either consider using the given parameters in the literature or develop an evaluation based on the achieved data from ToF-SIMS measurement. However, each of these approaches suffers from their own obstacle as described in following sections 5.3.1, 5.3.2.

5.3.1 Multifunctional and time-dependent microstructure of Cu foil at elevated temperature.

In the literature, usually, a single crystal copper has been considered for the evaluation of diffusion coefficients or solubility, which excludes the effect of Cu grain boundaries, voids or defects. That may work in case of using a) oxygen free and b) annealed copper foil. But, such an evaluation would be very imprecise for routine CVD experiments, due to the presence of imperfections and oxygen impurities in the untreated foils.

Furthermore, the degree and nature of foil imperfection are changing through the time due to changing microstructure and grain texture of copper foil during heating and annealing. Also, the solubility of carbon in copper changes dramatically as a result of varying oxygen concentration in copper [21]. Therefore, when we apply hydrogen into the system during heating-up and annealing, practically we reduce oxygen from copper and make carbon solubility in copper a time-dependent parameter. Moreover, when the temperature is increased above 800°C, the pre-melted layer forms on the copper foil surface and becomes very vivid at 1000°C, as demonstrated in ref [22]. However, yet this liquid layer was not well characterized in the literature. The presence of the pre-melted layer, which can also be affected by impurities, induces even more complexity for the evaluation.

All of the effects listed above makes diffusion coefficients and carbon solubility very complicated to calculate and varying parameters. A quantitative evaluation or even estimation of such a complex time-dependent structure requires individual studies for each involving effect as well as investigating the interplay between all of the linked parameters. This requires individual and specialized thesis works.

5.3.2 Mixing effect (re-implantation) in ToF-SIMS measurements

Since the one atom thick graphene film is growing on 25 µm copper foil during the CVD process, even a ppm level of intrinsic carbon in copper foil can effect on growth regime. Accordingly, tracing the intrinsic carbon in the copper with adequate accuracy is a challenging experiment. On the one hand, we need a system that can resolve the detected carbon atom from the whole substance with the sensitivity blew 10^4. On the other hand, to exclude surface carbon from the carbon embedded in the bulk, we need a technique that can measure the depth profile of carbon within the copper bulk with the aforementioned mass-sensitivity. Such restrictions limited our options from the available

techniques to ToF-SIMS for measuring carbon content and tracing its variation in the Cu foils after treating in the CVD process.

However, it is well known that surface atoms can be re-implanted inside the bulk of the inspecting sample during sputtering and bombardment. The Re-implantation of carbon can cause a general broadening in ToF-SIMS profiles. [129] Nevertheless, the mixing effect (re-implantation) is always the same under the same analysis conditions. Hence, as the all measurements are acquired under the same conditions, the presented mixing is the same as in all measurements. Therefore all the differences we see between the measurements are real and can be discussed. Also, as we discuss in the next paragraphs with specific examples, we can conclude that in carbon signal from re-implantation of surface carbon does not dominate the measured profiling of carbon in the copper bulk.

a) Crossing of the carbon profiles of P-6 and T-0: In **Figure 3.5**, while the carbon intensity in P-6 is more than one order of magnitude higher than of T-0, at depth above 5 nm (5 nm >), the carbon profile of P-6 crosses the profile of T-0 at 10 nm and goes below that of T-0 at deeper region. If surface carbon was the only source, we would have similar decay rates in the profiles with no such crossings.

b) The crossing of the carbon profile of T-0, T-40, T-80 and T-100: In **Figure 3.9**, a similar discussion given above can be applied for the crossing of the carbon profile of T-0, T-40, T-80 and T-100.

These observations deny dominancy of carbon re-implantation during ToF-SIMS measurements over actual profiles. Therefore, the measured profiles reflect the migration of carbon from bulk toward the surface. However, since their scales are not calibrated, they are not delivering a quantitatively accurate value for an analytical calculation.

6 Conclusion and future work

The following novel experimental results are attained from the studies of this thesis on the interplay between intrinsic carbon of copper and hydrogen concentration during thermal treatment of copper foil in the CVD process for the growth of graphene:

The intrinsic carbon in the copper foil and its depletion during annealing phase assisted by hydrogen (HACD) can be the main determinant factor for the initial nucleation and growth of graphene flakes on the copper before the growth phase. For the first time, we disclose spontaneous nucleation of graphene flake (SNGFs) on a copper foil in the absence of external carbon source but under optimized hydrogen concentration and annealing duration. Therefore, SNGFs during annealing restricts the maximum average crystal-size of graphene film, grown by CVD method. Besides, it has been thought that the surface imperfection in the graphene growth by CVD on copper is the main cause of nucleation, we explicitly demonstrate that the surface imperfection such as SiOx particles, can remain passive for the nucleation in the absence of high carbon concentration. This picture also clarifies other results about how the number of nucleation sites can be reduced by feeding the CVD system with a tuned oxygen flow before or during the growth phase [4, 28].

Additionally, we illustrate the different aspect of HACD on copper foil that appears during the annealing copper foil under an increased concentration of hydrogen which can reduce the surface density of carbon on copper foil. We demonstrated that increasing hydrogen pressure is boosting HACD mechanism which provides a faster supersaturation of whole copper surface and results in a defected disordered graphitic (DG) film on the surface. At elevated H2 pressure, DG film can be such fragile and defected that get etched

before ending the annealing phase, due to the presence of oxidative impurities in the flowing gas.

Furthermore, we used the boosted HACD at maximized H_2 pressure of the system as a pre-treatment approach to effectively reduce the total carbon content of copper foil and minimize SNGFs effect in another step of annealing at 1.4 mbar H2. Also, we observed the same effect of reducing the carbon content of copper by HACD on reducing the density of graphene ad-layers in the growth step of the CVD process.

The following research can be down as based on the outcomes of this thesis results:

a) Same systematic analysis of HACD on an oxygen-free copper to individually investigate the role of intrinsic oxygen on HACD and SNGFs effects.

b) Same systematic research about HACD and SNGFs on the most common copper foils available on the market from a different supplier, to provide a benchmark leading universal consistency in the growth recipe and growth result of graphene by CVD method.

7 Bibliography

[1] X. Li, W. Cai, J. An, S. Kim, J. Nah, D. Yang, R. Piner, A. Velamakanni, I. Jung, E. Tutuc, S.K. Banerjee, L. Colombo, R.S. Ruoff, Large-area synthesis of high-quality and uniform graphene films on copper foils, Science 324(5932) (2009) 1312-1314.

[2] Y. Hao, M.S. Bharathi, L. Wang, Y. Liu, H. Chen, S. Nie, X. Wang, H. Chou, C. Tan, B. Fallahazad, H. Ramanarayan, C.W. Magnuson, E. Tutuc, B.I. Yakobson, K.F. McCarty, Y.-W. Zhang, P. Kim, J. Hone, L. Colombo, R.S. Ruoff, The Role of Surface Oxygen in the Growth of Large Single-Crystal Graphene on Copper, Science 342(6159) (2013) 720-723.

[3] J. Li, X.-Y. Wang, X.-R. Liu, Z. Jin, D. Wang, L.-J. Wan, Facile growth of centimeter-sized single-crystal graphene on copper foil at atmospheric pressure, Journal of Materials Chemistry C 3(15) (2015) 3530-3535.

[4] W. Guo, F. Jing, J. Xiao, C. Zhou, Y. Lin, S. Wang, Oxidative-Etching-Assisted Synthesis of Centimeter-Sized Single-Crystalline Graphene, Adv. Mater. 28(16) (2016) 3152-3158.

[5] T. Wu, X. Zhang, Q. Yuan, J. Xue, G. Lu, Z. Liu, H. Wang, H. Wang, F. Ding, Q. Yu, X. Xie, M. Jiang, Fast growth of inch-sized single-crystalline graphene from a controlled single nucleus on Cu–Ni alloys, Nature Materials 15 (2016) 43.

[6] L. Banszerus, M. Schmitz, S. Engels, M. Goldsche, K. Watanabe, T. Taniguchi, B. Beschoten, C. Stampfer, Ballistic Transport Exceeding 28 mum in CVD Grown Graphene, Nano Lett. 16(2) (2016) 1387-1391.

[7] F. Bonaccorso, Z. Sun, T. Hasan, A.C. Ferrari, Graphene photonics and optoelectronics, Nature Photonics 4 (2010) 611-622.

[8] D. Wei, Y. Liu, Controllable synthesis of graphene and its applications, Adv. Mater. 22(30) (2010) 3225-3241.

[9] N.O. Weiss, H. Zhou, L. Liao, Y. Liu, S. Jiang, Y. Huang, X. Duan, Graphene: an emerging electronic material, Adv. Mater. 24(43) (2012) 5782-57825.

[10] X. Li, W. Cai, L. Colombo, R.S. Ruoff, Evolution of Graphene Growth on Ni and Cu by Carbon Isotope Labeling, Nano Lett. 9(12) (2009) 4268-4272.

[11] S. Bhaviripudi, X. Jia, M.S. Dresselhaus, J. Kong, Role of kinetic factors in chemical vapor deposition synthesis of uniform large area graphene using copper catalyst, Nano Lett. 10(10) (2010) 4128-4133.

[12] K. Yan, H. Peng, Y. Zhou, H. Li, Z. Liu, Formation of bilayer bernal graphene: layer-by-layer epitaxy via chemical vapor deposition, Nano Lett. 11(3) (2011) 1106-1110.

[13] D.H. Jung, C. Kang, B.H. Son, Y.H. Ahn, J.S. Lee, Correlating nucleation density with heating ramp rates in continuous graphene film formation, Carbon 80 (2014) 708-715.

[14] C.-M. Seah, S.-P. Chai, A.R. Mohamed, Mechanisms of graphene growth by chemical vapour deposition on transition metals, Carbon 70 (2014) 1-21.

[15] P. Wu, X. Zhai, Z. Li, J. Yang, Bilayer Graphene Growth via a Penetration Mechanism, The Journal of Physical Chemistry C 118(12) (2014) 6201-6206.

[16] P. Wu, W. Zhang, Z. Li, J. Yang, Mechanisms of Graphene Growth on Metal Surfaces: Theoretical Perspectives, Small 10(11) (2014) 2136-2150.

[17] S. Kasap, H. Khaksaran, S. Celik, H. Ozkaya, C. Yanik, I.I. Kaya, Controlled growth of large area multilayer graphene on copper by chemical vapour deposition, PCCP 17(35) (2015) 23081-23087.

[18] J.M. Wofford, S. Nie, K. Thürmer, K.F. McCarty, O.D. Dubon, Influence of lattice orientation on growth and structure of graphene on Cu(0 0 1), Carbon 90 (2015) 284-290.

[19] P. Braeuninger-Weimer, B. Brennan, A.J. Pollard, S. Hofmann, Understanding and Controlling Cu-Catalyzed Graphene Nucleation: The Role of Impurities, Roughness, and Oxygen Scavenging, Chem. Mater. 28(24) (2016) 8905-8915.

[20] J. Zhang, P. Hu, X. Wang, Z. Wang, Structural evolution and growth mechanism of graphene domains on copper foil by ambient pressure chemical vapor deposition, Chem. Phys. Lett. 536 (2012) 123-128.

[21] Y. Hao, L. Wang, Y. Liu, H. Chen, X. Wang, C. Tan, S. Nie, J.W. Suk, T. Jiang, T. Liang, J. Xiao, W. Ye, C.R. Dean, B.I. Yakobson, K.F. McCarty, P. Kim, J. Hone, L. Colombo, R.S. Ruoff, Oxygen-activated growth and bandgap tunability of large single-crystal bilayer graphene, Nat Nanotechnol 11(5) (2016) 426-431.

[22] Z.J. Wang, G. Weinberg, Q. Zhang, T. Lunkenbein, A. Klein-Hoffmann, M. Kurnatowska, M. Plodinec, Q. Li, L.F. Chi, R. Schloegl, M.G. Willinger, Direct Observation of Graphene Growth and Associated Copper Substrate Dynamics by in Situ Scanning Electron Microscopy, Acs Nano 9(2) (2015) 1506-1519.

[23] H. Kim, C. Mattevi, M.R. Calvo, J.C. Oberg, L. Artiglia, S. Agnoli, C.F. Hirjibehedin, M. Chhowalla, E. Saiz, Activation Energy Paths for Graphene Nucleation and Growth on Cu, Acs Nano 6(4) (2012) 3614-3623.

[24] H. Chen, W. Zhu, Z. Zhang, Contrasting behavior of carbon nucleation in the initial stages of graphene epitaxial growth on stepped metal surfaces, Phys. Rev. Lett. 104(18) (2010) 186101.

[25] H. Shu, X. Chen, X. Tao, F. Ding, Edge Structural Stability and Kinetics of Graphene Chemical Vapor Deposition Growth, Acs Nano 6(4) (2012) 3243-3250.

[26] A. Cabrero-Vilatela, R.S. Weatherup, P. Braeuninger-Weimer, S. Caneva, S. Hofmann, Towards a general growth model for graphene CVD on transition metal catalysts, Nanoscale 8(4) (2016) 2149-2158.

[27] T. Liang, C. Luan, H. Chen, M. Xu, Exploring oxygen in graphene chemical vapor deposition synthesis, Nanoscale 9(11) (2017) 3719-3735.

[28] J. Kraus, M. Böbel, S. Günther, Suppressing graphene nucleation during CVD on polycrystalline Cu by controlling the carbon content of the support foils, Carbon 96 (2016) 153-165.

[29] B. Liu, N. Xuan, K. Ba, X. Miao, M. Ji, Z. Sun, Towards the standardization of graphene growth through carbon depletion, refilling and nucleation, Carbon 119 (2017) 350-354.

[30] B. Wang, Y.H. Zhang, H.R. Zhang, Z.Y. Chen, X.M. Xie, Y.P. Sui, X.L. Li, G.H. Yu, L.Z. Hu, Z. Jin, X.Y. Liu, Wrinkle-dependent hydrogen etching of chemical vapor deposition-grown graphene domains, Carbon 70 (2014) 75-80.

[31] S. Chaitoglou, E. Bertran, Effect of pressure and hydrogen flow in nucleation density and morphology of graphene bidimensional crystals, Materials Research Express 3(7) (2016) 075603.

[32] I. Vlassiouk, M. Regmi, P.F. Fulvio, S. Dai, P. Datskos, G. Eres, S. Smirnov, Role of Hydrogen in Chemical Vapor Deposition Growth of Large Single-Crystal Graphene, Acs Nano 5(7) (2011) 6069-6076.

[33] Y. Zhang, Z. Li, P. Kim, L.Y. Zhang, C.W. Zhou, Anisotropic Hydrogen Etching of Chemical Vapor Deposited Graphene (vol 6, pg 126, 2012), Acs Nano 6(7) (2012) 6526-6526.

[34] Y. Zhang, H. Zhang, F. Li, H. Shu, Z. Chen, Y. Sui, Y. Zhang, X. Ge, G. Yu, Z. Jin, X. Liu, Invisible growth of microstructural defects in graphene chemical vapor deposition on copper foil, Carbon 96 (2016) 237-242.

[35] S. Choubak, M. Biron, P.L. Levesque, R. Martel, P. Desjardins, No Graphene Etching in Purified Hydrogen, J Phys Chem Lett 4(7) (2013) 1100-3.

[36] S. Choubak, P.L. Levesque, E. Gaufres, M. Biron, P. Desjardins, R. Martel, Graphene CVD: Interplay Between Growth and Etching on Morphology and Stacking by Hydrogen and Oxidizing Impurities, The Journal of Physical Chemistry C 118(37) (2014) 21532-21540.

[37] M.H. Khaksaran, I.I. Kaya, Spontaneous Nucleation and Growth of Graphene Flakes on Copper Foil in the Absence of External Carbon Precursor in Chemical Vapor Deposition, Acs Omega 3(10) (2018) 12575-12583.

[38] I.H. Abidi, Y.Y. Liu, J. Pan, A. Tyagi, M.H. Zhuang, Q.C. Zhang, A.A. Cagang, L.T. Weng, P. Sheng, W.A. Goddard, Z.T. Luo, Regulating Top-Surface Multilayer/Single-Crystal Graphene Growth by "Gettering" Carbon Diffusion at Backside of the Copper Foil, Adv. Funct. Mater. 27(23) (2017).

[39] A.H. Castro Neto, F. Guinea, N.M.R. Peres, K.S. Novoselov, A.K. Geim, The electronic properties of graphene, Rev. Mod. Phys. 81(1) (2009) 109-162.

[40] K.I. Bolotin, K.J. Sikes, Z. Jiang, M. Klima, G. Fudenberg, J. Hone, P. Kim, H.L. Stormer, Ultrahigh electron mobility in suspended graphene, Solid State Commun. 146(9-10) (2008) 351-355.

[41] Y.B. Zhang, T.T. Tang, C. Girit, Z. Hao, M.C. Martin, A. Zettl, M.F. Crommie, Y.R. Shen, F. Wang, Direct observation of a widely tunable bandgap in bilayer graphene, Nature 459(7248) (2009) 820-823.

[42] L.G. De Arco, Y. Zhang, C.W. Schlenker, K. Ryu, M.E. Thompson, C.W. Zhou, Continuous, Highly Flexible, and Transparent Graphene Films by Chemical Vapor Deposition for Organic Photovoltaics, Acs Nano 4(5) (2010) 2865-2873.

[43] X.C. Miao, S. Tongay, M.K. Petterson, K. Berke, A.G. Rinzler, B.R. Appleton, A.F. Hebard, High Efficiency Graphene Solar Cells by Chemical Doping, Nano Lett. 12(6) (2012) 2745-2750.

[44] B.J. Kim, H. Jang, S.K. Lee, B.H. Hong, J.H. Ahn, J.H. Cho, High-Performance Flexible Graphene Field Effect Transistors with Ion Gel Gate Dielectrics, Nano Lett. 10(9) (2010) 3464-3466.

[45] Y. Wang, Z.Q. Shi, Y. Huang, Y.F. Ma, C.Y. Wang, M.M. Chen, Y.S. Chen, Supercapacitor Devices Based on Graphene Materials, J Phys Chem C 113(30) (2009) 13103-13107.

[46] S.M. Paek, E. Yoo, I. Honma, Enhanced Cyclic Performance and Lithium Storage Capacity of SnO2/Graphene Nanoporous Electrodes with Three-Dimensionally Delaminated Flexible Structure, Nano Lett. 9(1) (2009) 72-75.

[47] G.X. Ni, Y. Zheng, S. Bae, C.Y. Tan, O. Kahya, J. Wu, B.H. Hong, K. Yao, B. Ozyilmaz, Graphene-Ferroelectric Hybrid Structure for Flexible Transparent Electrodes, Acs Nano 6(5) (2012) 3935-3942.

[48] P. Blake, P.D. Brimicombe, R.R. Nair, T.J. Booth, D. Jiang, F. Schedin, L.A. Ponomarenko, S.V. Morozov, H.F. Gleeson, E.W. Hill, A.K. Geim, K.S. Novoselov, Graphene-based liquid crystal device, Nano Lett. 8(6) (2008) 1704-1708.

[49] J.D. Fowler, M.J. Allen, V.C. Tung, Y. Yang, R.B. Kaner, B.H. Weiller, Practical Chemical Sensors from Chemically Derived Graphene, Acs Nano 3(2) (2009) 301-306.

[50] K.S. Novoselov, D. Jiang, F. Schedin, T.J. Booth, V.V. Khotkevich, S.V. Morozov, A.K. Geim, Two-dimensional atomic crystals, Proc. Natl. Acad. Sci. U.S.A. 102(30) (2005) 10451-10453.

[51] S. Stankovich, D.A. Dikin, R.D. Piner, K.A. Kohlhaas, A. Kleinhammes, Y. Jia, Y. Wu, S.T. Nguyen, R.S. Ruoff, Synthesis of graphene-based nanosheets via chemical reduction of exfoliated graphite oxide, Carbon 45(7) (2007) 1558-1565.

[52] C. Berger, Z.M. Song, T.B. Li, X.B. Li, A.Y. Ogbazghi, R. Feng, Z.T. Dai, A.N. Marchenkov, E.H. Conrad, P.N. First, W.A. de Heer, Ultrathin epitaxial graphite: 2D electron gas properties and a route toward graphene-based nanoelectronics, J. Phys. Chem. B 108(52) (2004) 19912-19916.

[53] S. Bae, H. Kim, Y. Lee, X.F. Xu, J.S. Park, Y. Zheng, J. Balakrishnan, T. Lei, H.R. Kim, Y.I. Song, Y.J. Kim, K.S. Kim, B. Ozyilmaz, J.H. Ahn, B.H. Hong, S. Iijima, Roll-to-roll production of 30-inch graphene films for transparent electrodes, Nat Nanotechnol 5(8) (2010) 574-578.

[54] K.S. Kim, Y. Zhao, H. Jang, S.Y. Lee, J.M. Kim, K.S. Kim, J.H. Ahn, P. Kim, J.Y. Choi, B.H. Hong, Large-scale pattern growth of graphene films for stretchable transparent electrodes, Nature 457(7230) (2009) 706-710.

[55] A. Reina, S. Thiele, X.T. Jia, S. Bhaviripudi, M.S. Dresselhaus, J.A. Schaefer, J. Kong, Growth of Large-Area Single- and Bi-Layer Graphene by Controlled Carbon Precipitation on Polycrystalline Ni Surfaces, Nano Res 2(6) (2009) 509-516.

[56] B.J. Kang, J.H. Mun, C.Y. Hwang, B.J. Cho, Monolayer graphene growth on sputtered thin film platinum, J. Appl. Phys. 106(10) (2009).

[57] L.B. Gao, W.C. Ren, J.P. Zhao, L.P. Ma, Z.P. Chen, H.M. Cheng, Efficient growth of high-quality graphene films on Cu foils by ambient pressure chemical vapor deposition, Appl. Phys. Lett. 97(18) (2010).

[58] R. John, A. Ashokreddy, C. Vijayan, T. Pradeep, Single- and few-layer graphene growth on stainless steel substrates by direct thermal chemical vapor deposition, Nanotechnology 22(16) (2011).

[59] B. Wang, Y.H. Zhang, Z.Y. Chen, Y.W. Wu, Z. Jin, X.Y. Liu, L.Z. Hu, G.H. Yu, High quality graphene grown on single-crystal Mo(110) thin films, Mater. Lett. 93 (2013) 165-168.

[60] S.M. Kim, A. Hsu, Y.-H. Lee, M. Dresselhaus, T. Palacios, K.K. Kim, J. Kong, The effect of copper pre-cleaning on graphene synthesis, Nanotechnology 24(36) (2013) 365602.

[61] G.H. Han, F. Gunes, J.J. Bae, E.S. Kim, S.J. Chae, H.J. Shin, J.Y. Choi, D. Pribat, Y.H. Lee, Influence of Copper Morphology in Forming Nucleation Seeds for Graphene Growth, Nano Lett. 11(10) (2011) 4144-4148.

[62] A. Reina, X. Jia, J. Ho, D. Nezich, H. Son, V. Bulovic, M.S. Dresselhaus, J. Kong, Large Area, Few-Layer Graphene Films on Arbitrary Substrates by Chemical Vapor Deposition, Nano Lett. 9(1) (2009) 30-35.

[63] Y. Zhang, L.Y. Zhang, C.W. Zhou, Review of Chemical Vapor Deposition of Graphene and Related Applications, Acc. Chem. Res. 46(10) (2013) 2329-2339.

[64] M. Singh, H.S. Jha, P. Agarwal, Growth of large sp(2) domain size single and multi-layer graphene films at low substrate temperature using hot filament chemical vapor deposition, Mater. Lett. 126 (2014) 249-252.

[65] Y.H. Zhang, Z.Y. Chen, B. Wang, Y.W. Wu, Z. Jin, X.Y. Liu, G.H. Yu, Controllable growth of millimeter-size graphene domains on Cu foil, Mater. Lett. 96 (2013) 149-151.

[66] N. Kishi, A. Fukaya, R. Sugita, T. Kado, T. Soga, T. Jimbo, Synthesis of graphenes on Ni foils by chemical vapor deposition of alcohol with IR-lamp heating, Mater. Lett. 79 (2012) 21-24.

[67] C. Mattevi, H. Kim, M. Chhowalla, A review of chemical vapour deposition of graphene on copper, J. Mater. Chem. 21(10) (2011) 3324-3334.

[68] J.D. Wood, S.W. Schmucker, A.S. Lyons, E. Pop, J.W. Lyding, Effects of Polycrystalline Cu Substrate on Graphene Growth by Chemical Vapor Deposition, Nano Lett. 11(11) (2011) 4547-4554.

[69] F. Qing, R. Jia, B.W. Li, C. Liu, C.Z. Li, B. Peng, L. Deng, W. Zhang, Y. Li, R.S. Ruoff, X. Li, Graphene growth with 'no' feedstock, 2d Mater 4(2) (2017) 025089.

[70] C. Jia, J. Jiang, L. Gan, X. Guo, Direct optical characterization of graphene growth and domains on growth substrates, Sci. Rep. 2 (2012) 707.

[71] X. Li, C.W. Magnuson, A. Venugopal, J. An, J.W. Suk, B. Han, M. Borysiak, W. Cai, A. Velamakanni, Y. Zhu, L. Fu, E.M. Vogel, E. Voelkl, L. Colombo, R.S. Ruoff,

Graphene Films with Large Domain Size by a Two-Step Chemical Vapor Deposition Process, Nano Lett. 10(11) (2010) 4328-4334.

[72] A.W. Robertson, J.H. Warner, Hexagonal single crystal domains of few-layer graphene on copper foils, Nano Lett. 11(3) (2011) 1182-9.

[73] Q. Li, H. Chou, J.H. Zhong, J.Y. Liu, A. Dolocan, J. Zhang, Y. Zhou, R.S. Ruoff, S. Chen, W. Cai, Growth of adlayer graphene on Cu studied by carbon isotope labeling, Nano Lett. 13(2) (2013) 486-90.

[74] Z. Yan, Y.Y. Liu, L. Ju, Z.W. Peng, J. Lin, G. Wang, H.Q. Zhou, C.S. Xiang, E.L.G. Samuel, C. Kittrell, V.I. Artyukhov, F. Wang, B.I. Yakobson, J.M. Tour, Large Hexagonal Bi- and Trilayer Graphene Single Crystals with Varied Interlayer Rotations, Angew Chem Int Edit 53(6) (2014) 1565-1569.

[75] O. Frank, J. Vejpravova, V. Holy, L. Kavan, M. Kalbac, Interaction between graphene and copper substrate: The role of lattice orientation, Carbon 68 (2014) 440-451.

[76] I. Vlassiouk, P. Fulvio, H. Meyer, N. Lavrik, S. Dai, P. Datskos, S. Smirnov, Large scale atmospheric pressure chemical vapor deposition of graphene, Carbon 54 (2013) 58-67.

[77] M. Regmi, M.F. Chisholm, G. Eres, The effect of growth parameters on the intrinsic properties of large-area single layer graphene grown by chemical vapor deposition on Cu, Carbon 50(1) (2012) 134-141.

[78] S. Bae, S.J. Kim, D. Shin, J.H. Ahn, B.H. Hong, Towards industrial applications of graphene electrodes, Phys. Scr. T146 (2012).

[79] S.P. Pang, Y. Hernandez, X.L. Feng, K. Mullen, Graphene as Transparent Electrode Material for Organic Electronics, Adv. Mater. 23(25) (2011) 2779-2795.

[80] T. Sun, Z.L. Wang, Z.J. Shi, G.Z. Ran, W.J. Xu, Z.Y. Wang, Y.Z. Li, L. Dai, G.G. Qin, Multilayered graphene used as anode of organic light emitting devices, Appl. Phys. Lett. 96(13) (2010).

[81] J.B. Wu, M. Agrawal, H.A. Becerril, Z.N. Bao, Z.F. Liu, Y.S. Chen, P. Peumans, Organic Light-Emitting Diodes on Solution-Processed Graphene Transparent Electrodes, Acs Nano 4(1) (2010) 43-48.

[82] L. Huang, Q.H. Chang, G.L. Guo, Y. Liu, Y.Q. Xie, T. Wang, B. Ling, H.F. Yang, Synthesis of high-quality graphene films on nickel foils by rapid thermal chemical vapor deposition, Carbon 50(2) (2012) 551-556.

[83] H.J. Park, J. Meyer, S. Roth, V. Skakalova, Growth and properties of few-layer graphene prepared by chemical vapor deposition, Carbon 48(4) (2010) 1088-1094.

[84] S.S. Chen, W.W. Cai, R.D. Piner, J.W. Suk, Y.P. Wu, Y.J. Ren, J.Y. Kang, R.S. Ruoff, Synthesis and Characterization of Large-Area Graphene and Graphite Films on Commercial Cu-Ni Alloy Foils, Nano Lett. 11(9) (2011) 3519-3525.

[85] A. Delamoreanu, C. Rabot, C. Vallee, A. Zenasni, Wafer scale catalytic growth of graphene on nickel by solid carbon source, Carbon 66 (2014) 48-56.

[86] V.T. Nguyen, H.D. Le, V.C. Nguyen, T.T.T. Ngo, D.Q. Le, X.N. Nguyen, N.M. Phan, Synthesis of multi-layer graphene films on copper tape by atmospheric pressure chemical vapor deposition method, Adv Nat Sci-Nanosci 4(3) (2013).

[87] M.P. Lavin-Lopez, J.L. Valverde, M.C. Cuevas, A. Garrido, L. Sanchez-Silva, P. Martinez, A. Romero-Izquierdo, Synthesis and characterization of graphene: influence of synthesis variables, PCCP 16(7) (2014) 2962-2970.

[88] X.S. Li, Y.W. Zhu, W.W. Cai, M. Borysiak, B.Y. Han, D. Chen, R.D. Piner, L. Colombo, R.S. Ruoff, Transfer of Large-Area Graphene Films for High-Performance Transparent Conductive Electrodes, Nano Lett. 9(12) (2009) 4359-4363.

[89] S. Roddaro, P. Pingue, V. Piazza, V. Pellegrini, F. Beltram, The optical visibility of graphene: Interference colors of ultrathin graphite on SiO2, Nano Lett. 7(9) (2007) 2707-2710.

[90] P. Blake, E.W. Hill, A.H. Castro Neto, K.S. Novoselov, D. Jiang, R. Yang, T.J. Booth, A.K. Geim, Making graphene visible, Appl. Phys. Lett. 91(6) (2007).

[91] J. Henrie, S. Kellis, S.M. Schultz, A. Hawkins, Electronic color charts for dielectric films on silicon, Opt. Express 12(7) (2004) 1464-1469.

[92] Z.H. Ni, H.M. Wang, J. Kasim, H.M. Fan, T. Yu, Y.H. Wu, Y.P. Feng, Z.X. Shen, Graphene thickness determination using reflection and contrast spectroscopy, Nano Lett. 7(9) (2007) 2758-2763.

[93] V. Yu, M. Hilke, Large contrast enhancement of graphene monolayers by angle detection, Appl. Phys. Lett. 95(15) (2009).

[94] D.L. Duong, G.H. Han, S.M. Lee, F. Gunes, E.S. Kim, S.T. Kim, H. Kim, Q.H. Ta, K.P. So, S.J. Yoon, S.J. Chae, Y.W. Jo, M.H. Park, S.H. Chae, S.C. Lim, J.Y. Choi, Y.H. Lee, Probing graphene grain boundaries with optical microscopy, Nature 490(7419) (2012) 235-9.

[95] N. Reckinger, A. Felten, C.N. Santos, B. Hackens, J.F. Colomer, The influence of residual oxidizing impurities on the synthesis of graphene by atmospheric pressure chemical vapor deposition, Carbon 63 (2013) 84-91.

[96] H.R. Zhang, Y.H. Zhang, B. Wang, Z.Y. Chen, Y.Q. Zhang, Y.P. Sui, G.H. Yu, Z. Jin, X.Y. Liu, Stripe distributions of graphene-coated Cu foils and their effects on the reduction of graphene wrinkles, Rsc Adv 5(117) (2015) 96587-96592.

[97] Y. Cheng, Y.N. Song, D.C. Zhao, X.W. Zhang, S.Q. Yin, P. Wang, M. Wang, Y. Xia, S. Maruyama, P. Zhao, H.T. Wang, Direct Identification of Multilayer Graphene Stacks on Copper by Optical Microscopy, Chem. Mater. 28(7) (2016) 2165-2171.

[98] J.H. Warner, F. Schaffel, A. Bachmatiuk, M.H. Rummeli, Graphene: Fundamentals and Emergent Applications, Graphene: Fundamentals and Emergent Applications (2013) 1-450.

[99] V. Kochat, A.N. Pal, E.S. Sneha, A. Sampathkumar, A. Gairola, S.A. Shivashankar, S. Raghavan, A. Ghosh, High contrast imaging and thickness determination of graphene with in-column secondary electron microscopy, J. Appl. Phys. 110(1) (2011).

[100] M.H. Park, T.H. Kim, C.W. Yang, Thickness contrast of few-layered graphene in SEM, Surf. Interface Anal. 44(11-12) (2012) 1538-1541.

[101] J. Lee, X.Q. Zheng, R.C. Roberts, P.X.L. Feng, Scanning electron microscopy characterization of structural features in suspended and non-suspended graphene by customized CVD growth, Diamond Relat. Mater. 54 (2015) 64-73.

[102] H.F. Wang, C. Yamada, Y. Homma, Scanning electron microscopy imaging mechanisms of CVD-grown graphene on Cu substrate revealed by in situ observation, Jpn. J. Appl. Phys. 54(5) (2015).

[103] Z.J. Wang, J.C. Dong, Y. Cui, G. Eres, O. Timpe, Q. Fu, F. Ding, R. Schloegl, M.G. Willinger, Stacking sequence and interlayer coupling in few-layer graphene revealed by in situ imaging, Nat Commun 7 (2016).

[104] R.S. Weatherup, A.J. Shahan, Z.J. Wang, K. Mingard, A.J. Pollard, M.G. Willinger, R. Schloegl, P.W. Voorhees, S. Hofmann, In Situ Graphene Growth Dynamics on Polycrystalline Catalyst Foils, Nano Lett. 16(10) (2016) 6196-6206.

[105] L.L. Fan, Z. Li, X. Li, K.L. Wang, M.L. Zhong, J.Q. Wei, D.H. Wu, H.W. Zhu, Controllable growth of shaped graphene domains by atmospheric pressure chemical vapour deposition, Nanoscale 3(12) (2011) 4946-4950.

[106] L.B. Gao, W.C. Ren, H.L. Xu, L. Jin, Z.X. Wang, T. Ma, L.P. Ma, Z.Y. Zhang, Q. Fu, L.M. Peng, X.H. Bao, H.M. Cheng, Repeated growth and bubbling transfer of graphene with millimetre-size single-crystal grains using platinum, Nat Commun 3 (2012).

[107] P.W. Sutter, J.I. Flege, E.A. Sutter, Epitaxial graphene on ruthenium, Nature Materials 7(5) (2008) 406-411.

[108] Y.A. Wu, A.W. Robertson, F. Schaffel, S.C. Speller, J.H. Warner, Aligned Rectangular Few-Layer Graphene Domains on Copper Surfaces, Chem. Mater. 23(20) (2011) 4543-4547.

[109] H. Hiura, H. Miyazaki, K. Tsukagoshi, Determination of the Number of Graphene Layers: Discrete Distribution of the Secondary Electron Intensity Stemming from Individual Graphene Layers, Appl Phys Express 3(9) (2010).

[110] J.R. Ferraro, K. Nakamoto, C.W. Brown, Introductory Raman spectroscopy, 2nd ed., Academic Press, Amsterdam ; Boston, 2003.

[111] L.G. Cancado, M.A. Pimenta, B.R.A. Neves, M.S.S. Dantas, A. Jorio, Influence of the atomic structure on the Raman spectra of graphite edges, Phys. Rev. Lett. 93(24) (2004).

[112] L.G. Cancado, M.A. Pimenta, B.R.A. Neves, G. Medeiros-Ribeiro, T. Enoki, Y. Kobayashi, K. Takai, K. Fukui, M.S. Dresselhaus, R. Saito, A. Jorio, Anisotropy of the Raman spectra of nanographite ribbons, Phys. Rev. Lett. 93(4) (2004).

[113] M.S. Dresselhaus, G. Dresselhaus, R. Saito, A. Jorio, Raman spectroscopy of carbon nanotubes, Phys Rep 409(2) (2005) 47-99.

[114] A.C. Ferrari, J. Robertson, Interpretation of Raman spectra of disordered and amorphous carbon, Physical Review B 61(20) (2000) 14095-14107.

[115] M.A. Pimenta, G. Dresselhaus, M.S. Dresselhaus, L.G. Cancado, A. Jorio, R. Saito, Studying disorder in graphite-based systems by Raman spectroscopy, PCCP 9(11) (2007) 1276-1291.

[116] L.G. Cancado, A. Reina, J. Kong, M.S. Dresselhaus, Geometrical approach for the study of G ' band in the Raman spectrum of monolayer graphene, bilayer graphene, and bulk graphite, Physical Review B 77(24) (2008).

[117] A.C. Ferrari, J.C. Meyer, V. Scardaci, C. Casiraghi, M. Lazzeri, F. Mauri, S. Piscanec, D. Jiang, K.S. Novoselov, S. Roth, A.K. Geim, Raman spectrum of graphene and graphene layers, Phys. Rev. Lett. 97(18) (2006).

[118] A.C. Ferrari, Raman spectroscopy of graphene and graphite: Disorder, electron-phonon coupling, doping and nonadiabatic effects, Solid State Commun. 143(1-2) (2007) 47-57.

[119] C. Casiraghi, S. Pisana, K.S. Novoselov, A.K. Geim, A.C. Ferrari, Raman fingerprint of charged impurities in graphene, Appl. Phys. Lett. 91(23) (2007).

[120] A. Gupta, G. Chen, P. Joshi, S. Tadigadapa, P.C. Eklund, Raman scattering from high-frequency phonons in supported n-graphene layer films, Nano Lett. 6(12) (2006) 2667-2673.

[121] D. Graf, F. Molitor, K. Ensslin, C. Stampfer, A. Jungen, C. Hierold, L. Wirtz, Spatially resolved raman spectroscopy of single- and few-layer graphene, Nano Lett. 7(2) (2007) 238-242.

[122] A.C. Ferrari, J. Robertson, Raman spectroscopy of amorphous, nanostructured, diamond-like carbon, and nanodiamond, Philos T R Soc A 362(1824) (2004) 2477-2512.

[123] L.M. Malard, M.A. Pimenta, G. Dresselhaus, M.S. Dresselhaus, Raman spectroscopy in graphene, Phys Rep 473(5-6) (2009) 51-87.

[124] C. Castiglioni, F. Negri, M. Rigolio, G. Zerbi, Raman activation in disordered graphites of the A(1)(') symmetry forbidden k not equal 0 phonon: The origin of the D line, J. Chem. Phys. 115(8) (2001) 3769-3778.

[125] D.R. Cooper, B. D'Anjou, N. Ghattamaneni, B. Harack, M. Hilke, A. Horth, N. Majlis, M. Massicotte, L. Vandsburger, E. Whiteway, V. Yu, Experimental Review of Graphene, ISRN Condensed Matter Physics 2012 (2012) 56.

[126] D. Yoon, H. Moon, Y.W. Son, G. Samsonidze, B.H. Park, J.B. Kim, Y. Lee, H. Cheong, Strong Polarization Dependence of Double-Resonant Raman Intensities in Graphene, Nano Lett. 8(12) (2008) 4270-4274.

[127] L.G. Cancado, K. Takai, T. Enoki, M. Endo, Y.A. Kim, H. Mizusaki, N.L. Speziali, A. Jorio, M.A. Pimenta, Measuring the degree of stacking order in graphite by Raman spectroscopy, Carbon 46(2) (2008) 272-275.

[128] L.G. Cancado, M.A. Pimenta, R. Saito, A. Jorio, L.O. Ladeira, A. Grueneis, A.G. Souza, G. Dresselhaus, M.S. Dresselhaus, Stokes and anti-Stokes double resonance Raman scattering in two-dimensional graphite, Physical Review B 66(3) (2002).

[129] S. Fearn, An Introduction to Time-of-Flight Secondary Ion Mass Spectrometry (ToF-SIMS) and its Application to Materials Science, Morgan & Claypool Publishers, 2015.

[130] S. Fearn, Characterisation of biological material with ToF-SIMS: a review, Mater. Sci. Technol. 31(2) (2015) 148-161.

[131] D. Touboul, F. Halgand, A. Brunelle, R. Kersting, E. Tallarek, B. Hagenhoff, O. Laprevote, Tissue molecular ion imaging by gold cluster ion bombardment, Anal. Chem. 76(6) (2004) 1550-1559.

[132] F. Kollmer, Cluster primary ion bombardment of organic materials, Appl. Surf. Sci. 231 (2004) 153-158.

[133] A. Brunelle, D. Touboul, O. Laprevote, Biological tissue imaging with time-of-flight secondary ion mass spectrometry and cluster ion sources, J. Mass Spectrom. 40(8) (2005) 985-999.

[134] P. Aydogan, E.O. Polat, C. Kocabas, S. Suzer, X-ray photoelectron spectroscopy for identification of morphological defects and disorders in graphene devices, Journal of Vacuum Science & Technology A 34(4) (2016).

[135] A. Ibrahim, S. Akhtar, M. Atieh, R. Karnik, T. Laoui, Effects of annealing on copper substrate surface morphology and graphene growth by chemical vapor deposition, Carbon 94 (2015) 369-377.

[136] S. Saji, T. Kadokura, H. Anada, K. Notoya, N. Takano, Solid solubility of carbon in copper during mechanical alloying, Mater T Jim 39(7) (1998) 778-781.

[137] W.T.S. Ramos, T.H.R. Cunha, I.D. Barcelos, D.R. Miquita, G.A. Ferrari, S. de Oliveira, L.M. Seara, E.G.S. Neto, A.S. Ferlauto, R.G. Lacerda, The role of hydrogen partial pressure on the annealing of copper substrates for graphene CVD synthesis, Materials Research Express 3(4) (2016) 045602.

[138] G.A. Lopez, E. Mittemeijer, The solubility of C in solid Cu, Scripta Mater. 51(1) (2004) 1-5.

[139] B. Hu, Y. Jin, D. Guan, Z. Luo, B. Shang, Q. Fang, H. Ruan, H2-Dependent Carbon Dissolution and Diffusion-Out in Graphene Chemical Vapor Deposition Growth, The Journal of Physical Chemistry C 119(42) (2015) 24124-24131.

[140] H. Zhang, Y. Zhang, Y. Zhang, Z. Chen, Y. Sui, X. Ge, G. Yu, Z. Jin, X. Liu, Edge morphology evolution of graphene domains during chemical vapor deposition cooling revealed through hydrogen etching, Nanoscale 8(7) (2016) 4145-4150.

[141] I. Ruiz, W. Wang, A. George, C.S. Ozkan, M. Ozkan, Silicon Oxide Contamination of Graphene Sheets Synthesized on Copper Substrates via Chemical Vapor Deposition, Advanced Science, Engineering and Medicine 6(10) (2014) 1070-1075.

[142] N. Lisi, T. Dikonimos, F. Buonocore, M. Pittori, R. Mazzaro, R. Rizzoli, S. Marras, A. Capasso, Contamination-free graphene by chemical vapor deposition in quartz furnaces, Sci Rep-Uk 7(1) (2017) 9927.

[143] X. Li, C.W. Magnuson, A. Venugopal, R.M. Tromp, J.B. Hannon, E.M. Vogel, L. Colombo, R.S. Ruoff, Large-area graphene single crystals grown by low-pressure chemical vapor deposition of methane on copper, J. Am. Chem. Soc. 133(9) (2011) 2816-9.

[144] S. Chen, H. Ji, H. Chou, Q. Li, H. Li, J.W. Suk, R. Piner, L. Liao, W. Cai, R.S. Ruoff, Millimeter-size single-crystal graphene by suppressing evaporative loss of Cu during low pressure chemical vapor deposition, Adv. Mater. 25(14) (2013) 2062-5.

[145] V. Miseikis, D. Convertino, N. Mishra, M. Gemmi, T. Mashoff, S. Heun, N. Haghighian, F. Bisio, M. Canepa, V. Piazza, C. Coletti, Rapid CVD growth of millimetre-sized single crystal graphene using a cold-wall reactor, 2d Mater 2(1) (2015) 014006.

[146] B.R. Luo, E.L. Gao, D.C. Geng, H.P. Wang, Z.P. Xu, G. Yu, Etching-Controlled Growth of Graphene by Chemical Vapor Deposition, Chem. Mater. 29(3) (2017) 1022-1027.

[147] H. Wang, G. Wang, P. Bao, S. Yang, W. Zhu, X. Xie, W.J. Zhang, Controllable synthesis of submillimeter single-crystal monolayer graphene domains on copper foils by suppressing nucleation, J. Am. Chem. Soc. 134(8) (2012) 3627-30.

[148] Z. Yan, J. Lin, Z. Peng, Z. Sun, Y. Zhu, L. Li, C. Xiang, E.L. Samuel, C. Kittrell, J.M. Tour, Toward the Synthesis of Wafer-Scale Single-Crystal Graphene on Copper Foils, Acs Nano 6(10) (2012) 9110-9117.